ON-THE-FLY GENERATION OF SPATIAL TRANSFER FUNCTIONS FOR EFFICIENT MONTE CARLO-TH COUPLED CALCULATIONS

A Dissertation
Presented to
The Academic Faculty

By

Stefano Terlizzi

In Partial Fulfillment
of the Requirements for the Degree
Doctor of Philosophy in Nuclear Engineering

Georgia Institute of Technology

December 2020

ON-THE-FLY GENERATION OF SPATIAL TRANSFER FUNCTIONS FOR EFFICIENT MONTE CARLO-TH COUPLED CALCULATIONS

Approved by:

Dr. Dan Kotlyar, Advisor
Nuclear & Radiological Engineering
Georgia Institute of Technology

Dr. Bojan Petrovic
Nuclear & Radiological Engineering
Georgia Institute of Technology

Dr. Weston M. Stacey
Nuclear & Radiological Engineering
Georgia Institute of Technology

Dr. Pavel V. Tsvetkov
Department of Nuclear Engineering
Texas A&M University

Dr. Joel A. Kulesza
Los Alamos National Laboratory

Date Approved: November 30, 2020

To Jessica and Leo

ACKNOWLEDGEMENTS

During my years at Georgia Tech, I have been blessed with the opportunity to gain an incredible amount of knowledge and connections that will be greatly valuable for the rest of my life and career.

First, I would like to thank my advisor, Dr. Dan Kotlyar, for his support, guidance, and encouragement during my doctoral studies. I would like to further extend my gratitude to the reading committee members, Dr. Bojan Petrovic, Dr. Pavel Tsvetkov, Dr. Weston Stacey, and Dr. Joel Kulesza, for their feedback and constructive criticisms that made this thesis more solid and consistent. I would also like to thank my mentors at Los Alamos National Laboratory, Dr Topher Matthews and Mike Cooper, for allowing me to enlarge my research horizon outside my comfort zone.

Second, I would like to thank my colleagues at the CORE laboratory, Drew Johnson, Coral Kazaroff, Vedant Mehta, Matthew Krecicki, Jim Wang, Gus, Naiki Kaffezakis, and, previously, at the CRMP laboratory, Gabe (Andrew) Kooreman, Kyle Remley, Ryan Hon, Daniel Lago, Chris Chapman, and Alex Huning. I thank them for the stimulating discussions on reactor physics and the nerdy jokes that made this PhD more enjoyable.

Third, I would like to thank some of the incredible people I met outside the laboratories. I would like to thank the lunchtime group: Abdalla, Pietro, Joaquin, Giovanni, Matias, Sourabh, Giorgio, Sam, Banza and Pietro P. The soccer group: Esteban, Camilo, Lucas, Principio, Roberto, and Sush, and the many others I cannot list in this acknowledgement section.

Fourth, my family has been a constant support in reaching this objective. I would like to thank my parents, Leonardo and Vincenza, and my sisters, Chiara and Fabiana, for cheering for me from afar. Finally, I would like to thank my amazing wife Jessica and my son Leo, to which this thesis is dedicated, and who were always on my side in this crazy year.

TABLE OF CONTENTS

LIST OF TABLES

LIST OF FIGURES

SUMMARY

A novel methodology to efficiently perform coupled Monte Carlo (MC)- Thermal Hydraulics (TH) is developed in this thesis. This goal is achieved by accelerating the classical Picard iteration scheme using a deterministic, perturbation-based prediction step. The latter produces an improved initial guess of the power and the corresponding TH fields, *i.e.*, temperature and density, at the next Monte Carlo calculation, therefore accelerating the convergence of the whole algorithm. The prediction relies on a novel technique for the calculation of the cross-sections spatial distribution due to variations in the TH scalar fields. The latter technique is an original and novel contribution that relies on the definition of generalized transfer functions (GTF) to calculate the cross-sections given a change in density and temperature profiles. The method has many desirable characteristics. First, it allows to capture non-local effects contrarily to current methods for cross-sections interpolation/reconstruction. Second, the GTF, despite being here applied to MC codes, is general and may be used for deterministic methods as well, *e.g.*, GRIFFIN. Finally, the method is geometrically agnostic. Thus, it can be utilized to study non-traditional geometries, *i.e.*, not square or hexagonal, that characterize many advanced nuclear reactors' concepts. When applied to the acceleration of the MC-TH Picard iteration, it was observed a net acceleration with respect to the standard calculation procedure. These results were confirmed for both mono-dimensional and three-dimensional test problems based on light-water reactors designs. More specifically, the following novel contributions are present in this work:

- A novel methodology for on-the-fly calculation of macroscopic cross-sections due to spatial TH variations, called generalized transfer function (GTF), was formulated. This technique allows to capture non-local effects that are not included in standard cross-sections' generation techniques.

- The GTF was leveraged to define an acceleration scheme for coupled MC-TH calculations in conjunction with a perturbation-based power prediction model based on

the use of the fission matrix modes.

- The methodology was tested against an extruded boiling water reactor unit-cell problem for the sake of proving the methodology's concept with minimum computational effort on a non-trivial problem. It was observed a speed up between 2.1 and 12.4 depending on the number of criticality cycles per Picard iteration with negligible losses in accuracy.

- The methodology was tested against a 3D PWR-based mini-core with full TH feedback. The benchmark was evaluated at two different inlet water temperature to analyze the ability of the method to predict the power variation for both single-phase and two-phase flow. For 3D cases, it was found a speedup between 2.2 and 5.5 depending on the number of criticality cycles, with negligible loss of accuracy.

CHAPTER 1
INTRODUCTION

1.1 Background

The accurate prediction of the power spatial distribution is crucial for the design of nuclear reactors. This is because the power distribution is directly linked to (1) the maximum reactor core temperature and associated design margins through the Thermal Hydraulic (TH) equations that account for heat transfer and fluid mechanics, (2) the isotopic distribution and fuel depletion that is linked to the reactor's economics, and the (3) equilibrium Xenon concentration that determines the Beginning-of-Life (BOL) excess reactivity and, thus, deeply influences the final design of the reactor. The accurate computation of the power distribution is therefore of paramount importance to ensure the safety of the reactor, determine its design, and economic competitiveness.

Monte Carlo (MC) methods for particles trasport can be utilized to accurately simulate neutron and photon transport, and, therefore, the power deposition in nuclear reactors. This is because MC methods are geometrically flexible, *i.e.*, modelers are not bound to use square or hexagonal lattices, and utilize continuous energy and angle for the cross-sections' and neutron flux description [1]. These characteristics render MC methods appealing for advanced reactors designs that either rely on non-traditional fuel-geometries, *e.g.*, LightBridge™ fuel [2], or are characterized by neutron flux spectra substantially different from characteristic spectra found in traditional Light Water Reactors (LWR), *e.g.*, epithermal space reactors [3]. Despite allowing close-to-exact treatment of the energy and spatial dependence of the neutron density field, MC methods are stochastic in nature. Thus, the MC results/tallies have a confidence interval and associated standard deviation. In order to keep the latter within acceptable limits, *e.g.*, conventionally 1% for the power and

flux tallies, and avoid correlations among the tallies due to under-sampling, many particles need to be sampled. For full LWR core calculations, billions of neutrons may be necessary at each criticality iteration to avoid under-sampling and high uncertainty. For instance, Herman estimates that four billion particles are needed to avoid under-sampling in 3D full core criticality calculations of the BEAVRS reactor. This translates into 50,000 core-hours for a single Monte Carlo calculation performed ”in absence of massive tallies” [4]. When multiphysics calculations are performed, such as MC-TH coupled calculations, the MC calculations are repeated several times, therefore emphasizing the issue related to their computational expense. Thus, minimizing the number of MC calculation is crucial to limit the computational cost associated to multiphysics calculations relying on a MC solver for modeling the neutron transport in the reactor core.

1.2 Definitions

In the remainder of this thesis, the acronyms “MC” and “TH”, that were introduced in Section 1.1, are utilized in a narrow sense.

The acronym “MC” is used to denote a stochastic technique for the numerical solution of the criticality problem introduced in Section 2.1.1, *i.e.*, solution of the linear transport equation in criticality form subject to vacuum or reflective boundary conditions, Eqs. 2.1-2.3. Solving the criticality problem implies calculating the stationary neutron distribution in the geometry of interest, from which the spatial power distribution can be computed. For a detailed account of the MC technique and the associated equations, the reader is referred to Section 2.1. Linked with the acronym “MC” is the expression “MC code”, here used to denote a piece of software implementing the MC solution technique.

The acronym “TH” is utilized to denote the calculation of the temperature and density scalar fields in the geometry of interest on a coarse mesh, *i.e.*, resolution of tenths of centimeters. This is performed by solving the fluid-dynamics and heat transfer equations reported in Section 2.2 at the fuel assembly or, eventually, at the sub-assembly level. These

equations are referred to as “TH equations” for the sake of brevity. A “TH code” is a piece of software solving the TH equations on a coarse mesh. The term “sub-channel code” is utilized as a synonym of “TH code”, according to legacy nomenclature employed in the nuclear reactor’s community.

Finally, the acronym “MC-TH” is used to describe the problem given by the simultaneous solution of the linear transport equation in criticality form with the MC technique, and the solution of the TH equations on a coarse mesh.

1.3 Literature Review

Four main approaches have been utilized to couple MC and TH solvers [5]. The simplest coupling strategy is denominated Operator Splitting method (OS). In the OS framework, the neutronics equation is solved to obtain the power profile by making an educated guess of temperature and density profile. The calculated power spatial profile is then fed into the TH equations as heat source and the corrected TH fields are obtained, *i.e.*, temperature and density profiles [6]. The OS, despite leveraging well-tested single physics codes and its simplicity of implementation, does introduce an inconsistency in the treatment of the non-linearity, *i.e.*, no feedback of the TH fields on the power profile is simulated, therefore leading to limited accuracy of the solution. The error is in fact proportional to the exponential of the commutator between the operator associated to the MC code and the TH code respectively [7].

An improvement over the OS is the Picard iteration method (PI) [8]. The latter consists in solving separately neutronics and TH equations like in the framework of the OS. However, the temperature and density spatial distributions calculated by the TH solver are fed back into the neutronic solver and the sequence neutronics-TH is repeated until the non-linear residual decays below a set tolerance. If the neutron transport equation is solved through MC, the power iterates are ”polluted” by stochastic noise that can undermine the algorithm’s convergence. This effect can be minimized by defining a dynamic underrelax-

ation factor. A theory to consistently define this factor was proposed by Dufek based on the Robbins-Monro's stochastic approximation [9, 10, 11]. The PI, despite being widely used for coupling MC with TH solvers, exhibits only a linear convergence rate in absence of noise [12]. This makes the PI relatively slow when compared to other methods with super-linear and quadratic convergence used in deterministic codes coupling, *e.g.*, Newton and Broyden method [12].

To obtain higher convergence rate, it was proposed to transition to the Jacobian-free Newton Krylov method (JFNK) [13] that has super-linear convergence and has been successfully used for deterministic neutronics-TH coupling within the MOOSE framework [14]. The JFNK is a pseudo-Newton method employing a first-order update of the Jacobian matrix, *i.e.*, evaluation of a Jacobian-vector multiplication, to cut down the memory and high computational requirements of the algorithm. Despite requiring less memory than the Newton method, its implementation is not straightforward in MC codes due to the noise associated to the Jacobian-vector product's estimation [15]. To the best of the author's knowledge, this technique was used only in a limited number of cases to perform full-core MC-TH coupled calculations [16, 17]. This is because the generation of the Jacobian-vector products is still computationally expensive, therefore undermining the potential gain in terms of number of transport calculations.

A method to improve the convergence rate without substantially increasing the complexity of the algorithm is to modify the Picard iteration method by including a prediction block between neutronics and TH solver [18]. The latter provides a better initial guess for the next MC calculation. Hermann et al., defined a predictor using a two-step approach, in which the multi-group cross-sections response to TH variations are predicted on-the-fly by using Support Vector Regression (SVR) [19]. The predicted cross-sections are inputted in a Coarse-Mesh-Finite-Difference (CMFD) solver to obtain the power profile that is then fed into a TH code to obtain temperature and density profile [20, 21]. The sequence SVR-CMFD-TH is repeated until the power profile converges within a prescribed tolerance. The

latter constitutes an improved guess for the fission source profile at the next Picard iteration therefore increasing the convergence rate of the full sequence. Despite the potential for faster convergence when compared to the PI, this approach relies on a problem-dependent training process for the SVR, a machine-learning technique, that is able to capture inter-nodal effects on the cross-sections response, therefore undermining the actual gain in speed obtained through the prediction block [18].

1.4 Goals and Organization of the Thesis

In this thesis, we develop a new method for the efficient and simple coupling of MC and TH/sub-channel codes. This goal is achieved by accelerating the classical Picard iteration scheme through the use of a deterministic, perturbation-based prediction of the power $\vec{Q}$ and the corresponding TH fields, *i.e.*, temperature $\vec{T}$ and density $\vec{\rho}$, that produces a better initial guess for the neutronic and TH fields at the next MC calculation, therefore accelerating the convergence of the whole algorithm. The prediction relies on a novel technique for the calculation of the cross-sections spatial distribution due to variations in the TH scalar fields. The latter technique is an original and novel contribution that relies on the definition of generalized transfer functions to calculate the cross-sections given a change in density and temperature profiles. In particular, it does not need any problem-dependent training as in the case of Herman, while still capturing non-local effects. The overarching goal can be broken down into three main objectives, listed below:

- **Objective 1.** Developing a novel computational framework for the calculation of macroscopic cross-sections, given general spatial density and temperature profiles. This methodology uses Generalized Transfer Functions (GTF) that can be calculated either with stochastic or deterministic codes.

- **Objective 2.** Implementing an efficient hybrid stochastic-deterministic method for coupled MC-TH calculations based on the modified Picard iteration scheme and to

test it against stylized mono-dimensional problems. The scheme leverages the computational framework for cross-sections calculation developed in the pursue of objective 1.

- **Objective 3.** Finally, the new hybrid scheme will be applied to perform three-dimensional MC-TH calculations.

The remainder of this dissertation is organized as follows. In Chapter 2, the fundamentals MC-TH coupling are outlined. Chapter 3 presents the theory for the GTF method, complemented by numerical experiments to show the ability of the method to capture the cross-sections' variation due to varying TH-fields. The GTF-based acceleration block is introduced in Chapter 4 together with implementation details. while Chapter 56 reports the results for 1D and 3D problems respectively. Finally, conclusions and potential directions for future work are addressed in Chapters 78.

CHAPTER 2

MC-TH COUPLED CALCULATIONS

The purpose of this chapter is to introduce the concepts and methodologies this thesis builds upon. In particular, the theory of the "elementary blocks" forming a MC-TH coupled solver are considered: MC methods for neutron transport are described in Section 2.1, sub-channel thermal hydraulic codes are dealt with in Section 2.2, while the Picard iteration methodology is explained in Section 2.3.2.

2.1 MC methods to solve the criticality problem

2.1.1 The Criticality Problem (CP)

The Linear Transport Equation (LTE) accurately describes the neutron transport in nuclear reactor cores. Using the notation employed by Lewis and Miller, the LTE in criticality form can be written as [22]:

$$\begin{aligned}\nabla \cdot \vec{J}(\vec{r}, E, \hat{\Omega}) + \Sigma_t(\vec{r}, E)\psi(\vec{r}, E, \hat{\Omega}) = \\ \int dE' \int d\Omega' \, \Sigma_s(\vec{r}, E' \to E, \hat{\Omega}' \cdot \hat{\Omega})\psi(\vec{r}, E', \Omega') \\ + \frac{1}{k}\frac{\chi(\vec{r}, E)}{4\pi} \int dE' \int d\Omega' \, \nu\Sigma_f(\vec{r}, E')\psi(\vec{r}, E', \hat{\Omega}'),\end{aligned} \tag{2.1}$$

where:

- $\vec{r}$, E, and $\hat{\Omega}$ represent the position vector, the neutron energy, and the unit direction vector, respectively.
- $\psi(\vec{r}, E, \hat{\Omega})$ is the angular neutron flux, representing the total distance traveled by neutrons included within a differential volume d^3r centered in $\vec{r}$ with an energy in the differential energy interval dE centered at E, traveling in direction in some differen-

tial solid angle $d^2\Omega$ around $\hat{\Omega}$, in a time interval dt.

- $\vec{J}(\vec{r}, E, \hat{\Omega}) = \hat{\Omega} \cdot \psi(\vec{r}, E, \hat{\Omega})$ is the angular current, signifying the number of neutrons within a differential volume d^3r centered around $\vec{r}$ with an energy in some differential energy interval dE centered around E, traveling in direction $\hat{\Omega}$ which is in some differential solid angle $d^2\Omega$ that pass through an infinitesimal area d^2A in a time interval dt.

- k is the multiplication factor, giving the asymptotic ratio between neutrons produced at generation n and $n+1$.

- $\Sigma_t(\vec{r}, E)$ is the total macroscopic cross-section.

- $\Sigma_s(\vec{r}, E' \to E, \hat{\Omega}' \cdot \hat{\Omega})$ is the scattering kernel.

- $\chi(\vec{r}, E)$ is the fission spectrum.

- $\nu\Sigma_f(\vec{r}, E')$ is the neutron production cross-section as a results of induced fission.

The LTE can be solved by imposing vacuum boundary conditions, for which neutrons cannot enter the reactor. If $\vec{r}_\partial$ denotes the boundary of the spatial domain, while $\hat{\Omega}_-$ is the incoming direction at the boundary $\vec{r}_\partial$, the vacuum boundary conditions can be written as

$$\psi(\vec{r}_\partial, E, \hat{\Omega}_-) = 0. \tag{2.2}$$

To take advantage of the problem's symmetry, reflective boundary conditions can be imposed, so that a null net current of neutrons pass through $\vec{r}_\partial$ leads to

$$\psi(\vec{r}_\partial, E, \hat{\Omega}_-) = \psi(\vec{r}_\partial, E, \hat{\Omega}_+), \tag{2.3}$$

where $\hat{\Omega}_+$ is the outgoing direction at the boundary $\vec{r}_\partial$. The CP consists in solving Eq. 2.1 subject to vacuum boundary condition, described by Eq. 2.2, or reflective boundary conditions, modeled by Eq. 2.3.

2.1.2 Monte Carlo methods for criticality calculations

Monte Carlo methods are a class of stochastic methods for the approximation of integral quantities. The first application of computational MC to particle transport dates back to 1947 when J. Von Neuman, E. Fermi, and S. Ulam together with other scientists at LANL wrote the first MC code to be run on ENIAC. The connection between MC, which is a technique to approximate integrals, and LTE can be seen by considering the integral form of the LTE. For the sake of mathematical simplicity, we will consider the case of isotropic scattering. This is because this simplification allows to obtain a correct final expression for the scalar flux $\psi(\vec{r}, E) = \int d^2\Omega\psi(\vec{r}, E)$ with lower mathematical overhead. In integral form, Eq. 2.1 can be recast in the following form [23]:

$$\Sigma_t(\vec{r}, E)\psi(\vec{r}, E) = \int \left[\Sigma_t(\vec{r}', E')\psi(\vec{r}', E')C(\vec{r}', E' \to E)T(\vec{r}' \to \vec{r}, E')\right] d^3r', \tag{2.4}$$

where:

- $T(\vec{r}' \to \vec{r}, E')$ is the transport kernel:

$$T(\vec{r}' \to \vec{r}, E') = \Sigma_t(\vec{r}, E)\, e^{-\int \Sigma_t(\vec{r}'+s\hat{\Omega},E)ds)}\, \delta\left(\hat{\Omega} \cdot \frac{\vec{r} - \vec{r}'}{\|\vec{r} - \vec{r}'\|} - 1\right). \tag{2.5}$$

- $C(\vec{r}', E' \to E)$ is the collision kernel:

$$C(\vec{r}', E' \to E) = \frac{\Sigma_s(\vec{r}, E' \to E)}{\Sigma_t(\vec{r}, E)} + \frac{\chi(\vec{r}, E)\nu\Sigma_f(\vec{r}, E)}{4\pi\Sigma_t(\vec{r}, E)}. \tag{2.6}$$

Eq. 2.4 can be rewritten more succinctly by using $p = (\vec{r}, E)$ to denote a point in the phase space, ϕ to represent the collision density $\Sigma_t\psi$, and defining the operator R given by

the composition of the transport and collision kernel:

$$\phi(p) = \int \phi(p')\ R(p' \to p) dp' \tag{2.7}$$

If now we expand the collision density in components having $0, 1, ..., k$ collisions, where ϕ_0 is therefore associated to the uncollided scalar flux, we obtain the following equation for $k \geq 0$:

$$\begin{aligned} \phi_k(p) &= \int \phi_{k-1}(p') R(p' \to p) dp' \\ &= \int\ dp_0 ... \int dp_{k-1}\ \phi_0(p_0) R(p_0 \to p_1)\ R(p_1 \to p_2) ... R(p_{k-1} \to p) \end{aligned} \tag{2.8}$$

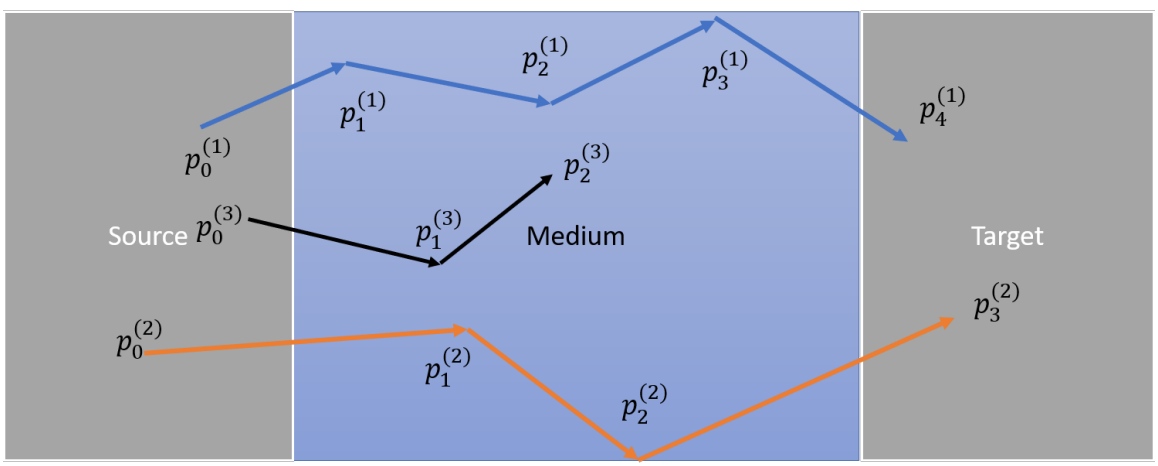

Figure 2.1: Illustration of random walks.

Eq. 2.8 expresses the concept that neutron transport is a Markovian process, in which a state p_k depends only on the previous p_{k-1}. In addition, the state p_k can be deduced from a probability density function $R(p_{k-1} \to p_k)$,that is therefore a transition probability. The concatenation of the collision-transport transitions, called a random walk, allows to compute the final state p_k from p_0. In other words, the MC approach consists in drawing a series of state points $\{p_k\}_{k=0,...,N}$ from a set of probability density function (pdf) resulting in a random walk. The results of M random walks is then used to estimated the expected

value of a quantity of interest and the associated uncertainty, by exploiting the results of the central limit theorem. In the example reported in Figure 2.1, we are interested in calculating the expected number of neutrons that, generated from the source, are absorbed in target after flying through a non-multiplying medium. The main conceptual steps are reported below:

1. The pdf describing the phase-space distribution of the neutrons in the source, denoted as $\phi_0(p_0)$, is used to determine the location, energy, and direction of the neutron initiating the history, *i.e.*, p_0. This can be done with rejection or inverse transform sampling [1].

2. The neutron is transported in the medium. This is operatively done by drawing a second state point in the random walk p_1 from the transition probability $R(p_0 \to p)$.

3. Three possible scenarios can arise at the state point p:

   - If the neutron is absorbed in the target, the counter A, associated to the number of particles absorbed, is incremented and the history terminated.
   - Likewise, the history is terminated if the particle exits the domain. However, the counter is not incremented.
   - The particle is neither absorbed nor exits the domain. Step 2 is repeated until the criteria for the history termination are met.

4. Step 1-3 are repeated M times, therefore obtaining M histories.

5. The expected number of particles absorbed in the target $\bar{A}$ can then be estimated through sample average:

$$\bar{A} = \int \Sigma_a(p)\psi(p)dp \approx \frac{1}{M}\sum_{m=0}^{M}\left(\sum_k \Sigma_a(p_k^{(m)})\psi(p_k^{(m)})\right). \tag{2.9}$$

Together with the corresponding variance:

$$\sigma_A^2 = \frac{1}{M-1}\sum_{m=0}^{M}\left(\sum_k (\Sigma_a(p_k^{(m)})\psi(p_k^{(m)}) - \bar{A})^2\right). \tag{2.10}$$

Despite being theoretically correct, Eq. 2.10 is not used in practice. This is because $\bar{A}$ is not known before the end of the calculation. Instead, the variance is estimated by accumulating scores and scores-squared of the tallied quantity of interest. Ref. [1] provides further details concerning the practical implementation of computational MC methods for particle transport.

2.1.3 Solving the CP: Power Iteration

In order to introduce the power iteration method, let us write Eq. 2.1 in a more succinct way by leveraging operator notation. Let $\mathcal{L}$ denote the loss operator including the reaction, streaming, and scattering contribution:

$$\begin{aligned}\mathcal{L}\psi(\vec{r}, E, \hat{\Omega}) = &\ \nabla \cdot \vec{J}(\vec{r}, E, \hat{\Omega}) + \Sigma(\vec{r}, E)\psi(\vec{r}, E, \hat{\Omega}) \\ &- \int dE' \int d\Omega'\ \Sigma_s(\vec{r}, E' \to E, \hat{\Omega}' \cdot \hat{\Omega})\psi(\vec{r}, E', \Omega'),\end{aligned} \tag{2.11}$$

while the multiplication operator $\mathcal{M}$ accounts for the fission neutrons' production:

$$\mathcal{M}\psi(\vec{r}, E, \hat{\Omega}) = \int dE' \int d\Omega'\ \nu\Sigma_f(\vec{r}, E')\psi(\vec{r}, E', \hat{\Omega}'). \tag{2.12}$$

Therefore, Eq. 2.1 can be rewritten as:

$$\begin{aligned}\mathcal{L}\psi(\vec{r}, E, \hat{\Omega}) &= \frac{1}{k}\frac{\chi(\vec{r}, E)}{4\pi}\mathcal{M}\psi(\vec{r}, E, \hat{\Omega}) \\ &= \frac{1}{k}S(\vec{r}, E, \hat{\Omega}),\end{aligned} \tag{2.13}$$

where $S(\vec{r}, E, \hat{\Omega})$ is the fission source distribution. Within the power method framework, a

first guess $S_0(\vec{r}, E, \hat{\Omega})$ of the fission source and the multiplication factor k_0 is made. The iterative sequence is then defined for $n \geq 0$:

$$\mathcal{L}\psi_n(\vec{r}, E, \hat{\Omega}) = \frac{1}{k_{n-1}} S_{n-1}(\vec{r}, E, \hat{\Omega}), \tag{2.14}$$

where the S_n is given by:

$$S_n = \mathcal{M}\psi_n(\vec{r}, E, \hat{\Omega}), \tag{2.15}$$

and the multiplication factor can be updated through the ratio:

$$k_n = k_{n-1} \frac{\int d^3r \int dE \int d^2\Omega S_n(\vec{r}, E, \hat{\Omega})}{\int d^3r \int dE \int d^2\Omega S_{n-1}(\vec{r}, E, \hat{\Omega})}. \tag{2.16}$$

The sequence is repeated until:

$$\frac{\|S_n - S_{n-1}\|}{S_{n-1}} < \tau, \tag{2.17}$$

where τ is a set tolerance. The convergence to the dominant eigenpair $\{S, k\}$ is ensured if k is strictly greater in magnitude than the other eigenvalues of $\mathcal{K} = \mathcal{L}^{-1}\,\mathcal{M}$ and the starting vector S_0 has a nonzero component in the direction of an eigenvector S. The convergence of the sequence is geometric and is dominated by the ratio between the two eigenvalues with larger real component, denominated the dominance ratio. The closer is the dominance ratio to unity, the slower is the convergence to the dominant eigenpair. This situation usually arises in large thermal reactor, where the neutrons exploration of the phase-space is less effective compared to systems with higher neutrons' mean free path [24]. Minimizing the number of MC simulations within MC-TH coupled simulations is therefore particularly important for this type of reactor, where even a single MC calculation can be extremely expensive.

2.1.4 Power Iteration in Monte Carlo Calculations

In the context of Monte Carlo simulations, the power method is known as the method of successive generation and was introduced in 1949 by Lieberoth et al [25]. Since the fission source is unknown, the first algorithmic step is to make an initial guess for the source's and the eigenvalue's phase-space distribution. Neutrons are then sampled from the initial distribution and transported through the medium. The transport consist in sampling from the pdf associated to the transport and collision operator described in Section 2.1.2. If the neutron exits the domain or is absorbed, the neutron history is terminated. If the absorption occurs in a fissile material, the number of fission neutrons born from the collision is sampled together with their energy and direction. The information on the position, energy, direction, and, eventually, statistical weight of the fission-generated particles is stored to define the next generation fission source. The sequence of steps, also known as criticality cycles, is repeated until a pre-set number of generations are run or a set tolerance is met. Among the codes that implement the power method are the standard continuous energy Monte Carlo codes for neutron transport, such as MCNP [26], Serpent [27], SCALE/KENO [28], and OpenMC [29]. It is noticeable that the user must impose the number of histories per generation, *i.e.*, neutron population, and the total number of generations. A poor choice of these parameters can lead to a biased solution, or convergence to erroneous results, mainly due to a violation of the central limit theorem. This happens because of insufficient number of simulated particles, leading to inter-cycle or spatial correlation *e.g.*, see Refs. [30, 31, 32, 33, 34]. These issues are amplified for systems with high-dominance ratio, *i.e.*, ratio of the second largest eigenvalue to the maximum eigenvalue, or optically thick reactors, where the neutrons exploration of the phase-space is less effective [24]. In these cases, a prohibitively large number of particles and cycles may be required to ensure convergence with acceptable uncertainty [35, 36].

2.2 Sub-channel TH codes

Sub-channel thermal hydraulic codes allow to solve the equations describing heat transfer and fluid dynamics at the assembly and the unit-cell level in a nuclear reactor. The solution of these equations allows to calculate the spatial distribution of temperature, pressure, density, and mass flow rate from which quantities of interests for the safety and the operation of the nuclear reactor can be computed. Among these are the Departure for Nuclear Boiling (DNB) for Light Water Reactors (LWRs), and the maximum temperature of the fuel.

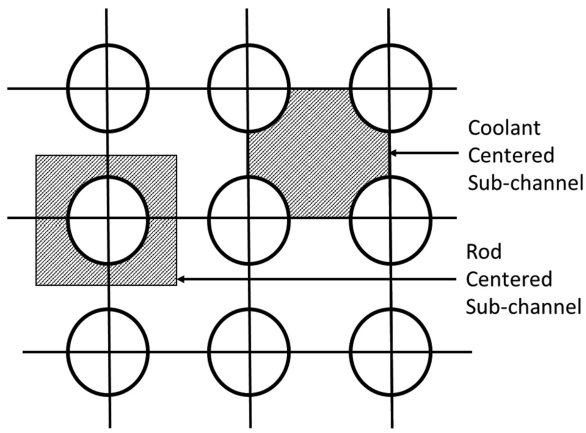

Figure 2.2: Typical mesh for sub-channel code [37].

Sub-channel codes rely on the definition of vertical structures, called ”sub-channels”. The latter are usually distinguished between coolant-centered sub-channels and rod-centered sub-channels, as illustrated in Fig. 2.2. Additional types of sub-channels can be defined to capture the flow at the periphery of the assembly. A structured coarse mesh in the axial direction, *i.e.*, z axis, to describe the temperature axial distribution is usually added. Eventually, a second staggered grid is superimposed to describe the pressure loss at different axial levels. Using this space mesh, the equations for the mass, momentum, and heat transfer are solved.

2.2.1 Radial Heat Transfer

The equation describing heat conduction for an arbitrary domain is:

$$\rho c_p \frac{\partial T}{\partial t} = \nabla \cdot \ \lambda \nabla T + Q, \tag{2.18}$$

where all the quantities depend on space and time and:

- ρ is the mass density.
- c_p is the heat capacity.
- λ is the heat conductivity.
- T is the temperature.
- Q is the volumetric heat source. The heat source is connected to the scalar neutron flux $\psi(\vec{r}, E, \hat{\Omega}, t)$ by the following relation:

$$Q(\vec{r}, t) = \frac{1}{V} \int d^3r' \int d^2\Omega \int dE \ k_Q(\vec{r}' \rightarrow \vec{r}, t) \Sigma_f(\vec{r}, E, t) \psi(\vec{r}, E, \hat{\Omega}, t), \tag{2.19}$$

  in which $k_Q(\vec{r}' \rightarrow \vec{r})$ is a kernel describing the fission energy deposition and V is the volume in which the heat source is defined. In this thesis, we will assume local deposition, and, therefore, the kernel reduces to $k(\vec{r}', t)$. In particular, gamma deposition is not considered as it does not affect the methodology here outlined.

In steady-state conditions, Eq. 2.18 can be solved by using the circuit-equivalent model that exploits the analogy between the heat and electric charge conservation equations. The thermal-electric analogy is illustrated in Table 2.1, where electric fields and analogous thermal quantities are reported in each column. Conceptually, the thermal-electric analogy provides an explanation of heat transfer in terms of temperature difference as driving force, analogously to what occurs in charge transfer with the electric potential difference.

Table 2.1: Thermal-electric analogy.

Current, I_e	Voltage, V_e	Resistance, R_e
Heat Flux, Q	Temperature, T	Thermal Resistance, R_t

Using the thermal-electric equivalence, in steady-state conditions, the temperature decrease from fuel center-line temperature T_f^c and the external coolant temperature T_c^f is given by:

$$T_\infty^c = T_c^f - R_{t,eq}Q, \tag{2.20}$$

where $R_{t,eq}$ is an equivalent thermal resistance. The use of the circuit-equivalent method makes the modeling of the heat transfer intuitive when using structured mesh. In Fig. 2.3, the equivalent circuit used to calculate the radial temperature spatial distribution is illustrated. The geometry is discretized into concentric layers and the axial conduction is neglected. To each layer, a thermal resistance is then associated and the equivalent resistance is simply calculated using the formula for series resistances.

$$R_{t,eq} = \sum_i R_{t,i} \tag{2.21}$$

The definition of the single resistances in terms of known properties is a function of three factors: (1) The material, (2) The phenomenon regulating the heat transfer, (3) The geometry. For conduction through a cylindrical shell with inner radius r_1 and outer radius r_2, the resistance has the following definition:

$$R_t = \frac{1}{2\pi\lambda L} ln(r_2/r_1), \tag{2.22}$$

where λ is the conduction value in W/m/K for the material located within [r1, r2]. In the case of convection, the resistance has a simple formulation:

$$R = \frac{1}{hA}, \tag{2.23}$$

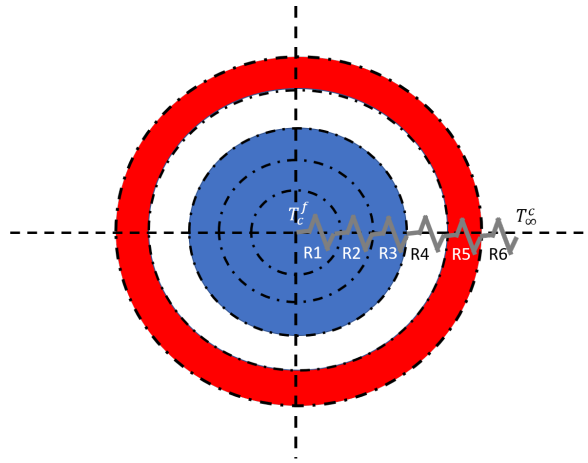

Figure 2.3: Thermal-electric analogy for fuel pin.

in which h is the heat transfer coefficient that regulates the convective heat transfer at the interface between the solid and fluid, and A is the heat exchange area. The heat transfer coefficient can be estimated based on semi-analytical arguments and empirical correlations. For instance, the Dittus-Bölter can be utilized to describe the conjugate heat transfer for smooth cylindrical ducts in single phase flow:

$$\frac{hD_H}{\lambda} = C\ Re^a\ Pr^b, \tag{2.24}$$

where:

- Re is the Reynolds number describing the ratio between inertial and viscous forces. If u denotes the average fluid speed, D_H is the hydraulic diameter, and ν is the kinetic viscosity, the Reynolds number is described by the following relation:

$$Re = \frac{uD_H}{\nu} \tag{2.25}$$

- Pr is the Prandtl number characterizing the relative importance of heat and viscous

mass transfer. If $\alpha_t = \frac{\lambda}{\rho c_p}$ is the thermal diffusivity:

$$Pr = \frac{\alpha_t}{\nu_t} \tag{2.26}$$

- C, a, and b are three empirical coefficients.

When two-phase flow occurs, Eq. 2.24 cannot adequately describe the heat transfer from the fuel assemblies to the coolant. In particular, the correlation to be utilized strongly depends on the flow regime. A synopsis of the different heat transfer regimes for water up-flowing in a uniformly-heated vertical duct is reported in Fig. 2.4. In the latter figure, the coolant enters the duct in sub-cooled state, *i.e.*, $T < T_{sat}$. Then, at a certain height the wall becomes superheated and bubbles start forming at the solid-liquid interface. The turbulence created by the bubble detaching from the interface increases the heat transfer rate between the heat source and the coolant leading to an increase in temperature until the saturation temperature T_{sat} is reached. A saturated nucleate boiling regime onsets during which temperature remains constant and bubbles coalesce into larger bubbles, eventually giving rise to slug or churn flow. As boiling continues, liquid and vapor stratify: the liquid form a thin film at the interface, while a core of vapor is formed. Eventually, the liquid layer can get completely depleted, leading to an abrupt decrease of the heat transfer coefficient, conventionally denoted as dryout condition. This situation of dryout can arise both at high and low quality vapor, depending on the level of the heat flux. The qualitative trend of the heat transfer trend is depicted in Fig. 2.5.

Reporting the numerical correlations associated to every flow regime presented in this section is beyond the scope of this thesis. Reference [38] reports heat transfer correlations for each of the flow regimes described in this section.

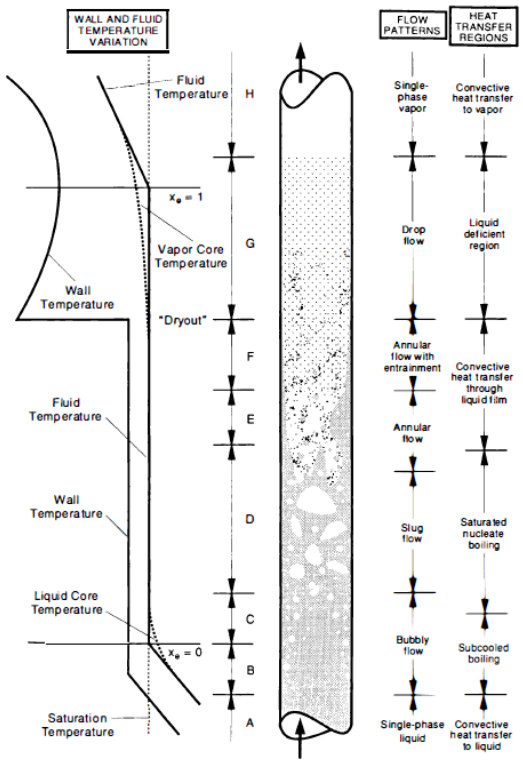

Figure 2.4: Different flow and heat transfer regime for heated vertical duct with uniform axial heat transfer and forced convection [38].

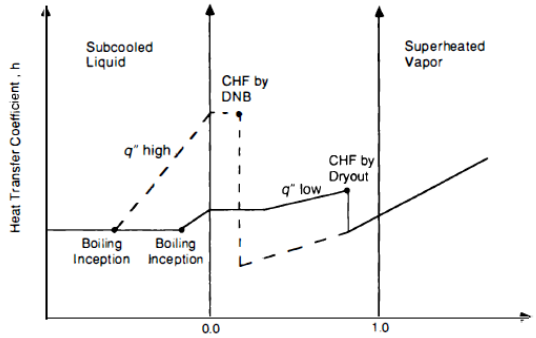

Figure 2.5: Qualitative trend of heat transfer coefficient for different magnitude of the heat source as a function of quality [38].

2.2.2 Axial Temperature

The axial temperature distribution can be computed through the use of the first principle of thermodynamics applied to an axial cell, conventionally called a node. If T_∞^j and T_∞^{j+1} are the inlet and outlet temperature respectively, the following equation can be written to

describe the relation between the outlet and inlet node temperature:

$$T_{\infty}^{j+1} = T_{\infty}^{j} + \frac{Q_j V_j}{\dot{m} c_{p,j}}, \tag{2.27}$$

where:

- $\dot{m}$ is the mass flow rate,
- Q_j is the volumetric power associated to the jth node,
- $c_{p,j}$ is the node-averaged specific heat capacity associated to the jth node.

Eq. 2.27 is valid only for single phase flow. It can be generalized for two-phase flow by expressing the relation in terms of enthalpy. A depiction of the calculation procedure along a channel is reported in Fig. 2.6, where the exit temperature at the upstream node is used as entering temperature for the node above. Eq. 2.27 is valid if we assume negligible losses due to changes in kinetic energy and gravitational potential. This makes it a good approximation for LWRs, while additional terms may be needed for gas-cooled reactors. Moreover, notice that the specific heat capacity depends on the temperature of the coolant itself and the pressure. This makes Eq. 2.27 a non-linear relation.

2.2.3 Axial Pressure Loss

The axial pressure spatial distribution is calculated by distinguishing different sources of loss and assuming superposition of the effects.

- The friction pressure loss Δp_{fric} is linked to the loss of pressure due to the interaction of the fluid with the solid surface.
- The gravitational pressure loss Δp_{grav} is due to the gravitational potential's variation.
- The acceleration pressure loss Δp_{acc} is due to the change in the kinetic energy.
- The form pressure loss Δp_{form} due to abrupt changes in the area cross-section.

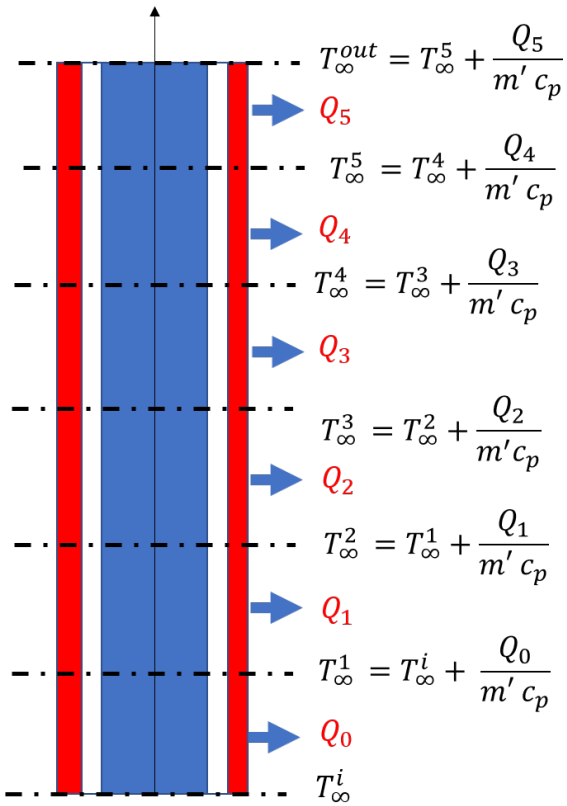

Figure 2.6: Axial temperature calculation.

The final equation for the pressure loss is then:

$$\Delta p_{tot} = \Delta p_{fric} + \Delta p_{grav} + \Delta p_{acc} + \Delta p_{form} \tag{2.28}$$

In this section, an overview of the fundamental equations to compute these four contributions are provided. Emphasis will be given to correlations utilized in LWR reactors' analysis. This will allow to better understand the results reported in Chapters 56, where BWR and PWR-based problems are analyzed.

Friction Loss

The friction losses, caused by the interaction of the fluids with the solid, are proportional to the variation of the fluid's kinetic energy through an empirically-defined coefficient, called

Darcy's factor. The following conventional mathematical formula is utilized:

$$\Delta p_{fric} = f \frac{L}{D_H} \frac{\dot{m}^2}{2\rho_m}, \tag{2.29}$$

where:

- f is the Darcy friction factor.
- L is the length of the duct section.
- D_H is the hydraulic diameter.
- $\dot{m}$ is the fluid mass flow rate.
- ρ_m is an average coolant density. An expression to define this quantity in two-phase flow will be defined in Section 2.2.3

The definition of the friction factor depends on: (1) The flow regime, *i.e.*, laminar or turbulent, as determined from the value of the Reynolds number (2) The roughness of the tube, (3) The geometry of the domain of interest, (4) The fluid physical properties. An example of f definition is the Colebrook equation:

$$\frac{1}{\sqrt{f}} = -2\log_{10}\left(\frac{\frac{\epsilon}{D_H}}{3.70} + \frac{2.51}{Re\sqrt{f}}\right), \tag{2.30}$$

where ϵ is the duct's roughness.

In two-phase flow, the general approach is to define additional parameters denominated two-phase multipliers ϕ_{LO}^2 and ϕ_{GO}^2 linking the total friction pressure loss $\left(\frac{dp}{dz}\right)_T$ and the one caused by the single phases, with flow rate matching the total two-phase mass flow rate. The multipliers, the total pressure loss, and the single-phase losses are linked by the

following relation

$$\left(\frac{dp}{dz}\right)_T = \phi_{LO}^2 \left(\frac{dp}{dz}\right)_L \\ \phi_{GO}^2 \left(\frac{dp}{dz}\right)_V, \tag{2.31}$$

where the L and V are subscript associated to the liquid and the vapor, respectively. The multipliers can be calculated through empirical correlations. The most known of these correlations is the one developed by Lockhart-Martinelli in 1949 that expresses the multipliers as a function of the parameter X, called the Martinelli parameter [38]

$$X = \frac{\left(\frac{dp}{dz}\right)_L}{\left(\frac{dp}{dz}\right)_V}. \tag{2.32}$$

The relation between the multipliers and the parameter X is reported in Fig. 2.7 as calculated by Lockhart.

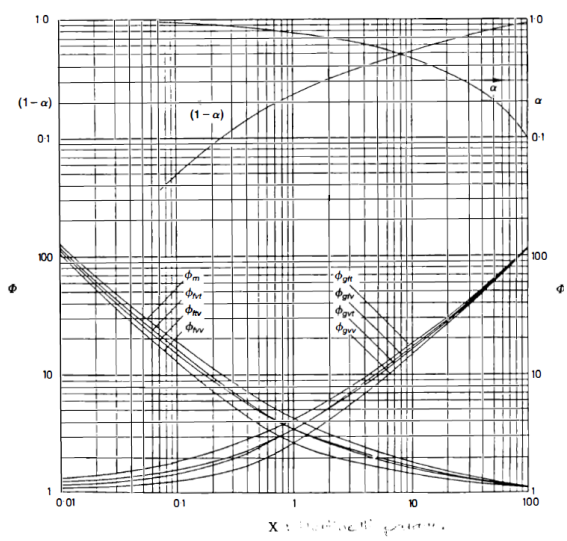

Figure 2.7: Lockhart-Martinelli relation [39].

More refined correlations can be defined to improve the model's fidelity. Among these is the Chisholm correlation:

$$\phi_{LO}^2 = 1 + \frac{C}{X} + \frac{1}{X^2}, \tag{2.33}$$

where C, named C-factor, is a parameter originally tabulated as a function of the fluid properties and the geometrical characteristics of the duct. The modified Chisholm correlation, gives a formula of C as a function of the Reynolds number and the Martinelli parameter

$$C = aX^b, \tag{2.34}$$

in which the coefficients $a = -2.44 + 0.00939\ Re_{LO}$ and $b = -0.938 + 0.00432\ Re_{LO}$ are a function of the Reynolds' number $Re_{LO} = (\dot{m}\ D_H)/\mu_L$. More refined models including the mass exchange between the vapor and liquid phases and the different flow patterns can be utilized, such as the ones provided by the US vendors [38].

Acceleration Losses

The acceleration losses are due to variations of the fluids kinetic energy. Mathematically, we can express this contribution as:

$$\left(\frac{dp}{dz}\right)_{acc} = \frac{d}{dz}\left(\frac{\dot{m}^2}{\rho_m}\right) = \frac{d}{dz}\left(\rho_m\ v^2\right). \tag{2.35}$$

The acceleration losses are not negligible either when the coolant reaches speeds in the order of the speed of sound starting from low speed condition, *i.e.*, high velocity gradients, or when phase change occurs, *i.e.*, high density gradients.

A consistent formulation for the effective density ρ_m is not straightforward. In fact, a suitable average, compatible with the conservation laws must be defined. The first approach that can be used to define an effective two-phase density is the Homogeneous Equilibrium Model (HEM). In the framework of the HEM, the two phases are assumed to be in thermodynamic equilibrium and dynamic equilibrium, *i.e.*, temperature and average velocity are equal in a cross-section of the duct. The model is a good approximation to describe flows driven by high pressure gradients, or other potential differences, where the two-phases are

highly mixed. In this case, the density ρ_m can be described by the following relation:

$$\frac{1}{\rho_m} = \frac{x}{\rho_g} + \frac{1-x}{\rho_l}, \tag{2.36}$$

where x is the vapor quality defined as:

$$x = \frac{m_v}{m_v + m_l}. \tag{2.37}$$

In Eq. 2.37, m_v and m_l denote the vapor and liquid mass respectively.

The separated flow model (SFM) is an alternative model that considers thermal equilibrium between the two phases, but different velocities. With this approximation, the density can be defined as:

$$\frac{1}{\rho_m} = \frac{x^2}{\{\rho_v\ \alpha\}^2} + \frac{(1-x)^2}{\rho_l\ \{1-\alpha\}^2}, \tag{2.38}$$

where $\{\alpha\}$ is the area-averaged void fraction. The latter parameter expresses the fraction of cross-sectional area occupied by the vapor over the total area. The void fraction can be correlated to the vapor quality and the density of the single phases through the following equation:

$$\{\alpha\} = \frac{1}{1 - \frac{1-x}{x}\frac{\rho_v}{\rho_l}S} \tag{2.39}$$

where S is the slip ratio, *i.e.*, ratio of the area and time averaged speed of the vapor and liquid phase. Naturally, the slip ratio is unitary for the HEM model. However, S can be sensibly different from unity, when the phases are highly segregated, *e.g.*, in churn/slug flow, and the pressure gradients along the ducts are not extremely high. In this case, empirical correlation such as Martinelli-Nelson, or CISE correlation are utilized to obtain the slip ratio as a function of the vapor quality.

Gravity Pressure Losses

The gravity pressure losses $\left(\frac{dp}{dz}\right)_{grav}$ are due to a change in gravitational potential along the duct. Applying the definition weight force on a fuel section in a duct with constant cross-sectional area, we obtain the following definition for this term:

$$\left(\frac{dp}{dz}\right)_{grav} = \frac{d}{dz}\left(\rho_H \; g \; dz \; sin(\theta)\right), \tag{2.40}$$

where:

- θ is the angle between the duct symmetry axis and the horizontal plane.
- g is the gravitational acceleration.
- ρ_m is an effective density.

The effective density can be defined according to Eqs. 2.36-2.38. Alternatively, a simplified formulation can be utilized:

$$\rho_m = \{\alpha\} \; \rho_v + \{1 - \alpha\} \; \rho_l \tag{2.41}$$

Form Pressure Losses

The form pressure losses are used to describe the pressure drop connected to an abrupt change in flow area. This contribution appears in presence of spacer grids utilized in nuclear reactors. If A_s and A_v denote the restricted and unrestricted area respectively, then:

$$\left(\frac{dp}{dz}\right)_{form} = C_s \; \frac{A_v}{A_s} \frac{\dot{m}^2}{\rho_m}, \tag{2.42}$$

where C_s is a modified drag coefficient, dependent on the flow regime, *i.e.*, turbulent or laminar, and the spacers' geometry. Examples of this correlations can be found in [38].

2.3 MC-TH coupling through Picard iteration

The Picard iteration scheme, also denominated fixed point iteration, is a classical technique to solve systems of non-linear equations cast in the form [12]:

$$\vec{\xi} = \mathcal{G}\{\vec{\xi}\}, \tag{2.43}$$

where $\vec{\xi}$ is the vector of unknowns and $\mathcal{G}$ is a non-linear operator acting on the vector $\vec{\xi}$. In Section 2.3.1, the neutronics-TH coupled problem is reduced to the fixed-point form of Eq. 2.43. The PI algorithm is then introduced in Section 2.3.2, while consideration on the algorithm's convergence and the use of under-relaxation scheme are reported in Section 2.3.3.

2.3.1 Reduction of neutronics-TH Problem to Fixed-point Iteration

Let $\vec{Q}$ be the vector containing the node-wise heat source spatial distribution and $\mathcal{T}\{\cdot\}$ the sub-channel code operator, returning the node-wise temperature and density distribution in the reactor when applied to the heat source distribution. Then, we obtain the following equation:

$$[\vec{T}, \vec{\rho}] = \mathcal{T}\{\vec{Q}\}, \tag{2.44}$$

where $\vec{\rho}$ and $\vec{T}$ denote the density and temperature spatial distributions. The definition of the neutronic operator $\mathcal{P}$, returning the heat source given temperature and density, and the use of Eq. 2.44 leads to the following equation:

$$\begin{aligned} \vec{Q} &= \mathcal{P}\{\vec{T}, \vec{\rho}\} = \\ &= \mathcal{P} \circ \mathcal{T}\{\vec{Q}\} \end{aligned}. \tag{2.45}$$

Finally, the definition of the composed operator $\mathcal{C} = \mathcal{P} \circ \mathcal{T}$ leads to the neutronics-TH problem in fixed-point form:

$$\vec{Q} = \mathcal{C}\{\vec{Q}\}. \tag{2.46}$$

The power profile satisfying Eq. 2.46 is called a fixed point and it coincide with the eigenvector corresponding to the unitary eigenvalue of the operator $\mathcal{C}$. When Monte Carlo codes are utilized to calculate the neutronic solution, stochastic noise is added to the iterates, therefore transforming the deterministic operator $\mathcal{C}$ in a random mapping and the vector $\vec{Q}$ into a random variables. Despite not changing the formal description of the problem given in Eq. 2.46, the presence of the noise can compromise the convergence of the algorithm [40]. Considerations on this topic are given in Section 2.3.3.

2.3.2 Picard Iteration Algorithm

The PI consists in introducing an initial guess $\vec{Q}_0$ and defining the following recursive series for $n \geq 0$:

$$\vec{Q}_{n+1} = \mathcal{C}\{\vec{Q}_n\}. \tag{2.47}$$

Alg. 1 reports the pseudo-code for the algorithm when applied to the neutronics-TH problem and single-physics codes are leveraged. As noticeable, an initial guess $\vec{Q}_0$ for the power profile is made and fed into the TH code from which temperature and density are obtained. The latter are then inputted into the MC solver to obtain an updated power distribution $\vec{Q}_1$. If the relative residual:

$$res = \max\{res_Q, res_T, res_\rho\}, \tag{2.48}$$

where:

- res_Q is the L2 norm of the power relative residual.

- res_T is the L2 norm of the temperature relative residual.

- res_ρ is the L2 norm of the density relative residual.

For a variable X, the associated L2 norm of the relative residual is defined as follows:

$$res_X = \frac{\left\|\vec{X}_1 - \vec{X}_0\right\|_2}{\left\|\vec{X}_0\right\|_2}, \tag{2.49}$$

where $||\cdot||_2$ denotes the L2 norm operator. If res is below the preset tolerance τ, the sequence is converged. Otherwise, the power profile is updated and the sequence of operations 34 is repeated. It must be noticed that the algorithm can be stated in terms of TH fields instead of power profile. This is equivalent to the approach here described if we make the choice $\vec{Q}_0 = \mathcal{T}\{\vec{T}_0, \vec{\rho}_0\}$, where $\vec{T}_0$ and $\vec{\rho}_0$ are the initial temperature and density guesses.

Algorithm 1 Standard Picard Iteration Algorithm.

```
Initial guess: Q⃗_0
while n < N_max res > tol do
    [T⃗, ρ⃗] = T{Q⃗_0}
    Q⃗_1 = P{T⃗, ρ⃗}
    if res < τ then
        return
    else
        Q⃗_0 = Q⃗_1
    end if
end while
```

2.3.3 Convergence of PI and stochastic approximation

There is a vast literature concerning the convergence of fixed-point iteration schemes [41]. In general, for the Banach fixed point iteration theorem, if the operator $\mathcal{C}$ is a contraction mapping, then there exists only one fixed point of $\mathcal{C}$ and the PI converges to it [12]. Formally, let $\left\|\vec{Q}_l - \vec{Q}_{l-1}\right\|$ denotes the distance between two power profiles at consecutive

iterations $l-1$ and l in a suitable metric, then the operator $\mathcal{C}$ is a contraction operator if:

$$\left\| \mathcal{C}\{\vec{Q}_l\} - \mathcal{C}\{\vec{Q}_{l-1}\} \right\| \leq q \left\| \vec{Q}_l - \vec{Q}_{l-1} \right\|, \tag{2.50}$$

where q is a real number in the interval $[0, 1)$, called a Lipshitz constant. Physically, this means that the PI converges if the system has negative feedback to local power variation/fluctuation. In other words, if a power variation from the fixed point occurs in the reactor, its effect will be dampened and eventually nullified for $n \to \infty$. If condition 2.50 holds, the Banach fixed point iteration theorem states that there exists a unique fixed point $\vec{Q}^*$, and the rate of convergence is linear.

If the operator is not a contraction, *i.e.*, $q \geq 1$, the Picard iteration may not converge and if it does, it may converge to a value that is not a fixed point of the neutronics-TH operator $\mathcal{C}$. This circumstance may arise due to numerical errors in the estimate of the action of the operator $\mathcal{C}$ due to the MC noise when the Lipschitz constant is close to unity or because the operator $\mathcal{C}$ is intrinsically not a contraction. In this circumstances, a more reliable sequence such as the one generated by the Mann iteration scheme is needed [40]:

$$\vec{Q}_{n+1} = \omega_n \, \vec{Q}_n + (1 - \omega_n) \mathcal{C} \, \vec{Q}_n, \tag{2.51}$$

where ω_n is a weighting factor depending on the iteration number. The Mann iteration, is equivalent to weighting two successive iterates generated by the Picard iteration scheme, $\vec{Q}_n$ and $\vec{Q}_{n+1} = \mathcal{C} \, \vec{Q}_n$. In particular, for $\omega_n = 1/n$ we obtain the Robbins-Monro scheme [9] that ensures almost-sure convergence of the iterates to a fixed point of the neutronics-TH composed operator $\mathcal{C}$ even for noise-corrupted Picard iterates. The original Picard algorithm is modified as reported in Alg. 2 to include the Robbin-Monro relaxation. The scheme will be utilized in this paper to obtain the reference solution for the coupled neutronics-TH system of equations.

Algorithm 2 Picard Iteration Scheme with Robbins-Monro Relaxation.

Initial guess: $\vec{Q}_0$
while $n < N_{max}$ $res > tol$ **do**
  $[\vec{T}, \vec{\rho}] = \mathcal{T}\{\vec{Q}_0\}$
  $\vec{Q}_1 = \mathcal{P}\{\vec{T}, \vec{\rho}\}$
  if $res < \tau$ **then**
    return
  else
    $\vec{Q}_1 := \frac{1}{n}\,\vec{Q}_0 + \left(1 - \frac{1}{n}\right)\,\vec{Q}_1$
    $\vec{Q}_0 := \vec{Q}_1$
  end if
end while

CHAPTER 3

GENERALIZED TRANSFER FUNCTIONS METHOD

This chapter lays down the theoretical bases of the Generalized Transfer Function method. In particular, its application to macroscopic cross-sections prediction is considered. Theoretical explanations will be complemented by supporting results obtained for mono-dimensional problems. The chapter closely follows the theory exposed in Ref. [42][43].

The remainder of the chapter is structured as follows. The problem statement and basic definitions are provided in Section 3.1, while the GTF theory is outlined in Section 3.2. This is followed by preliminary results obtained on a BWR unit-cell problem in Section 3.3 with non-uniform fuel enrichment. Finally, the main results of this chapter are highlighted in Section 3.5.

3.1 Problem statement

Let D be the physical space occupied by the reactor's core and $\{D_i\}_{i=0,\dots,N}$ a finite number of disjoint regions in D, called "nodes", such that $D = \bigcup_{i=0}^{N} D_i$. In this work, any function defined on D is node-wise constant. The theory here developed can easily be adapted for continuous functions, *i.e.*, non-constant node-wise functions, by using the notation employed in Ref. [42]. We can then define a scalar field $\Sigma_g(\vec{x}) : D \subset \mathbb{R}^3 \to \mathbb{R}$ for every group constant Σ_g. The latter assigns a value to the multi-group constant Σ_g at each point $\vec{x}$ in the physical domain $D \subset \mathbb{R}^3$. In the remainder of the text, the subscript g will be removed for the sake of easier notation.

Let now $\Sigma(\vec{x}) : D \subset \mathbb{R}^3 \to \mathbb{R}$ denote a macroscopic cross-section scalar field. Then, the following equation can be used to express the functional relation between $\Sigma(\vec{x})$ and the

thermal-hydraulic conditions:

$$\Sigma(\vec{x}) = \mathcal{O}_n\{T(\vec{x}), \rho(\vec{x})\}. \tag{3.1}$$

In Eq. 3.1, $\mathcal{O}_n$ is an unknown non-linear operator mapping the effect of temperature $T(\vec{x})$ and density $\rho(\vec{x})$, on the macroscopic cross-section scalar field. The problem consists in efficiently approximating the action of this unknown operator $\mathcal{O}_n$ on the inputs $\rho(\vec{x})$ and $T(\vec{x})$. Notice that since the scalar field is constant in each node, Eq. 3.1 can be rewritten as:

$$\vec{\Sigma} = \mathcal{O}_n\{\vec{T}, \vec{\rho}\}, \tag{3.2}$$

where the ith component of the vectors $\vec{T}$, $\vec{\rho}$ and $\vec{\Sigma}$ denote the value of the temperature, density and field in the ith node. In the remainder of the section, we will use the vector notation for consistency with Chapter 1-2.

3.2 Solving the problem: Generalized Transfer Functions

The GTF is a spectral method that allows to describe the dependence of the cross-sections on the TH fields in terms of elementary spatial profiles rather than local values of temperature and density. In this section, the GTF method is motivated and derived from a general Petrov-Galerkin framework [44].

3.2.1 Motivations

The traditional approach to solve the problem of approximating the function F in Eq. 3.1 is the branch-off calculation sequence in which the operational space is sampled by using the local value of the TH fields, *i.e.*, temperature and density. In practice, local values of fuel temperature and coolant density at the node are independently perturbed for every node. The latter is usually coincident with an axial sector of a single fuel assembly

and is completely reflected, *i.e.*, reflective boundary conditions are applied. The resulting value of the cross-sections are then tabulated as a function of fuel temperature and density. A physics-based interpolation technique based on the local values of the TH fields is then applied to the pre-generated tables to obtain operational-specific macroscopic cross-sections. There are two main issues with this approach. The first is that it neglects the effect of non-local TH perturbations on the cross-sections. These effects can play a crucial role in shaping the power distribution in systems with large neutron mean-free-path such as graphite-moderated and fast reactors, or the upper regions in BWR reactors where the water density is lower. To account for these non-local effects, the cross-sections can be generated by employing super-cells, *i.e.*, sets of assemblies, rather than single assemblies. However, the effect of perturbing the TH fields in the neighboring assemblies on the local cross-section is not modeled, therefore leading to less accurate estimation. The second issue related to the use of the traditional approach is that the method is only memory-efficient for coarse mesh generation of cross-sections. If the cross-sections need to be generated and reconstructed for fine nodes, such as the one employed in finite elements-based radiation transport codes, *e.g.*, RATTLESNAKE [45], the method would require a number of cross-section evaluations proportional to the number of spatial degrees of freedom. The latter can be in the order of hundreds of thousands or even millions, therefore leading to a memory-inefficient algorithm.

The generalized transfer function method is a spectral method that leverages complete sets of basis functions to expand the input, *i.e.*, $\vec{\rho}$ and $\vec{T}$, and the output variables, *i.e.*, $\vec{\Sigma}$. The GTF is a functional remapping the response of the system to the input variables onto the output variable space. An example of complete basis set is reported in Figure 3.1 for a function θ defined on a finite 2D spatial domain. The use of spatial expansion functions in lieu of the local value of the TH fields allows to capture inter-nodal effects that are usually ignored in the traditional computational sequence. The method has three main advantages over the traditional approach to cross-section generation and reconstruction:

1. The GTF captures non-local effects that are usually ignored in the traditional computation sequence, therefore leading to increased accuracy of the computed cross-sections.

2. The method allows to employ non-orthogonal basis functions to expand the spatial distribution of the variables of interest. The utilization of an optimized set of functions, for instance based off Singular Value Decomposition (SVD), may be used to abate the storage requirement [46]. In other words, a limited number of elementary shapes could be used in lieu of the many nodal values.

3. The basis functions/vectors are not bound to be defined on Cartesian geometry. In fact, the GTF is geometrically agnostic and it can be used to remap the TH fields on the cross-sections for general, non-regular geometries, such as the fuel pin proposed by LightBridge [2].

3.2.2 Petrov-Galerkin framework for single variable

The derivation will be here carried out for a single variable, namely the coolant density $\vec{\rho}$. The extension to many variables will be addressed in Section 3.2.5. Moreover, for the sake of simplicity, the theory will be developed assuming that a deterministic code is used for generating the cross sections. If a Monte Carlo method is utilized to compute the nodal cross-section, the expected value of the variable of interest must be utilized in lieu of the deterministic variable. Considerations on the effect of Gaussian noise will be provided in the Section 3.4.

Let us consider the simplified form of Eq. 3.1:

$$\vec{\Sigma} = \mathcal{O}_n\{\vec{\rho}\}. \tag{3.3}$$

Then, let us assume that $\rho(\vec{x})$ admits a unique set of coefficients $\{\rho^{(n)}\}_{n=0,\ldots,N}$ such

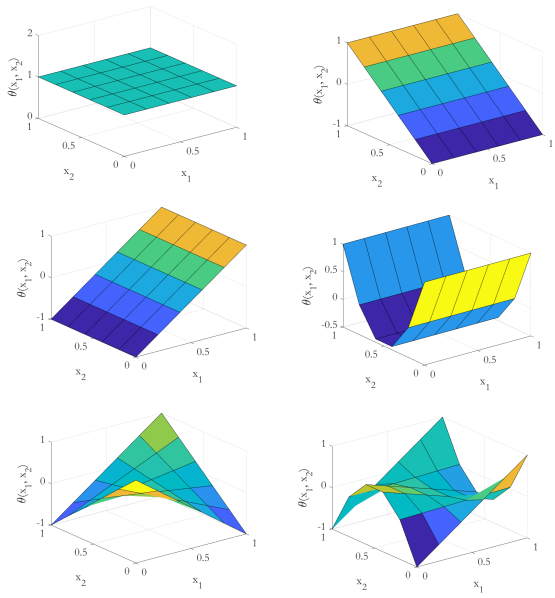

Figure 3.1: Example of complete basis for a function $\theta : \mathbb{R}^2 \rightarrow \mathbb{R}$.

that:

$$\vec{\rho} = \sum_{n=0}^{N} \rho^{(n)} \, \vec{\psi}_n. \tag{3.4}$$

In Eq. 3.4, $\{\vec{\psi}_n\}_{n=0,\ldots,N}$ is a complete bi-orthogonal basis functions set, meaning that:

$$(\vec{\psi}_n^{\dagger}, \vec{\psi}_l) = c_l \, \delta_{nl}. \tag{3.5}$$

In Eq. 3.5, $(\cdot, \cdot)$ denotes the inner-product defined on a Hilbert space $\mathbb{H}$, $\vec{\psi}^{\dagger}$ is the dual function basis, c_l is a positive real number, and δ_{nl} is the Kronecker delta. The exploitation of the bi-orthogonality property allows to efficiently compute the expansion coefficients as $\rho^{(n)} = \langle \vec{\psi}_n^{\dagger} | \vec{\rho} \rangle / c_n$. By inserting Eq. 3.4 into Eq. 3.3, we obtain the following identity:

$$\vec{\Sigma} = \mathcal{O}_n \left\{ \sum_{n=0}^{N} \rho^{(n)} \vec{\psi}_n \right\}. \tag{3.6}$$

If there exists a linear operator $\mathcal{O}_l$ that locally approximates the non-linear mapping

$\mathcal{O}_n$, Eq. 3.6 can be recast as:

$$\vec{\Sigma} \approx \sum_{n=0}^{N} \rho^{(n)} \mathcal{O}_l \left\{ \vec{\psi}_n \right\}. \tag{3.7}$$

The function $\mathcal{O}_l \left\{ \vec{\psi}_n \right\}$ is the system's linear response to a density profile of spatial shape $\vec{\psi}_n$.

Let us now consider a second set of complete bi-orthogonal basis functions $\{\vec{\Gamma}_l\}_{l=0,..,L}$, in general different from $\{\vec{\psi}_l\}_{l=0,..,L}$. Additionally, we assume $\{\vec{\Gamma}_l\}_{l=0,...,L}$ to be normalized such that $(\vec{\Gamma}_n, \vec{\Gamma}_l) = \delta_{nl}$. Expanding the macroscopic cross-sections into this basis, we obtain the equation:

$$\vec{\Sigma} = \sum_{l=0}^{L} \sigma^{(l)} \vec{\Gamma}_l. \tag{3.8}$$

The substitution of Eq. 3.8 into Eq. 3.7, the Galerkin projection onto the dual space $\{\vec{\Gamma}_l^{\dagger}\}_{l=0,..,L}$, and the exploitation of the bi-orthogonality property leads to the following equivalent representation:

$$\sigma^{(l)} \approx \sum_{n=0}^{N} \rho^{(n)} \left(\vec{\Gamma}_l^{\dagger}, \mathcal{O}_l \{ \vec{\psi}_n \} \right). \tag{3.9}$$

In Eq. 3.9, the factor $\left(\vec{\Gamma}_l^{\dagger}, \mathcal{O}_l (\vec{\psi}_n \right)$ is the projection of the system's linear response on the basis functions $\{\vec{\Gamma}_l\}_{l=0,..,L}$. Denoting the projected response with $R_{n \to l}$, and substituting the $\approx$ sign with the equality for the sake of easy notation, Eq. 3.9 can be rewritten as:

$$\sigma^{(l)} = \sum_{n=0}^{N} \rho^{(n)} R_{n \to l}. \tag{3.10}$$

In Eq. 3.10, the term $R_{n \to l}$ can be interpreted as the response to a perturbation of the coefficient $\rho^{(n)}$ projected onto the lth basis function. Eq. 3.10 can be rewritten in an equivalent

form:

$$\sigma^{(l)} = H^{(l)}\,\rho^{(l)}, \tag{3.11}$$

where $H^{(l)}$ is the generalized transfer function:

$$H^{(l)} = \frac{\sigma^{(l)}}{\rho^{(l)}} = \frac{\sum_{n=0}^{N} \rho^{(n)} R_{n\to l}}{\rho^{(l)}}. \tag{3.12}$$

Eq. 3.12 shows that the transfer function is a weighted average of the individual responses that correspond to uniquely defined shapes. The weights coincide with the ratio $\vec{\rho}^{(n)}/\vec{\rho}^{(l)}$. It must be noticed that, in Eq. 3.12, the density is expanded in the basis $\{\vec{\psi}_n\}_{n=0,\ldots,N}$ at the numerator, while at the denominator is expanded using the basis $\left\{\vec{\Gamma}_l^{\dagger}\right\}_{l=0,\ldots,L}$.

3.2.3 On the choice of the basis functions

The derivation presented in Sec. 3.2 is not bound to a choice of the basis sets $\{\vec{\psi}_n\}_{n=0,\ldots,N}$ and $\left\{\vec{\Gamma}_l\right\}_{l=0,\ldots,L}$. The only constraints are the following:

- The basis vectors $\{\vec{\psi}_n\}_{n=0,\ldots,N}$ must be linearly independent.
- The basis vector $\left\{\vec{\Gamma}_l\right\}_{l=0,\ldots,L}$ must be bi-orthogonal or orthogonal.

The two constraints above have interesting consequences. The first is that the TH variables are not bound to be expanded in terms of orthogonal or bi-orthogonal basis sets. Therefore, actual density spatial distribution can be utilized for the purpose of forming a basis set. The second is that, in general, the two basis sets are different and can be optimized for the TH variables and the cross-sections separately.

For the TH basis functions, a natural choice is the Krylov basis, *i.e.* distribution of the TH variable of interest obtained at each Picard iteration. This allows to eliminate the problem of choosing a basis set relying on theoretical or semi-analytical insights. Another

basis set that could be used for the purpose of expanding the TH field is a basis set obtained from Singular Value Decomposition (SVD) on snapshots of systems. However, this choice requires a problem-dependent training stage for the algorithm that is incompatible with the attempt to predict the cross-sections on-the-fly.

Concerning the bi-orthogonal basis set $\{\vec{\Gamma}_l\}_{l=0,1,\ldots}$, many choices are possible. In this work, we used the discrete Fourier basis. The choice derives from two considerations. First, the computation of the expansion coefficients is extremely efficient using standard Fast Fourier Transform (FFT) algorithms [47]. Secondly, the introduction of the Fourier transform enables to leverage common signal processing techniques for denoising cross-sections generated with MC codes.

3.2.4 Single shape approximation of the GTF

A simplified expression for the transfer function $H^{(l)}$ can be obtained when $\forall n > 0$, $\rho^{(0)} >> \rho^{(n)}$ and the expansion coefficient are normalized such that $\rho^{(0)} = 1$. In this case, Eq. 3.12 can be approximated as:

$$H^{(l)} \approx \frac{R_{0\to l}}{\rho^{(l)}}. \tag{3.13}$$

In Eq. 3.13, $R_{0\to l}$ is the projection of the response $L(\vec{\psi}_0)$ onto the lth basis function. Being the response of interest the macroscopic cross-section $\vec{\Sigma}$, $R_{0\to l}$ is then the $l^{(th)}$ Fourier expansion coefficient of the cross-section $\vec{\Sigma}$ due to a density profile of shape $\vec{\psi}_0$. Denoting this expansion coefficient as $\vec{\Sigma}^{(l)}$, Eq. 3.13 can be rewritten as:

$$H^{(l)} \approx \frac{\Sigma^{(l)}}{\rho^{(l)}}. \tag{3.14}$$

If we use the Fourier discrete basis for expanding the cross-sections, Eq. 3.14 can be

written in the following form:

$$\tilde{H} \approx \frac{\tilde{\Sigma}}{\tilde{\rho}}, \tag{3.15}$$

where the tilde denotes the discrete Fourier transform of the underlying function. *e.g.*, $\tilde{\Sigma} \equiv \mathcal{F}\{\vec{\Sigma}\}$ is the discrete Fourier transform of $\vec{\Sigma}$. From Eq. 3.15, it is evident that the transfer function is formally identical to the one commonly defined for Linear Time Independent (LTI) systems [47]. In addition, the cross-section can be computed by using the discrete Fourier inverse-transform $\mathcal{F}^{-1}$:

$$\vec{\Sigma} = \mathcal{F}^{-1}\{\tilde{H}\ \tilde{\rho}\}. \tag{3.16}$$

This simplified definition of GTF can be leveraged if either the transfer function is a slow varying function of the density or the density changes are modest. In this case, $\tilde{H}$ can be calculated once and utilized to predict the cross-sections distribution for many density profiles.

3.2.5 Extension of the single-shape approximation to multiple feedback mechanisms

Two main strategies can be utilized to extend the GTF theory to multiple variables, *e.g.* fuel temperature, coolant density, moderator temperature.

1. The first approach considers the variables as uncorrelated. The transfer function can then be characterized by sampling the variables' profiles independently and recording the response of the system. In practice, this means to create an N dimensional table, where N is the number of TH variables of interest. Let us consider, for the sake of illustration, the case of two variables, *e.g.*, the fuel temperature $\vec{T}_f$ and moderator density $\vec{\rho}$. Both the fuel temperature and density profiles are expanded in a numerable set of elementary shapes $\vec{\psi}_i$. The row i and column j of the table will then contain the transfer function computed for the fuel temperature spatial profile $\psi_i(\vec{x})$ and density

$\vec{\psi}_j$. The reconstruction of the transfer function for a different spatial profile can be obtained through projection.

$$H = \sum_{i=0}^{I_T} \sum_{j=0}^{N_\rho} \alpha_{i,j} H_{i,j}, \tag{3.17}$$

where $\alpha_{i,j}$ is defined as the product:

$$\alpha_{i,j} = \langle \vec{\psi}_i^\dagger | \vec{\rho} \rangle \, \langle \vec{\psi}_j^\dagger | \vec{T}_f \rangle / c_{ij}, \tag{3.18}$$

where c_{ij} is a normalization coefficient.

This approach is simple to implement and similar in philosophy to the branching sequence, routinely employed for cross-sections generation, within which the temperature and density value is perturbed at each node independently. It must be noticed that this method requires to execute a transport solution for each shape function $\vec{\psi}_j$, and each variable leading to relatively high computational and memory requirements.

2. The second approach uses correlated temperature and density spatial profiles, instead of considering the contributions due to density and temperature as independent. In other words, consistent temperature and density profiles are obtained from a TH-subchannel code's run and a one-to-one relation is assumed to hold. In general, this is true if the coolant is in single phase, while it does not hold for two-phase flows where an additional degree of freedom is present due to the void fraction, α.

3. The third strategy consists in defining an effective variable $\vec{\xi}$ that captures the effect of multiple TH fields. This approach allows to maintain the simplicity of the algorithm employed for the single TH feedback. In order to define the variable $\vec{\xi}$, we can leverage insights concerning the way macroscopic cross-sections depend on TH fields. In particular, for Light Water Reactors (LWR), we can employ the new

variable:

$$\vec{X} = \sqrt{\vec{T}_f} \circ \vec{\rho} \tag{3.19}$$

where the symbol $\circ$ denotes the Hadamard product, *i.e.*, element-wise operation, while $\vec{T}_f$ and $\vec{\rho}$ are the fuel temperature and density distribution. In the variable $\vec{\xi}$, the square root of the fuel temperature accounts for the dependence on the Doppler temperature feedback. It must be observed that the choice of the variable is grounded on semi-heuristic considerations and it depends on the physics of the system. For non-LWR reactors alternative definitions of the variable $\vec{\xi}$ may be needed to capture the phenomena arising from the use of different materials in the reactor core.

In this thesis, the second and third strategy are investigated to obtain an on-the-fly evaluations of the transfer functions. This is because they allows to use the same machinery utilized for the single feedback while obtaining a good estimation of the cross-sections' variation. Additionally, both strategies need only a single evaluation of the cross-sections, making these methods computationally more efficient than the first strategy.

3.2.6 Implementation for three-dimensional spatial distributions

Despite being formulated for general three dimensional spatial distributions, the practical implementation of the GTF can be challenging when the Fourier basis is utilized for general geometries, *i.e.*, non-Cartesian. This is because the DFT is defined for uniform sampling on periodic signals, therefore not being an optimal choice for general heterogenous geometries. To circumvent this shortcoming, different strategies can be envisioned to apply the GTF to general three-dimensional distributions $\vec{v}_{i,j,k}$, where i, j, and k are directional indexes.

- The first strategy relies on directly applying the three-dimensional DFT to the spatial distribution. This strategy enables a straightforward theoretical formulation for the

method. In fact, no modifications need to be carried out on the theory for the GTF methodology. However, the inability of the three-dimensional DFT to natively handle non-Cartesian mesh, makes the implementation changeling for non-square lattices, *e.g.*, hexagonal lattices. In the latter case, more complex methodologies need to be utilized such as the one reported in Ref. [48], therefore complicating the GTF implementation. This is in contradiction with the underlying philosophy of the methods that needs to be practical, and, therefore, of relatively easy implementation.

- The second strategy relies on using a collection of transfer functions generated for each channel or sub-channel separately. This approach is the simplest possible and allows to exploit the machinery developed for the mono-dimensional methodology. Despite its simplicity and the consistency with the theory developed in this chapter, the inability to account for inter-channel effects does limit the applicability of this method for accurately predicting the 3D cross-sections distributions.

- The third strategy consists in vectorizing the 3D distribution. This implies defining a new compound index such that $\vec{v}_{i,j,k} \rightarrow \vec{v}_{l(i,j,k)}$ where $l(i,j,k)$ is a compound index. The only constraint for the compound index function $l(i,j,k)$ is to be bijective with respect to the input indexes, *i.e.*, there is a unique assignment. The general nature of the function $l(i,j,k)$ makes this approach an available option for both structured and unstructured mesh. However this strategy does not take into consideration the actual topology of the problem, therefore having a lower fidelity than the one employing a 3D Fourier transform. For a Cartesian mesh, we can take advantage of the mesh elements' ordering along each of the orthogonal directions x, y, and z to define two vectorization approaches:

  - The first vectorization approach, here denominated plane-by-plane vectorization, swipes the geometry horizontally before moving vertically. In practice, the origin is defined in the bottom left corner of the geometry and the coor-

dinate axes are swept sequentially. In this case, the function describing the compound index is:

$$l(i,j,k) = i + N_x * (j-1) + N_x * N_y * (k-1), \tag{3.20}$$

where N_x, and N_y are the total number of mesh elements along the x, and y axis.

– The second vectorization approach, here denominated channel-by-channel vectorization, swipes the geometry vertically before moving horizontally. In other words, it exhausts all the elements in one channel before moving to the adjacent one. The ordering of the channels can be made such that the x and y directions are swept sequentially. In this case, the compound index is described as:

$$l(i,j,k) = k + N_z * (i-1) + N_z * N_x * (j-1), \tag{3.21}$$

where N_z is the number of mesh elements.

In this thesis, the last approach will be utilized. This is because it can be used for general three-dimensional distributions, without compromising the simplicity of implementation or the computational efficiency of the GTF-based acceleration.

3.3 Preliminary Results on Single Shape Approximation

To preliminarily test the performance of the proposed approach, we use an axially-reflected 3D BWR unit-cell, *i.e.*, pin radially surrounded by water, for both fresh and depleted fuel. The fuel lattice pitch is 1.87 cm and radial reflective boundary conditions are imposed. The length of the unit cell is 366 cm and 20 cm of water reflector surrounds the active core at the top and bottom. The 3% fresh fuel was burned for 3.0 MWd/kgU to obtain the depleted case. The axial burnup distribution is reported in Fig. 3.2. The unit-cell was discretized

in 36 equally-high axial layers for the purpose of tallying the cross-sections' nodal values. The TH feedback was limited to the void fraction and only mono-energetic group constants are considered. The problem was chosen to show the main strengths and the limits of the method with the minimum computational effort.

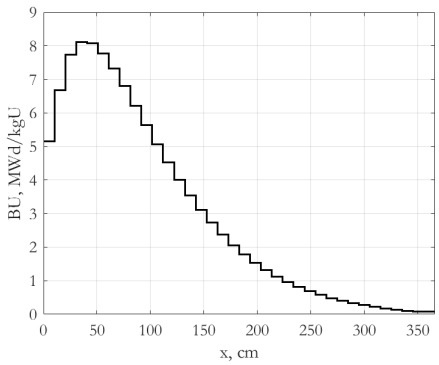

Figure 3.2: Burnup Axial Distribution.

In both cases, the reference results were generated using 300,000 particle per 400 criticality cycles of which 100 inactive, leading to maximum standard deviation below 0.1% for all the quantities of interest. The sequence to compute the transfer function was implemented in a MATLAB 2018b linkage code, while Serpent 2.1.30 was used to compute the cross-sections spatial distribution and the associated uncertainty [27].

For the fresh fuel, we considered the three density profiles shown in Fig. 3.3. These three profiles $\{\vec{\rho}_i\}_{i=1,2,3}$ were chosen arbitrarily. The density ρ_3 was used to compute the transfer function for the absorption macroscopic cross-section. This TF is then convoluted with $\{\vec{\rho}_i\}_{i=1,2,3}$ and the associated absorption cross-sections predicted. The absorption was chosen over other cross-sections' types since it gives the worst results in terms of accuracy. This is consistent with the intention of obtaining a lower bound for the method's accuracy.

The results are reported in Fig. 3.3.b. The solid lines represent the reference Monte Carlo cross-sections, while the star markers are associated to the solutions found with the FFT-based prediction. The plot shows agreement within 1% between the reference and the predicted cross-sections. This agreement is also preserved at the boundaries where the

spatial gradient is maximum. It is worth noticing that the worst results are obtained for $\vec{\rho}_1$. This is because it is the curve with maximum average distance $|\delta\vec{\rho}|$ from the reference point $\vec{\rho}_0$. This is consistent with the theoretical observations in Section 3.2.4.

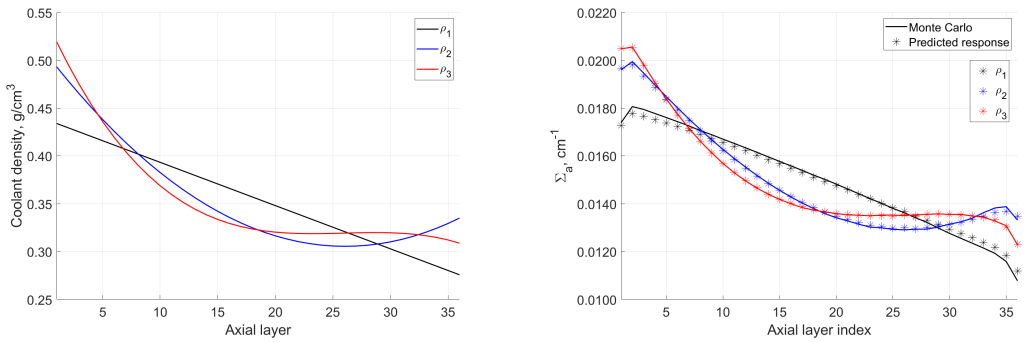

(a) (b)

Figure 3.3: (a) Three arbitrary density profiles. (b) Corresponding predicted and reference absorption cross-sections distributions.

Contrary to the process adopted for the fresh fuel, the five density profiles $\{\vec{\rho}_j\}_{j=1,..,5}$ reported in Fig. 3.4 were extracted from a fixed point MC-TH calculation for the BWR unit-cell with depleted fuel. A density variation from $\vec{\rho}_1$ to $\vec{\rho}_5$ leads to an average power change of 30%, with nodal peaks of 50%. For each of these profiles, a transfer function H_j was then generated by using Eq. 3.15. In the remainder of the Section, $H_j^{\Sigma_a}$ and $H_j^{\nu\Sigma_f}$ will denote the transfer functions mapping the profile $\vec{\rho}_j$ over the one-group macroscopic absorption cross-section and macroscopic fission neutrons production, respectively.

For Eq. 3.16, the prediction of the cross-sections $\vec{\Sigma}_X$ is obtained by inverse-transforming the product between the transfer function and the density profile. In this work, to perform the Fourier transform and inverse-transform the functions `fft` and `ifft` implemented in MATLAB are utilized. In order to verify the weak relationship between H and $\vec{\rho}$, all the possible combinations of transfer functions $H_k^{\Sigma_X}$ and density profiles $\vec{\rho}_j$ are calculated. Figs. 3.5-3.6 show the predictions of the absorption macroscopic cross-sections $\vec{\Sigma}_a$ and the macroscopic fission-production term $\nu\vec{\Sigma}_f$ using $H_1^{\Sigma_a}$ and $H_1^{\Sigma_f}$. It is noticeable that good agreement is found in all cases, although the accuracy decreases with increasing distance

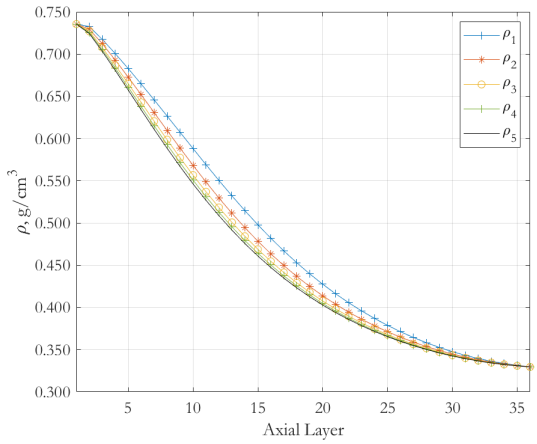

Figure 3.4: Density Axial Distributions $\{\vec{\rho}_j\}_{j=1,\ldots,5}$.

between initial guess and actual profile. The Mean Absolute Percentage Error (MAPE) for $\vec{\Sigma}_a$ passes from 0.76% to 1.39% going from $\vec{\rho}_2$ to $\vec{\rho}_5$, while it passes from 0.386% to 0.658% for $\nu\vec{\Sigma}_f$. The MAPE of $\vec{\Sigma}_a$ for all the simulated cases is reported in Table 3.1.It can be noticed that the MAPE, although always lower than 2%, increases with the distance between $\vec{\rho}_1$ and $\vec{\rho}_j$, as expected based on the theoretical description in Section 3.2. The macroscopic fission neutrons production follows the same pattern, with MAPE bound by 1%.

Table 3.1: MAPE of Σ_a for different combinations of density profile and transfer functions.

TF/Density	$\vec{\rho}_1$	$\vec{\rho}_2$	$\vec{\rho}_3$	$\vec{\rho}_4$	$\vec{\rho}_5$
$H_1^{\Sigma_a}$	0.00	0.76	1.18	1.66	1.37
$H_2^{\Sigma_a}$	0.76	0.00	0.43	0.91	0.61
$H_3^{\Sigma_a}$	1.20	0.43	0.00	0.49	0.19
$H_4^{\Sigma_a}$	1.69	0.92	0.49	0.00	0.30
$H_5^{\Sigma_a}$	1.39	0.62	0.19	0.30	0.00

The accuracy of the cross-sections' prediction is caused by the low sensitivity of the transfer functions to the density variation. This can be seen from Fig. 5.4, where the Bode diagram of the transfer functions generated at $\vec{\rho}_1$ and $\vec{\rho}_5$ for $\vec{\Sigma}_a$ are reported. It is noticeable that all the expansion coefficients are not null. There are two causes for this phenomenon. First, the cross-sections present steep local gradients at the domain's boundaries due to

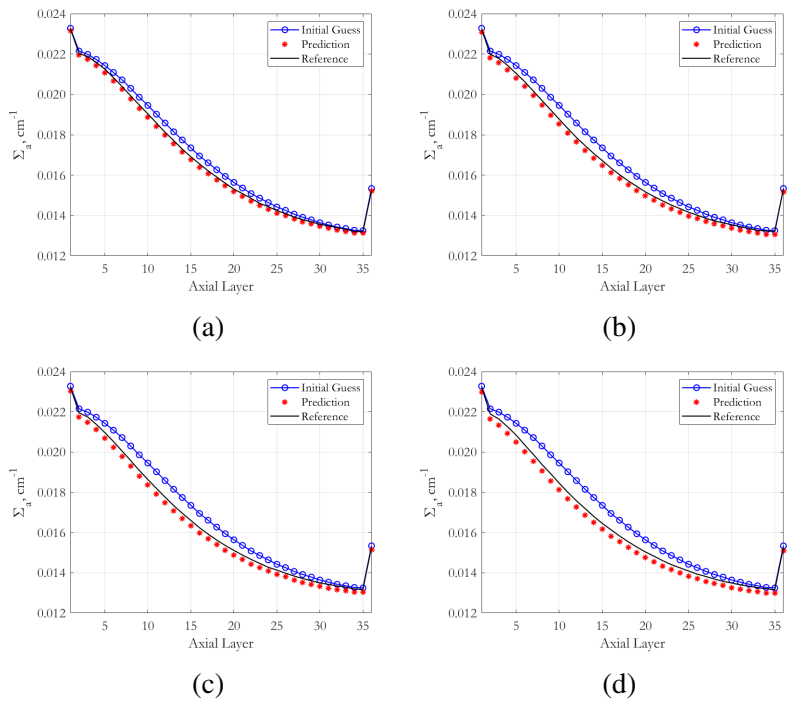

Figure 3.5: Predictions of the macroscopic absorption cross-sections' spatial distribution (star markers) compared with the MC-generated reference solution (dashed lines) and the initial guess for: (a) $\vec{\rho}_2$, (b) $\vec{\rho}_3$, (c) $\vec{\rho}_4$, (d) $\vec{\rho}_5$. Transfer function calculated at $\vec{\rho}_1$.

the presence of reflectors. Second, the DFT is applied to a non-periodic signal in a finite space-domain, giving origin to spectral leakage, *i.e.*, higher modes are exited because the periodic extension of the signal outside the observation window is not continuous. Both these phenomena excite high order coefficients. This may constitute a problem if the FFT with hard threshold is utilized to denoise the MC output.

3.4 Considerations on noise

An interesting consideration regarding the effect of noise on the cross-sections' prediction can be drawn from Fig. 3.8.a . The latter represents the transfer function $H_1^{\Sigma_a}$ generated with poor statistics: 1,000 particles/cycle for 100 cycles (50 active). It is evident that the noise undermines the quality of the TFs' estimation. This stochastic fluctuation propagates through the calculations leading to results with undermined accuracy as shown in Fig. 3.8.b, where the prediction performed with high statistics and low statistics are compared.

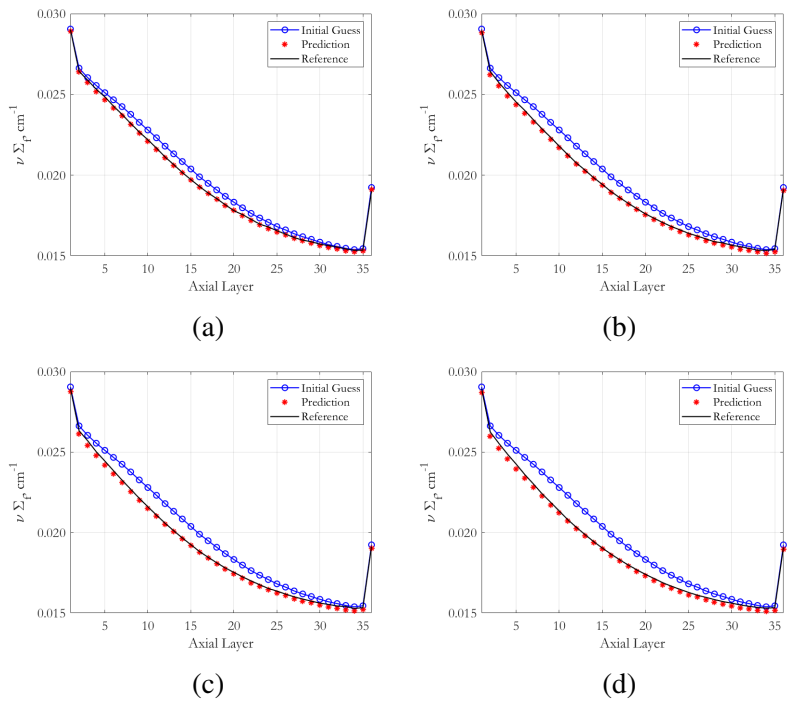

Figure 3.6: Predictions of the macroscopic fission neutron production's spatial distribution (star markers) compared with the MC-generated reference solution (dashed lines) and the initial guess (solid line) for: (a) $\vec{\rho}_2$, (b) $\vec{\rho}_3$, (c) $\vec{\rho}_4$, (d) $\vec{\rho}_5$. Transfer function for $\vec{\rho}_1$.

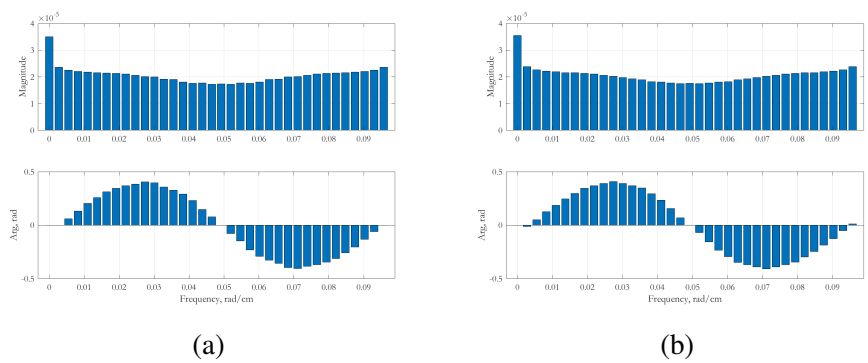

Figure 3.7: Transfer Functions for Σ_a calculated for: (a) $\vec{\rho}_1$ and (b) $\vec{\rho}_5$

3.5 Summary

In this chapter the theory of the Generalized Transfer Function (GTF) method was introduced from a general Petrov-Galerkin framework valid for a single TH variable, *e.g.*, moderator density. In particular, the single shape approximation of the GTF was derived and its limitations were discussed. The theory was then extended to multiple TH input variables

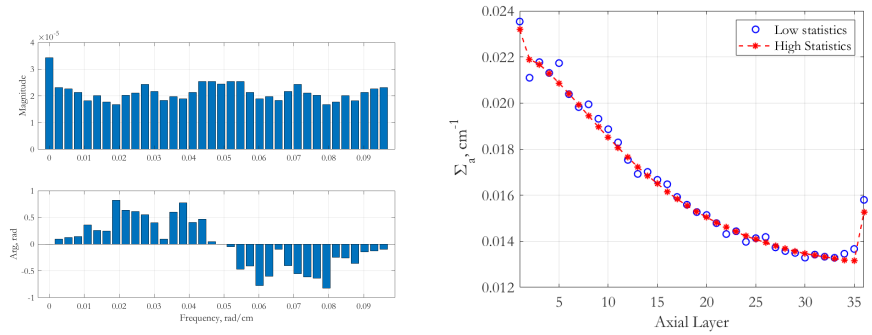

(a) (b)

Figure 3.8: (a) Transfer Functions calculated at $\vec{\rho}_5$ with reduced statistics and (b) Associated prediction.

and the implementation of the method for multi-dimensional distributions was addressed. Results obtained for an axially-reflected BWR unit-cell with realistic axial density profile and non-homogeneous axial fuel composition were used to support the theoretical claims. It was shown that the method is able to predict the one-group macroscopic cross-sections within a few percent even near the boundaries. According to our analysis, two caveats must be considered when utilizing this technique. First, the accuracy of the solution decreases with increasing distance between the initial guess and the actual distribution of the quantity of interest. Second, the statistics can undermine the quality of the results, by exciting higher components of the Fourier spectrum.

CHAPTER 4
GTF-BASED ACCELERATION

The purpose of this chapter is to introduce a physics-based prediction block to accelerate the MC-TH Picard iteration scheme. The prediction will leverage the GTF method introduced in Chapter 3.

The remainder of the chapter is structured as follows. Section 4.1 presents a literature review of the acceleration methods used for the Picard iteration scheme with an emphasis on MC-TH application. The GTF-based acceleration scheme is introduced in Section 4.2 and implementation details are provided in Section 4.3. Finally, the findings of this chapter are highlighted in Section 4.4.

4.1 Literature Review

Three main strategies have been devised to accelerate the Picard iteration in the context of the MC-TH fixed point problem. The first method, denominated Steffensen's acceleration method, defines a quadratic sequence from the Picard iterations' sequence. The latter is characterized by faster convergence rate to the fixed point when compared to the original Picard iterates. The second approach is called Anderson's acceleration and uses an optimized weighted sum of the iterates to define a new fixed point estimate. The final method, that we will call Herman's acceleration, uses a reduced order model to provide a better guess of the fixed point at the next iteration. In the following section, each of this approaches is described.

4.1.1 Steffensen's Acceleration

The Steffensen's acceleration method relies on the definition of Aitken's process, alternatively denominated Δ^2 process. The latter associates a superlinearly convergent sequence

to an original linearly convergent sequence, such as the one formed by the Picard iterates [49].

Let then $\{\xi_{n+1}\}_{n=0,1,\ldots,N}$ denote the set of the Picard iterates and let us assume that the sequence formed by the member of this set converges to the fixed point ξ^* with linear convergence rate. If there exists a real number $A : |A| < 1$ such that:

$$\lim_{n\to\infty} \frac{\xi^* - \xi_{n+1}}{\xi^* - \xi_n} = A, \tag{4.1}$$

then the sequence:

$$\dot{\xi}_n = \xi_n - \frac{(\xi_{n+1} - \xi_n)^2}{\xi_n - 2\xi_{n+1} + \xi_{n+2}}, \tag{4.2}$$

converges faster to the fixed point ξ^* compared to the original Picard sequence, in the sense that:

$$\lim_{n\to\infty} \frac{\xi^* - \dot{\xi}_n}{\xi^* - \xi_n} = 0 \tag{4.3}$$

Eq. 4.2, that is valid only for scalar fixed points, can be generalized for vectorial fixed point problems [50]:

$$\vec{\xi} = \vec{\xi}_n - \frac{||\vec{\xi}_{n+1} - \vec{\xi}_n||^2 \left(\vec{\xi}_n - 2\vec{\xi}_{n+1} + \vec{\xi}_{n+2}\right)}{||\vec{\xi}_n - 2\vec{\xi}_{n+1} + \vec{\xi}_{n+2}||^2} \tag{4.4}$$

In the context of neutronics MC calculations, Eq. 4.2 was used to predict the multiplication factor at the next criticality cycle, *i.e.*, neutronics in absence of TH feedback, while its vectorial form was utilized to accelerate coupled deterministic neutronics and TH calculations [51].

The Steffensen's acceleration scheme has several desirable characteristics. First, it is a memory-efficient algorithm, *i.e.*, only two Picard iterates need to be stored. Second, it has close-to-negligible computational overhead. Finally, it is of simple implementation and

inclusion in non-linear solution schemes. The main drawback of the scheme is that the difference between successive iterates must be ”small enough” for the Steffensen’s acceleration to work. This undermines the efficacy of this acceleration scheme at the beginning of the iterative calculations when the distance between successive iterates is ”larger”, unless a close-enough initial guess of the fixed point is used. Additionally, the presence of stochastic noise, corrupting the iterates, can farther undermine the method’s efficacy and the gain in convergence rate.

4.1.2 Anderson’s Acceleration

The Anderson’s acceleration utilizes a weighted sum of iterates to define the new element of the converging sequence $\{\vec{\dot{\xi}}_n\}_{n=0,\ldots,N}$:

$$\vec{\dot{\xi}}_n = \sum_{l=0}^{L} \beta_l \, \vec{\xi}_l, \tag{4.5}$$

where $\{\beta_l\}_{l=0,..,L}$ is a set of real valued coefficients that solve the constraint minimization problem:

$$\min_{\sum_{l=0}^{L} \beta_l = 1} ||\vec{\dot{\xi}}_n||. \tag{4.6}$$

In Eq. 4.6, $|| \cdot ||$ defines a suitable norm, *e.g.*, L2 norm. The method, without truncation is equivalent to the generalized minimal residual (GMRES) method [52]. However, no more than five iterates are retained to perform the acceleration calculations for practical applications. This method has been utilized to accelerate multiphysics calculations on neutronics-TH simplified problems leading to local improvement of the convergence rate [53].

4.1.3 Herman's acceleration

The acceleration scheme, proposed by Herman et al., leverages a neutronic reduced order model (ROM) to obtain a "better guess" of the power profile, *i.e.*, the fixed point, at the next iteration. The better guess translates in a faster convergence of the algorithm to the fixed point. The acceleration procedure, performed at every criticality iteration, is represented in Fig. 4.1. The power, obtained from the Monte Carlo code, is fed into the TH solver that outputs temperature and density fields. The latter are then utilized within the prediction block, represented by red blocks in Fig. 4.1.

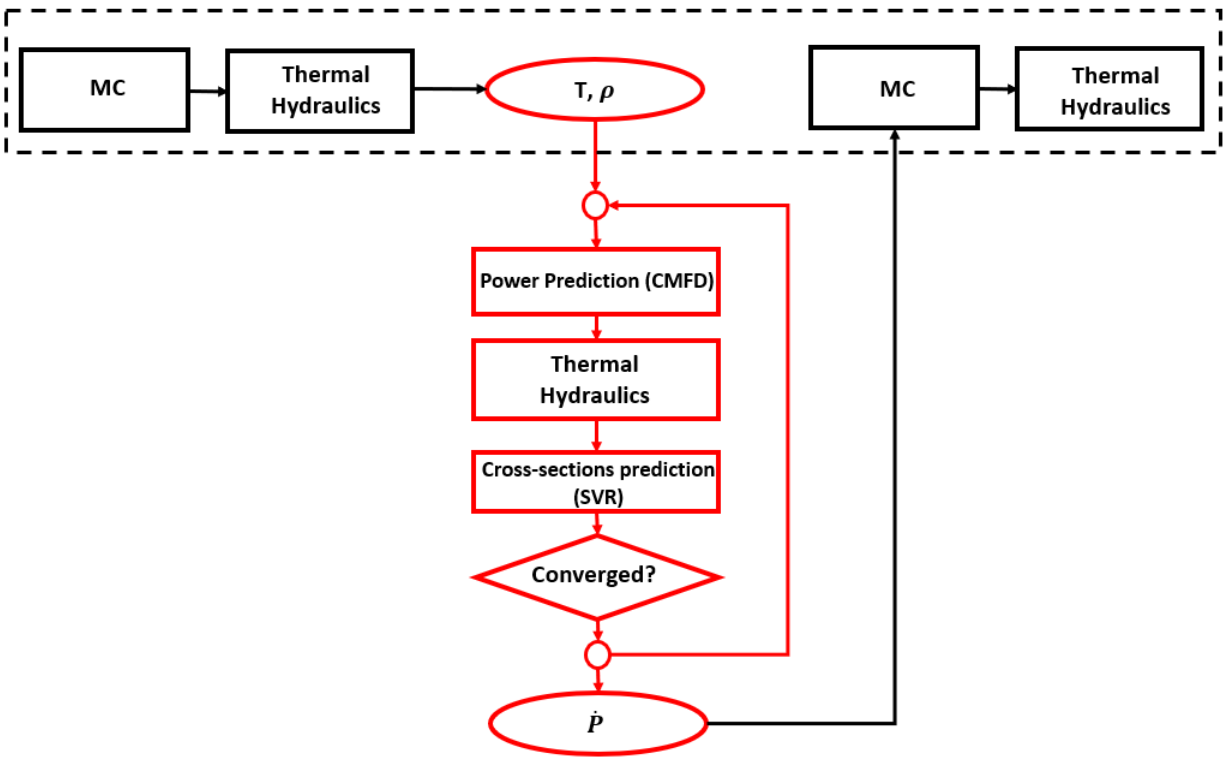

Figure 4.1: Prediction block for Herman's acceleration.

1. In the first sub-block the power distribution is calculated from the tallied cross-sections using a reduced order model for neutronics. Herman uses a Coarse Mesh Finite Difference (CMFD) solver, a well-known technique, originally developed to accelerate fission source convergence in nodal simulations [20], and then applied to

speed up the convergence of the fission source in Monte Carlo criticality calculations [21]. However, alternative solvers can be used in lieu of the CMFD, as noticed in Ref. [4].

2. A sub-channel TH code is then used to estimate the full-core temperature and density spatial distribution.

3. In the third sub-block, the macroscopic cross-sections corresponding to the updated temperature and density profiles are predicted using Support Vector Regression (SVR), a data-driven machine-learning technique able to capture 3D inter-nodal effects. The latter reframes the problem of evaluating the cross-sections response to temperature and density as an optimization problem. The macroscopic cross-section Σ_i is modeled as:

$$\Sigma_i = \langle \vec{w}_i \ , \ \vec{x} \rangle + b_i, \tag{4.7}$$

where b_i is an offset coefficient, $\vec{w}_i$ is a vector of weight, and the angle brackets denote the inner product. The unknown weights and offset can be found by solving the following minimization problem:

$$\begin{cases} \min \left\{ \frac{1}{2} + C \sum_{i=0}^{I} \left(\eta_i + \eta_i^* \right) \right\} \\ \Sigma_i - \langle \vec{w}_i \ , \ \vec{x} \rangle - b_i \leq \epsilon + \eta_i \\ \langle \vec{w}_i \ , \ \vec{x} \rangle + b_i - \Sigma_i \leq \epsilon + \eta_i^* \\ \eta_i, \eta_i^* \geq 0 \end{cases} \tag{4.8}$$

In Eq. 4.8:

(a) The variables η_i and η_i^* are slack variables and are included to improve the generalization and help with optimization.

(b) The variable ϵ and C are hyper-parameters to be set a priori or after a try-and-error procedure.

4. Finally, the updated cross-sections are fed into the CMFD solver to obtain the power distribution and the sequence is repeated until the difference between the power profiles calculated at successive iteration is below a set tolerance.

The method proposed by Herman has two interesting characteristics. First, it is relatively easy to implement and leverages well-known techniques. Second, Herman's acceleration is tailored to nuclear reactors' application, and, therefore, can be more efficient than other general-purpose techniques.

The main drawback of this approach is its reliance on the SVR. In fact, the latter, being a data-driven approach, needs problem-dependent training in order to accurately predict the cross-sections as a function of the 3D TH fields. For instance, in Ref. [18], to compute the coefficients in Eqs. 4.8, a full-core MC simulation was performed from which the cross-sections' tallies were collected. Each cross section-type model was then trained in separate SVR models from assembly averaged values resulting in a non-negligible computational overhead, therefore undermining the benefit of the acceleration scheme.

4.2 GTF-based acceleration

In this section, we propose a new prediction block that leverages the GTF to estimate the fixed point at the next iteration with low to negligible computational overhead. As Herman's acceleration described in Section 4.1.3, this GTF-based acceleration defines a ROM with lower computational weight than the original MC-TH sequence. However, the estimation of the cross-sections' variation due to the TH scalar fields' variation is performed using the GTF rather than the SVR. The main advantage of the GTF over the SVR is that does not require a problem-dependent training, therefore resulting in a net improvement in computational efficiency. The prediction block is composed of the following steps:

1. **Initial Conditions.** The density $\vec{\rho}_0$, temperature $\vec{T}_0$, the expected power distribution $\vec{Q}_0$, the node-wise absorption cross-sections $\vec{\Sigma}_a$ and secondary neutron production $\nu\vec{\Sigma}_f$ are obtained from the previous Picard iteration.

2. **GTF Calculation**. The transfer functions H_{Σ_Y} are then computed for the absorption and secondary neutrons production one-group cross-sections. In general, for the cross-section Σ_Y, the transfer function is:

$$H_{\Sigma_Y} = \frac{\tilde{\Sigma}_Y}{\tilde{\rho}}. \tag{4.9}$$

   In Eq. 4.9, $\tilde{\Sigma}_Y$ is the Discrete Fourier Transform (DFT) of the expected cross-section distribution Σ_Y of type Y, e.g. fission, while $\tilde{\rho}$ is the DFT of the corresponding density spatial distribution. If the effects of several variables needs to be captured, the density can be substituted by a proper variable as described in Section 3.2.5

3. **Convergence loop until residual $>$ tolerance**

   (a) **TH Solver.** The power $\vec{Q}_0$ is imposed as heat source in the TH equations. The latter are solved using the sub-channel code to obtain the density $\vec{\rho}'$ and temperature $\vec{T}'$ distributions.

   (b) **Inverse transform**. The updated group-constants $\tilde{\Sigma}$ are calculated from the transfer function (stage 3) and the new TH conditions.

$$\vec{\Sigma}'_Y = \mathcal{F}^{-1}\left(H_{\Sigma_X}\tilde{\rho}'\right). \tag{4.10}$$

   In Eq. 4.10, $\mathcal{F}^{-1}$ is the inverse Fourier transform.

   (c) **Power Solver**. The cross-sections are used in a fast reduced order neutronic solver to compute the updated power distribution $\vec{Q}'$. In this thesis, the First Order Perturbation (FOP) for the power update is used. The variation of the

effective multiplication factor $k = 1/\lambda$ is computed in the following way:

$$\delta\lambda = \frac{\left\langle \psi_0^\dagger, \delta\mathcal{L}\psi_0 - \lambda\delta\mathcal{M}\psi_0 \right\rangle}{\left\langle \psi_0^\dagger, \mathcal{M}\psi_0 \right\rangle}. \tag{4.11}$$

In Eq. 4.11:

- $\mathcal{L}$ is the loss operator as defined in Eq. 2.13, *i.e.*, scattering, collision and streaming term, *i.e.*, fission source.
- $\mathcal{M}$ is the fission operator *i.e.*, fission source, as defined in Eq. 2.12.
- ψ_0 and $\psi_0^\dagger$ are the dominant forward and adjoint flux eigenmode, respectively.

The variation of the dominant flux eigenmode can be predicted by superposition of effects:

$$\delta\psi_0 = \sum_{m=1}^{N} a_m \psi_m. \tag{4.12}$$

The expansion coefficients a_m can be computed in terms of the variation in loss and fission operator. Denoting with $\psi_m^\dagger$ the mth adjoint flux mode, and with λ_m the associated eigenvalue, the following definition for the expansion coefficient can be derived [54].

$$a_m = \frac{\left\langle \psi_m^\dagger, \delta\mathcal{L}\psi_0 - \lambda\delta\mathcal{M}\psi_0 \right\rangle - \delta\lambda \left\langle \psi_m^\dagger, \mathcal{M}\psi_0 \right\rangle}{\left\langle (\lambda - \lambda_m)\psi_m^\dagger, \mathcal{M}\psi_0 \right\rangle}. \tag{4.13}$$

In this work, the flux modes are assumed to coincide with the modes of the fission matrix produced by Serpent (see Appendix A for the definition of fission matrix). In addition, the simplification $\delta\mathcal{M} = \delta(\nu\Sigma_f)$ and $\delta\mathcal{L} = \delta\Sigma_a$ are introduced. The validity of these approximations is discussed in details in Ref. [55], while the demonstration of these equations are reported in Appendix B.

The full computational sequence for the GTF-accelerated Picard iteration is reported in Fig. 4.2. The acceleration can be performed every M criticality cycles, where $M \geq 1$.

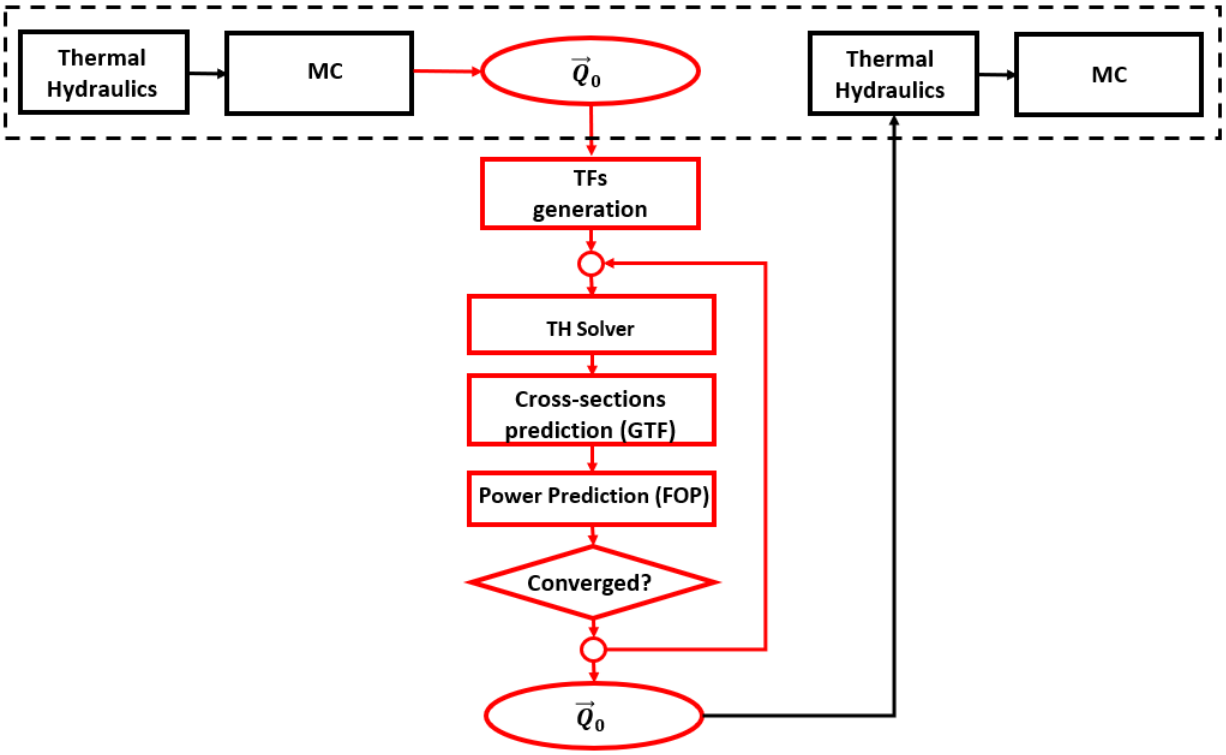

Figure 4.2: GTF-based prediction block.

4.3 Codes and Implementation Details

The implementation of the GTF-accelerated PI method is composed by three main blocks:

- A Monte Carlo code for particle transport.
- A sub-channel code for the resolution of the TH equations.
- A linkage code for input/output handling and to perform the power prediction.

4.3.1 Monte Carlo Code: Serpent

Serpent 2.1.31 is used as Monte Carlo solver. The latter is a three-dimensional, continuous-energy Monte Carlo neutron and photon transport code developed at VTT Technical Re-

search Centre of Finland, Ltd. [27]. The code relies on Woodcock delta-tracking for particle transport and unified energy grid for faster computations. In the framework of the GTF-based acceleration, Serpent to tally the expected nodal power distribution, together with the nodal macroscopic absorption cross-sections and the fission neutrons production at each Picard iteration. Additionally, the fission matrix is tallied to perform the power and multiplication factor's estimation according to Eqs. 4.11-4.13.

4.3.2 Sub-channel code: THERMO

Concerning the solution of the TH equations, THERMO, a thermal-hydraulic sub-channel code developed at the Ben-Gurion University of Negev, was utilized. The code is written in MATLAB and was meant for use with the neutron transport and depletion software BGCore before being developed as stand-alone package [56]. THERMO is under further development in my researh group, motivating its use within this dissertation. The code takes in inlet coolant properties and power distribution to calculates axial bulk temperature, density, and pressure profiles. The channels are axially discretized, and in each volume, the radial temperature distribution in the pin is found using thermal equivalent circuit models. The code can model and simulate both single phase and two-phase flows. In this paper, the Drift Flux Model is used to model the two-phase flow in the BWR unit-cell. THERMO was extensively verified in the past on many nuclear reactor designs, including PWRs [57], Resource-renewable Boiling Water Reactor (RBWR) [58], and hydrogen-cooled reactors for Nuclear Thermal Propulsion (NTPs) [59]. In this paper, THERMO is used to compute the moderator density profile $\vec{\rho}_m$, fuel temperature $\vec{T}_f$, and moderator temperature $\vec{T}_m$. The code takes the expected value of the power profile computed by Serpent and the inlet conditions for the coolant as input parameters.

4.3.3 Linkage Code

The linkage code was written in MATLAB. The latter externally couples Serpent and THERMO, allowing to perform coupled neutronics thermal-hydraulics in one and multiple dimensions. MATLAB was chosen over other programming languages for the purpose of fast code development. This was motivated by the author's extensive experience with this programming language and the ability of MATLAB to handle matrix and array operations with minimum code development effort.

Three are the functions of the linkage code:

- Transferring fuel, moderator temperature, and density profiles from THERMO to Serpent through modified input files. As regard to the thermal-scattering data, the library evaluated at the temperature closest to the one of interest is used. In addition, the initial guess for the effective multiplication factor and the spatial fission source profile are updated using the values at the previous Picard iteration, using the `pop` card and the `src` card respectively. The default initial guess for the energy and angular distribution of the fission source are utilized.

- Transferring the MC-tallied power spatial distribution from Serpent to THERMO through input file modification. The latter is used as heat source for the TH equations.

- Performing the prediction as explained in Section 4.2. The block collects the Σ_a and $\nu\Sigma_f$ spatial distribution tallied in Serpent, together with the TH fields generated at the previous iteration to generate the single-shape transfer functions. The latter are then used within the prediction block to estimate the power profile at the next iteration.

4.4 Summary

In this chapter, an overview of the acceleration methods for the Picard iterations was provided. The GTF-based acceleration was then introduced to address some of the limitations

of the previous methods when applied to MC-TH coupled calculations. Specifically, the GTF-based acceleration, contrary to Herman's method, does not rely on a problem-specific training, being a physics-based method rather than a data-driven approach. This allows to predict the cross-sections and the power at the next criticality cycle on-the-fly, therefore resulting in a net gain in computational efficiency. Additionally, a MATLAB code has been developed to perform 3D coupled MC-TH coupled calculations, employing Serpent and THERMO as single-physics code. The code can be easily modified and used for future research endeavors.

CHAPTER 5
MONO-DIMENSIONAL RESULTS

In this chapter, a proof of concept for the GTF-based acceleration based on a non-trivial one dimensional problem is provided. The latter is an axially-extruded BWR unit-cell, *i.e.*, UO_2 rod surrounded by water, with axial reflectors. The problem was chosen to gain insights into the limitations and strengths of the method with minimal computational expense. The proof-of-concept is carried out in three steps. First, in Sec. 5.1, the accuracy and speed-up of the GTF-based acceleration block is examined in a stand-alone fashion, *i.e.*, the predicted power profile, $\vec{P}$, is not fed back into Serpent and the TH solver. Moreover, the TH feedback is limited to the one associated to the moderator density, $\vec{\rho}$. In Section 5.2, the feedback is expanded to include both the fuel temperature, $\vec{T}_f$ and the moderator density. Finally, in Sec. 5.3, the GTF acceleration is integrated in the full Picard iterations sequence to measure the resulting acceleration and the accuracy of the integrated PI+GTF scheme when compared to the non-accelerated sequence. A summary of the results is provided in Section 5.4. In the remainder of the chapter, for the sake of easy notation, the vector sign will be dropped for the TH variables and the cross-sections distributions when deemed not essential or easily inferable from the context.

5.1 Single Variable, Stand-alone Prediction

This section analyzes the prediction block in a stand-alone fashion by considering ony the TH feedback associated to the moderator density. The remainder of the section is structured as follows. Section 5.1.1 describes the problem and illustrates the procedure used to calculate the reference solution. Comparison metrics to evaluate the efficacy of the prediction block are then introduced in Section 5.1.2. The GTF-based prediction is then utilized to predict the power profile from different reference power profiles in Sections 5.1.35.1.4.

Finally, observations on the effect of stochastic noise are presented in Section 5.1.5. The results are the same presented in Ref. [42].

5.1.1 Problem Description and Reference Solution

The geometry and material specifications for the axially-extruded BWR unit-cell problem, *i.e.*, pin surrounded by water, are reported in Fig. 5.1 and Table 5.1. The unit-cell height is 405.760 cm with 20 cm of axial reflector on both ends. Radial reflective and axial vacuum boundary conditions are imposed.

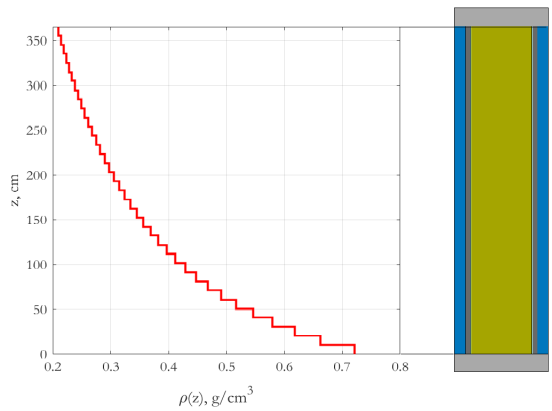

Figure 5.1: Axially-extruded BWR unit-cell's axial density profile and axial view. The 20-cm axial reflectors are at both ends of the 405.760-cm active fuel zone.

Table 5.1: BWR unit-cell problem specifications

Parameter	**Value**
Total Height, cm	405.760
Top Axial Reflectors' Height, cm	20
Bottom Axial Reflectors' Height, cm	20
Pellet radius, cm	0.60579
Gas-gap radius, cm	0.62103
Cladding radius, cm	0.71501
Pitch (cm)	1.87452
Gas-gap density, g/cm^3,	1.0004E-03
Zr cladding density, g/cm^3	6.5514
UO_2 density, g/cm^3	10.42

Nineteen TH-MC Picard iterations were executed to produce the reference solution. A total of 1,000,000 particles per 700 cycles, of which 150 inactive, were simulated at each MC-TH iteration. This led to a maximum relative standard deviation of 0.07% on the power tallies. The convergence tolerance was set to 0.001% for the density distribution. This reference solution accounts only for the TH feedback due to the changes in the density profile. Figure 5.2.a presents the value of the k_∞ as a function of the iteration number, while the reference power and density profile at selected Picard iterations are shown in Fig. 5.2.b-c to prove the convergence of the coupled sequence. The uncertainty was not propagated through the TH calculations, and, therefore, it is not shown in the plots. The Mean Average Percentage Error (MAPE) for the power and density as a function of the number of iterations is reported in Fig. 5.3, confirming the convergence of the coupled scheme. For the MAPE associated to the power profile, the fluctuations after five iterations are caused by the interplay between deterministic and statistical component of the error, *i.e.*, the MAPE and the average standard deviation for the power profile have the same order of magnitude.

5.1.2 Comparison Metrics

The prediction methodology is applied to evaluate the variation of the following Quantities of Interest (QoI): the macroscopic absorption cross-section $\vec{\Sigma}_a$, the macroscopic fission-production term $\nu\vec{\Sigma}_f$, the mass density $\vec{\rho}$, and the power profile $\vec{P}$. All the QoIs are node-wise constant and the cross-sections are in mono-energetic representation. The quality of the prediction is assessed through three metrics:

1. The first metric, the Percentage Absolute Difference (PADx), measures the bin-wise error for the QoI X:

$$PAD_i^X = \frac{|X_i - X_{r,i}|}{X_{r,i}} \times 100. \tag{5.1}$$

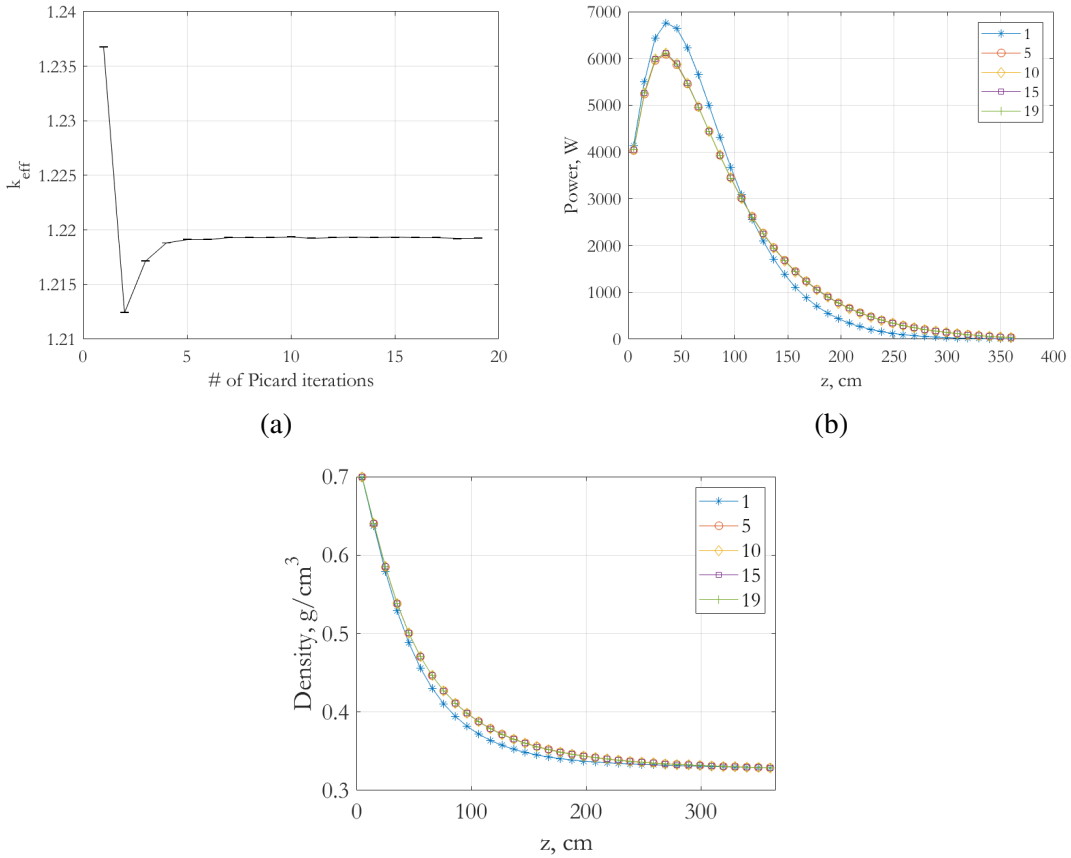

Figure 5.2: (a) k-inf as a function of MC-TH iteration's number, (b) Power distribution for selected iterations, and (c) Density profile for selected iterations.

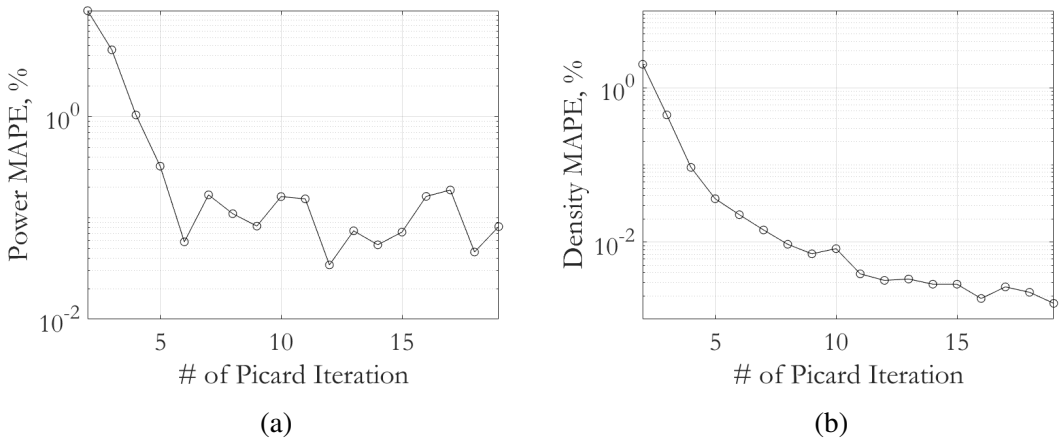

Figure 5.3: MAPE of power and density profile as a function of the Picard iterations' number.

In Eq. 5.1, X_i and $X_{r,i}$ are the value of the predicted QoI X, and the reference X_r at bin i, respectively.

2. The second metric, the Mean Absolute Percentage Error (MAPE), measures the average error on the QoI X. The MAPE for the QoI X is defined as:

$$MAPE_X = \frac{1}{N}\sum_{i=0}^{N} PAD_i^X \times 100, \tag{5.2}$$

where N is the total number of spatial bins.

3. The third metric is a Figure of Merit (FOM) introduced to assess the error's reduction between initial guess $\vec{X}_0$ and the outputs of the FFT-based prediction $\vec{X}$. Formally, it is described by the following ratio:

$$FOM_X = \frac{MAPE_X}{MAPE_{X_0}}. \tag{5.3}$$

In Eq. 5.3, $MAPE_{X_0}$ and $MAPE_X$ denote the mean absolute percentage error of the QoI X before and after applying the FFT-based prediction. The FOM is therefore directly proportional to the error reduction between the initial guess and the final result obtained with the FFT-based approximation. Thus, a smaller FOM is related to a higher error reduction between successive iterates due to the use of the GTF-based prediction block.

5.1.3 Transfer Functions for the prediction block

The transfer functions represented in Fig. 5.4 for $\vec{\Sigma}_a$ and $\nu\vec{\Sigma}_f$ were calculated using three initial density profiles. The latter are represented by the blue lines with circular markers in Figs. 5.5.a-c. The densities were obtained from the reference Picard calculations at different iterations. The MAPE between $\{\rho_y\}_{y=a,b,c}$ and the reference density is 31.16%

for ρ_a, 11.18% for ρ_b, and 2.77% for ρ_c respectively. The subscript refers to the figure where they are represented, *i.e.*, ρ_a is represented in Fig. 5.5.a.

In this section, $H_X^{\rho_y}$ denotes the transfer function computed at ρ_y, for the QoI X. All the QoIs used to generate the transfer functions were computed by running 400 active batches, of which 150 inactive, with 100,000 particles. This led to a maximum standard deviation of 0.1% on the bin-wise value of all the QoIs.

The similarity between the different transfer functions can be easily noticed despite being generated for different density profiles. In fact, all the TFs reach their peak at zero frequency, before plateauing for higher components. It is noticeable that no coefficient is null. There are two motivations for this phenomenon. First, due to the presence of axial reflectors, the cross-sections present steep local gradients at the domain's boundaries. Therefore, high order coefficients are needed to describe the profile. Second, the DFT is applied to a non-periodic signal in a finite space-domain, giving origin to spectral leakage. An intuitive explanation of the phenomenon is that the periodic extension of the signal outside the observation window is not continuous. These apparent discontinuities at the boundaries have a complicated representation in the frequency domain leading to the need for high order expansions. This may constitute a problem if the FFT with hard threshold is utilized to denoise the MC output.

5.1.4 Solution of the BWR unit-cell and effect of the reference point

In this section, the BWR unit-cell problem with fresh fuel is solved using the prediction block. The results are compared with the reference coupled MC-TH solution obtained with the stabilized Picard iteration scheme and are summarized in Fig. 5.5. The columns within the plot refer to a unique initial density distribution ρ_0, while the rows are associated to a unique QoI. Each plot presents the initial distribution for the QoI (denoted by blue circles), its predicted value (denoted by red stars) and the reference solution (denoted by black smooth curve). The x-axis, in every figure, describes the active length of the unit-cell in

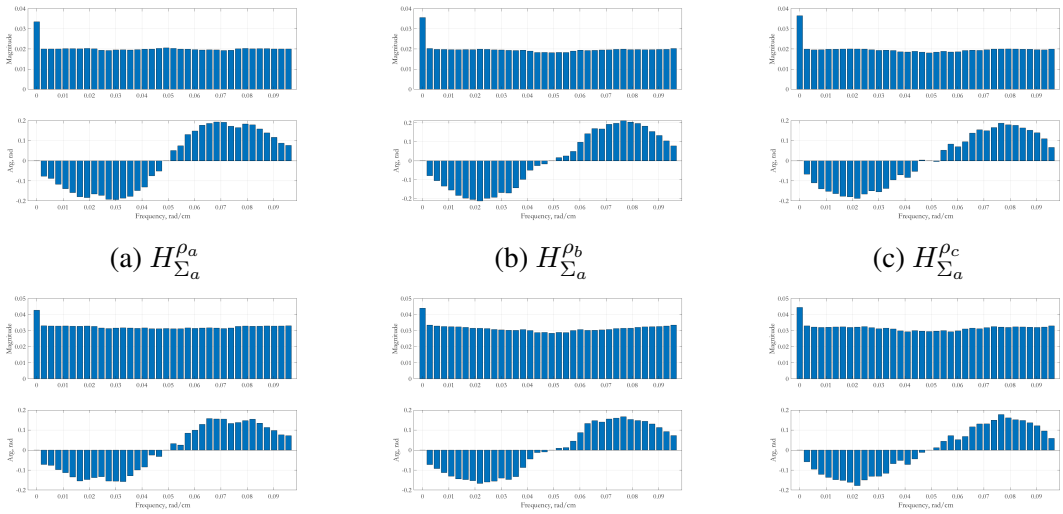

(a) $H^{\rho_a}_{\Sigma_a}$ (b) $H^{\rho_b}_{\Sigma_a}$ (c) $H^{\rho_c}_{\Sigma_a}$

(d) $H^{\rho_a}_{\nu\Sigma_f}$ (e) $H^{\rho_b}_{\nu\Sigma_f}$ (f) $H^{\rho_c}_{\nu\Sigma_f}$

Figure 5.4: Transfer functions calculated for different coolant density profiles. Plots (a)-(c) report the transfer function for the macroscopic absorption cross-section, while (d)-(f) present the TF for the fission neutrons' production.

centimeters, while the left and right ordinates report the value of the QoI in a proper unit of measure and of the PAD, respectively. The prediction of the QoIs, including the calculation of the transfer functions from the MC outputs, took less than one minute, and 30 seconds on a single processor for every choice of the initial guess. The multiplication factor was always within 120 pcm from the reference.

As expected, the results' accuracy improves as the initial density distribution approaches the actual solution of the problem. This consideration holds for all the QoIs. The behavior is expected since the transfer function is calculated in correspondence of this initial guess and is not updated along the FFT-TH iterations. In particular, referring to Table 5.2, where the MAPE is reported for all the QoIs as a function of the initial guess, the MAPE for the density ρ and the power P, is reduced from 1.6% to 0.15%. and from 16% to 2.8% respectively. The following observations are made for each QoI:

- Density, $\vec{\rho}$. The density profile is predicted within 10% accuracy in every bin and for any choice of the initial guess of spatial profile. The maximum error is 0.8% in the most favorable case, *i.e.*, leftmost plot in the first line, while the MAPE is 0.16%.

The maximum PAD is located in proximity of the bottom boundary. This is driven by the error in the power profile, dictated by the neglection of the leakage term in Eq. 4.13.

- Absorption macroscopic cross-section, $\vec{\Sigma}_a$.

  Figs. 5.5.d-f report the results for the absorption macroscopic cross-section. The PAD is maximum in the top half of the domain, *i.e.*, $z > 200$ cm. Here it reaches 11% and 2% for the least and most favorable case, respectively. This is due to the higher standard deviation associated to the MC-generated cross-sections and the associated spatial fluctuations that excite high order Fourier modes. This undermines the reliability of the prediction.

- Neutron fission production, $\nu\vec{\Sigma}_f$. The fission macroscopic cross-section is reported in Figs. 5.5.g-i. The PAD follows the same trend noticed for the absorption cross-section. The MAPE reduces from 3.3% to 0.53% when the density profile approaches the reference solution.

- Power profile, $\vec{P}$. The results for the power profile are reported in Figs. 5.5.j-l. The difference is maximum near the boundaries due to the neglection of the leakage term in the linear power update, Eq. 4.13. At the top of the geometry, the PAD reaches 30% and 6% for the least and most favorable case, respectively. The error propagates through the TH solver, affecting also the density profile's prediction. The MAPE is reduced from 15% to 2.76%.

The FOM for each of the QoI is reported in Table 5.3. It is noticeable that the density presents a reduction of two orders of magnitude in MAPE, *i.e.*, the error reduction is the inverse of the FOM. For the other QoIs, the prediction consistently entails an error reduction of one order of magnitude when the prediction block is applied.

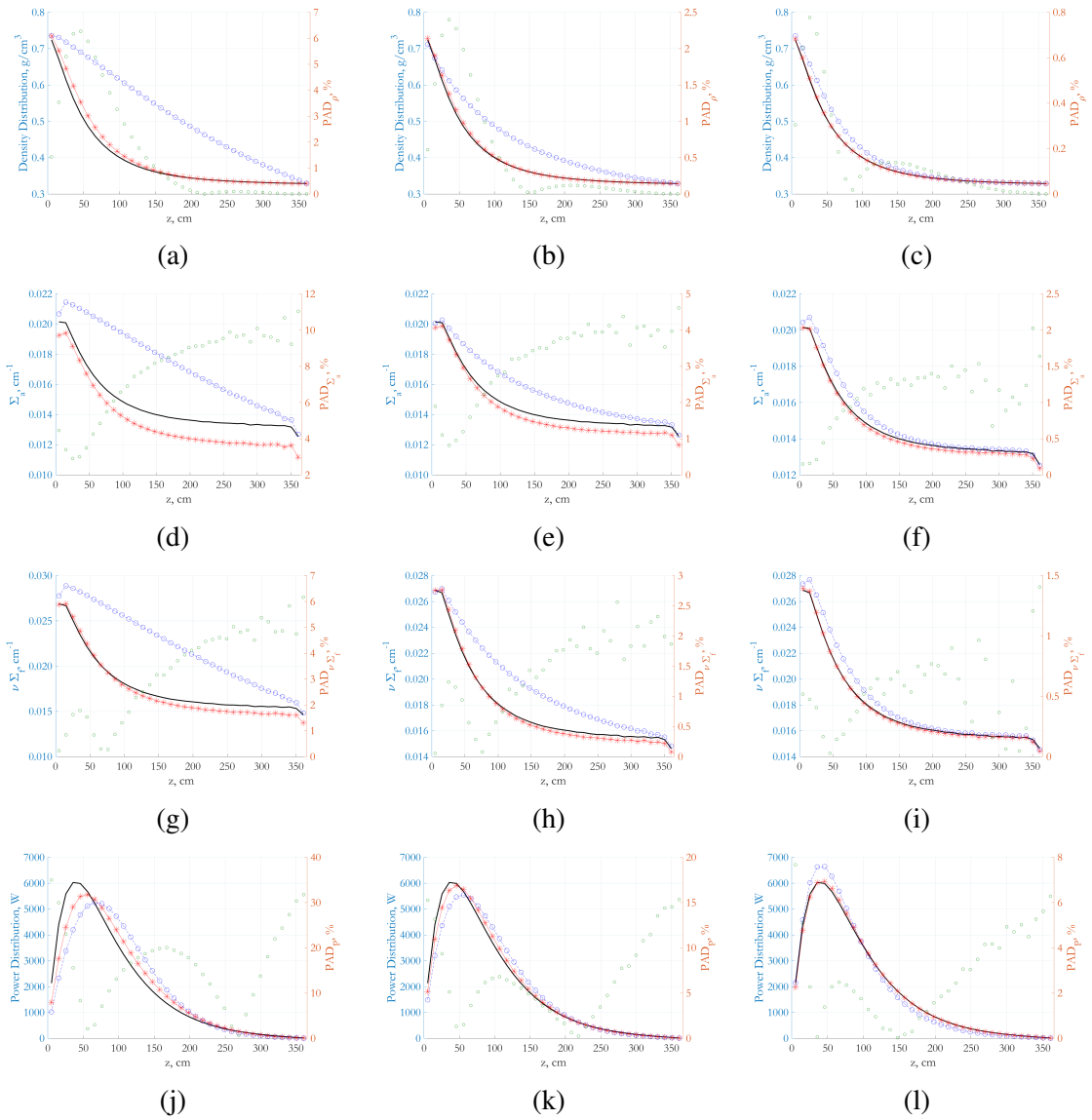

Figure 5.5: Solution of the BWR unit-cell problem with the GTF-FOP-TH prediction block. In each figure, the black solid line represents the reference solution, the red line with starred markers is the predicted solution, while the blue curve with the circular marker is the initial guess. Finally, the green dots represent the PAD between the reference and the prediction. Each row of plots is associated to a different QoI, *i.e.*, a-c to ρ, d-f to the absorption cross-section, g-i to the fission neutrons production, and j-l to the power, while the columns are for different density's initial guess.

Table 5.2: MAPE of the QoI for different initial guess $\rho_0^{(i)}$

Parameter/Initial Guess	$H^{\rho_0^{(1)}}$	$H^{\rho_0^{(2)}}$	$H^{\rho_0^{(3)}}$
ρ	1.6076	0.5026	0.1509
Σ_a	7.8030	3.2004	1.1073
$\nu\Sigma_f$	3.3085	1.4260	0.5315
Power	15.9987	6.5554	2.7601

Table 5.3: FOM of the QoIs for different initial guess $\rho_0^{(i)}$

Parameter/Initial Guess	$H^{\rho_0^{(1)}}$	$H^{\rho_0^{(2)}}$	$H^{\rho_0^{(3)}}$
ρ	5.16e-2	4.50e-2	5.45e-2
Σ_a	4.20e-1	4.66e-1	5.71e-1
$\nu\Sigma_f$	1.32e-1	1.54e-1	2.09e-1
Power	5.12e-1	3.81e-1	1.25e-1

5.1.5 Considerations on the effect of the statistics

This section discusses the effect of the batch size on the accuracy of the results. To perform this analysis, the neutron population is varied from 10,000 to 1,000,000 while the number of fission source iterations is set to 400 of which 150 are inactive. The density profile $\rho_0^{(3)}$, used to generate the results in the third column of Table 5.5, is utilized to generate all the transfer functions.

The MAPE for the macroscopic absorption cross-section and $\nu\vec{\Sigma}_f$ is reported as a function of the batch size in Table. 5.4. The error decreases monotonically as the batch size increases. The variation is maximum when the neutron population transits from 10,000 to 50,000 neutrons per batch.

To investigate the effect of extremely poor statistics where the variation of the MAPE is higher, we ran a case with 1,000 particles per cycles. The transfer functions are reported in Fig. 5.6. Comparing these TFs with the results in Fig. 5.4, it is noticeable that the statistical fluctuations undermine the quality of the TFs' estimations. This can propagate through the calculations, therefore hindering the accuracy of the methodology, as shown in Fig. 3.8.

Table 5.4: MAPE for different batch sizes.

MAPE/Batch Size	10^4	5×10^4	5×10^5	10^6
$MAPE_{\Sigma_a}$	1.4191	0.5362	0.5503	0.4793
$MAPE_{\nu\Sigma_f}$	1.6780	1.1519	1.1231	1.0890

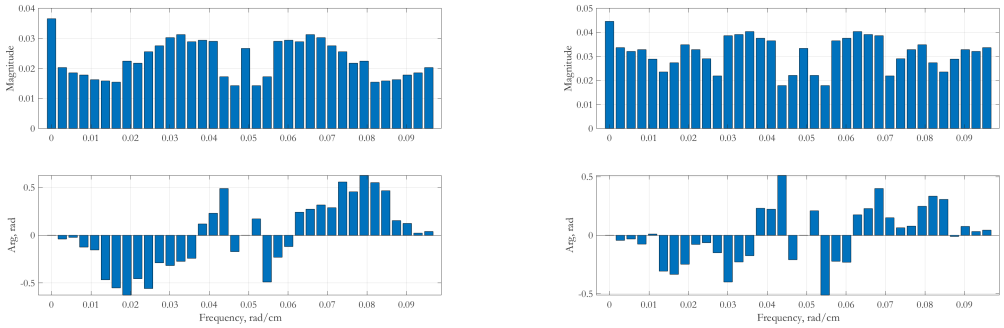

(a) (b)

Figure 5.6: Transfer Functions obtained with 1,000 particles per batch for (a) Absorption cross-section and (b) Fission neutrons production.

5.2 Multiple Variables, Stand-Alone Prediction

In this second part of the proof of concept, the TH feedback is expanded to account for both the effect of fuel temperature and density profile. After detailing the procedure to obtain a reference solution in Section 5.2.1, Section 5.2.2 analyzes the transfer functions and the corresponding cross-sections prediction as a function of the number of cycles. Considerations on the associated power prediction obtained through the perturbation-based formula is then presented in Sec. 5.2.3.

5.2.1 Reference Solution

The reference power spatial distribution, accounting for both fuel temperature and density-driven TH feedback, was generated by combining the converged solution of 8 independent Picard simulations. Each independent simulation was computed using 50 Picard iterations. Within each Picard iteration, 1,000,000 particles per cycle were run for a total of 700 cycles, of which 400 were inactive. This procedure led to a root mean square power standard

deviation of 0.13%, and a multiplication factor standard deviation of 2 pcm. The domain was discretized in 38 axial layers, of which 36 are equal-height cells in the active zone.

In order to show the convergence of the profiles used to obtain the reference solutions, Fig. 5.7 shows the expected value of the multiplication factor, together with the power, density, and fuel temperature profile at selected iterations for one of the 8 independent simulations. The corresponding L2 norm of the residual for power and density profile are reported in Fig. 5.7 as a function of the number of iterations. These two relative residual constitute the most stringent and the least stringent convergence criterion respectively. The uncertainty is not propagated through the calculations and, therefore, is not reported.

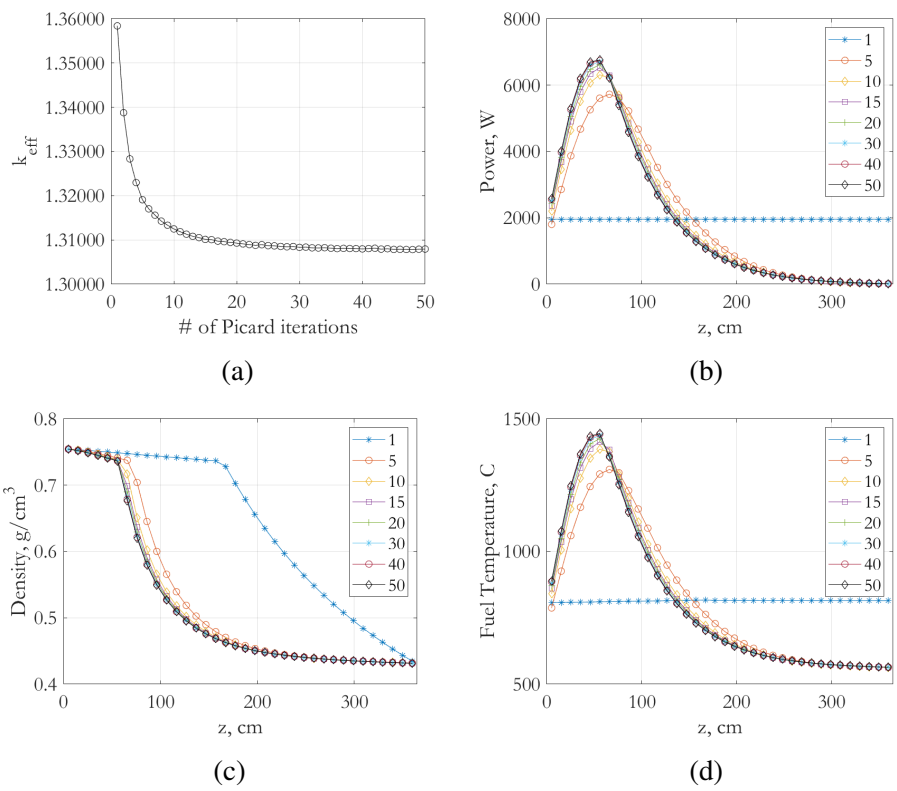

Figure 5.7: (a) k-eff as a function of MC-TH iteration's number, (b) Power spatial distribution for selected iterations,(c) Density spatial profile for selected iterations, and (d) Fuel temperature for selected iterations.

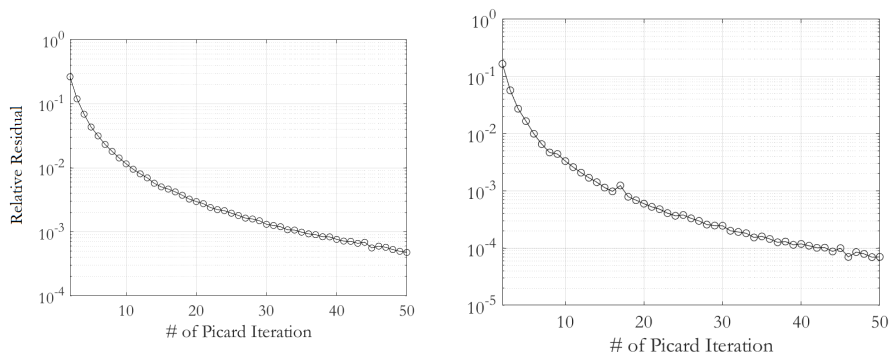

(a) (b)

Figure 5.8: L2-norm of the relative residual as a function of the Picard iterations number for (a) Power spatial profile, and (b) Density spatial profile.

5.2.2 Transfer Functions and choice of the independent variable

The transfer functions illustrated in Figs. 5.11-5.9 were generated using 19 Picard iterations. Within each Picard iteration, 300,000 particles were run for 400 cycles of which 200 inactive. TH profiles computed from a non-accelerated Picard sequence were used to mimic the insertion of the prediction block in the full PI algorithmic sequence. In Fig. 5.9, the transfer function obtained using $\vec{\xi}$ as independent variable are represented by the red lines with circular markers. The black line with star markers represent the transfer functions with respect to the density profiles. The continuous-line representation was used in lieu of the bin-chart representation employed in Sec. 5.1 for the sake of easier graphical comparison. The variables were also normalized in order to obtain a dimension-less input variable and the same scale for the magnitude of the TFs.

It can be noticed the the transfer functions calculated with respect to $\vec{\xi}$ and $\vec{\rho}$ have similar behavior in terms of both real and imaginary component, denoted respectively as ”magnitude” and ”arg” in the Bode diagram. However, they exhibit an important difference in terms of magnitude. While the TF computed using the density as independent variable presents a peak in correspondence of the zero mode followed by a plateau, the TF presents two local minima. The first depression is in correspondence of the few modes following the zeroth component. The second occurs for the higher modes, *i.e.*, mode index above 34.

These components are usually associated with the stochastic noise. Since, using a good enough statistics, we can assume that the noise in each axial node is spatially uncorrelated, its spatial frequency is expected to match the number of nodes. This behavior was observed at every iteration and for both the macroscopic cross-sections of interest. This is clearly visible in Fig. 5.9-5.10, where the TFs are reported at selected iterations for Σ_a and $\nu\Sigma_f$ respetively.

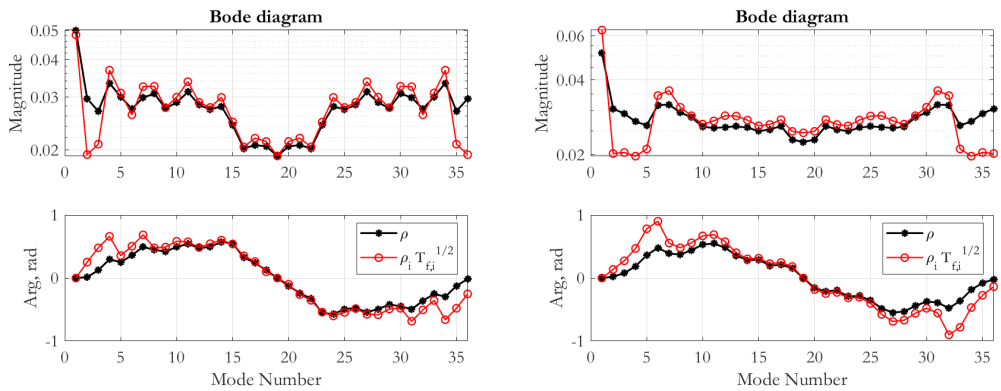

(a) (b)

Figure 5.9: Bode diagram of the absorption cross-sections' transfer functions calculated at Picard (a)iteration 1, and (b) iteration 19. The line with circular marker is the transfer function calculated using $\vec{\xi}$ as independent variable. The line with star markers is the TF computed using the density as independent variable.

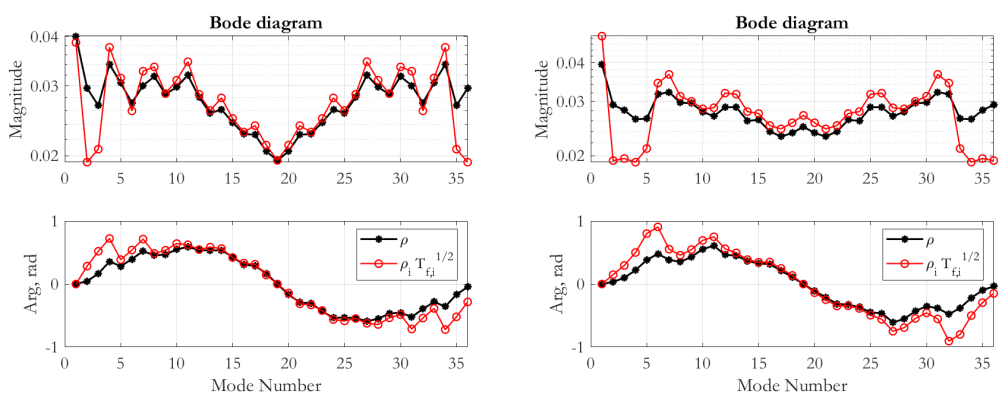

(a) (b)

Figure 5.10: Bode diagram of the secondary neutron production cross-sections' transfer functions calculated at Picard (a)iteration 1, and (b) iteration 19. The line with circular marker is the transfer function calculated using $\vec{\xi}$ as independent variable. The line with star markers is the TF computed using the density as independent variable.

The ability of the TFs to correctly predict the macroscopic cross-sections at different Picard iterations was studied in Figs. 5.12-5.9, where the reference cross-sections $\Sigma_x(\vec{T}_f, \vec{\rho})$, denoted by a solid black line, are compared against the ones predicted through the transfer functions $\Sigma^*(\vec{T}_f, \vec{\rho})$, represented by the green dashed line with star markers. The blue line with circular markers is the initial guess, *i.e.*, the cross-section associated to the initial state at which the transfer function is calculated. It is noticeable that, consistent with the single feedback case, the transfer functions can capture the TH-driven cross-sections' variation. Moreover, the prediction improves as the reference point at which the transfer function is calculated $\left(\vec{T}_f^0, \vec{\rho}^{\,0}\right)$ gets closer to the state at which the cross-sections must be evaluated $\left(\vec{T}_f, \vec{\rho}\right)$. The Percentage Absolute Difference (PAD), as defined in Eq. 5.1, is maximum at the top of the unit-cell where the standard deviation reaches the maximum value. The Root Mean Square Error (RMSE) of the cross-sections prediction is reported as a function of the Picard iteration number in Fig. 5.12 and Fig. 5.9 for Σ_a and $\nu\Sigma_f$ respectively. It is noticeable that the error correctly decreases with number of the iterations in both cases. For both the cross-sections of interest the interplay between deterministic and stochastic component of the error for an iteration number larger than twelve when they reach the same order of magnitude.

5.2.3 Analysis of power prediction

The power profiles predicted with Eqs. 4.11-4.13 are shown in Fig. 5.13. The cross-sections analyzed in Section 5.2.2 were utilized as inputs for the calculation of the expansion coefficients in Eq. 4.13. In Figs. 5.13.a-c, the blue curves represent the power profile's initial guess, *i.e.*, the power extracted at Picard iterations 1, 5, and 10 respectively. The power profile predicted by using the first order perturbation theory in conjunction with the transfer function formalism are denoted by the red and green curve. The red curve is computed by using 1 iteration between the TH code and the reduced order neutronic solver within the prediction block. The green curve is obtained by performing 5 iterations between TH and

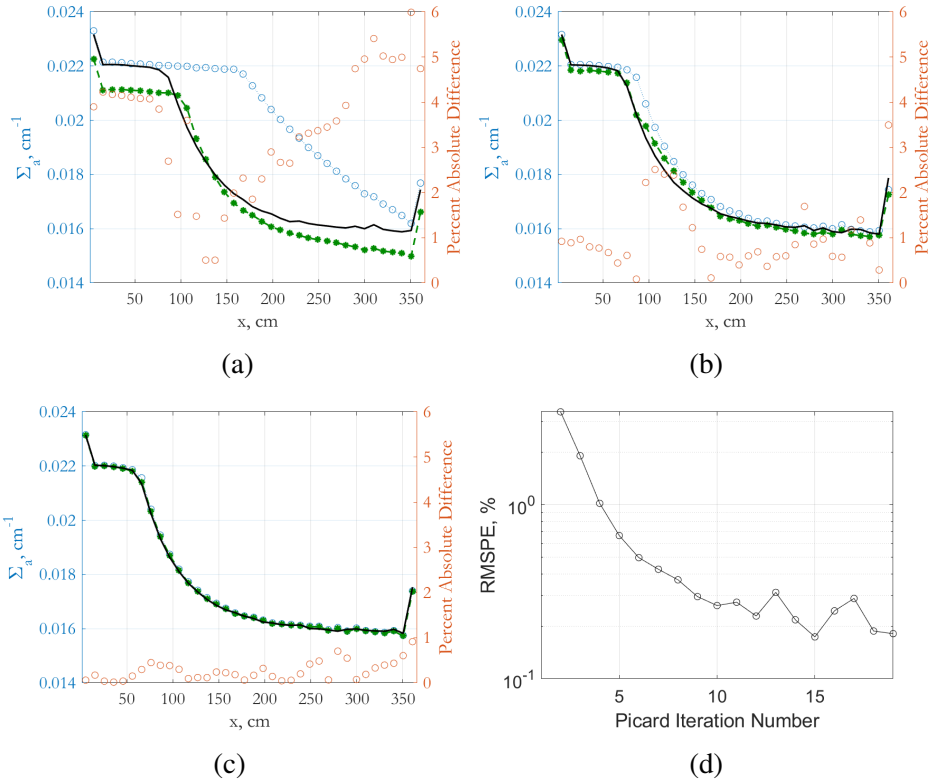

Figure 5.11: Comparison of the absorption cross-sections prediction at selected Picard iteration numbers against reference: (a)Iteration 1, (b) Iteration 3,(c) Iteration 10. In each figure, the black solid line represents the target distribution, *i.e.*, cross-section at the next iteration, the green dashed line with circles is the predicted cross-section, while the blue line with circular markers is the initial guess. (d) The L2 error from the reference solution as a function of the iteration number.

reduced order neutronic solver. It can be noticed that the use of multiple iterations amplifies the effect of the prediction. This phenomenon improves the efficacy of the prediction block in the first iteration when the solution is far away from the reference. However, when multiple prediction iterations are used in close proximity to the fixed point, *i.e.*, for iteration numbers higher than one, this leads to drift away from the correct solution. The phenomenon is clearly illustrated in Fig. 5.13.b, where the predicted and reference power are shown for the third Picard iteration. This occurs because the first order perturbation formula utilized in the predictor block is not a consistent approximation of the neutron transport equation. In other words, the solution drifts away from the reference, constituted by the solution of the transport equation, towards a different power profile P^*. The differ-

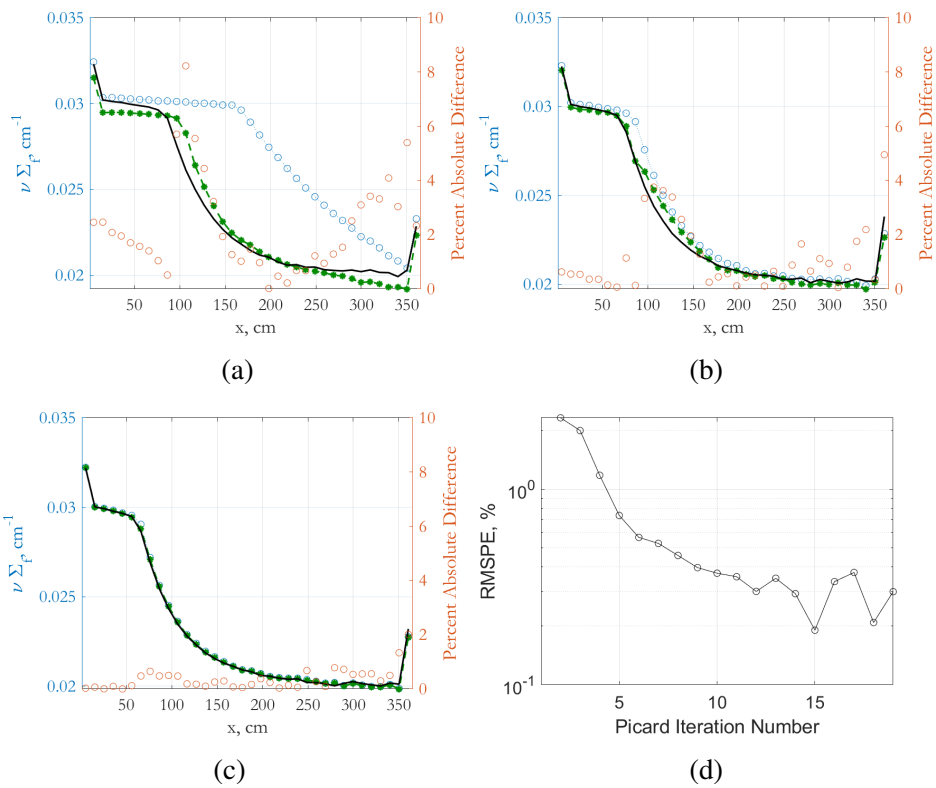

Figure 5.12: Comparison of the secondary neutron emission prediction at selected Picard iteration numbers against the reference: (a)Iteration 1, (b) Iteration 3,(c) Iteration 10. In each figure, the black solid line represents the target distribution, *i.e.*, cross-section at the next iteration, the green dashed line is the predicted cross-section, while the blue line with circular markers is the initial guess. (d) The L2 error from the reference solution as a function of the iteration number.

ence between P^* and the reference is 4.52% in L2 norm when 5 iterations are employed within the prediction block. This discrepancy decreases to 2.52% if a single prediction iteration is used.

Further observations can be made by considering the predicted fuel temperature and density spatial profiles, *i.e.*, TH fields associated to the predicted power profile. The relative error associated to these TH fields is reported as a function of the iteration number in Fig. 5.14. It can be noticed that, as for the predicted power, the error associated to the TH fields decreases with the number of iterations until it reaches a limit of accuracy dictated by the inconsistency of the approximation and the stochastic component of the error. Additionally, it must be noticed that the error is lower than the one associated to the power

profile, reaching 1.17% for the fuel temperature and 0.520% for the moderator density at the 20th iteration.

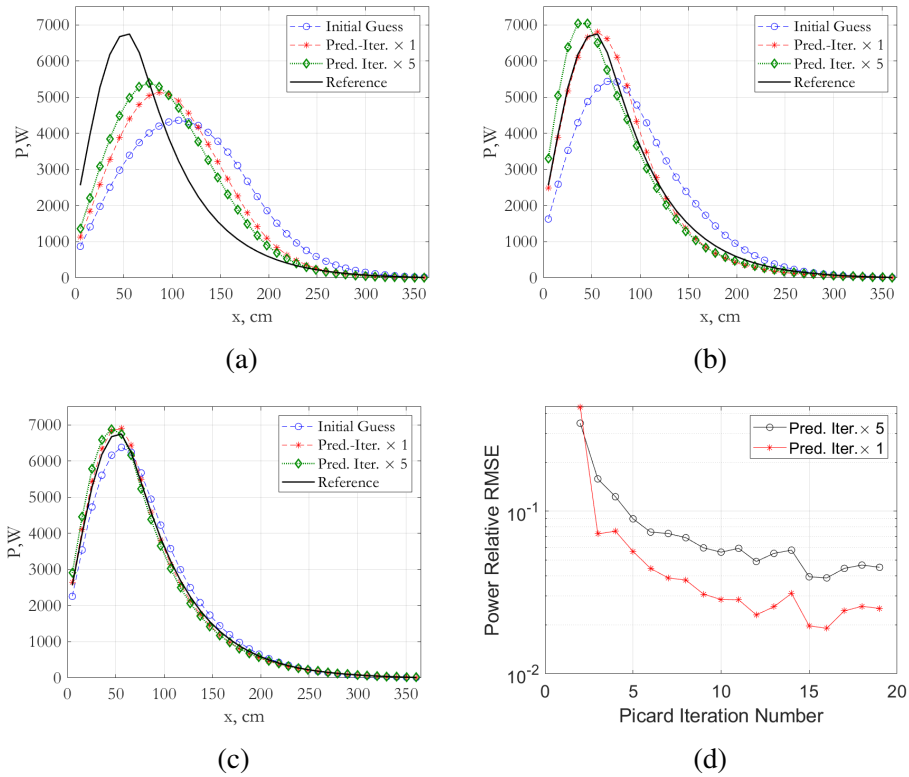

Figure 5.13: Comparison of the power prediction at selected Picard iteration numbers against reference: (a)Iteration 1, (b) Iteration 3,(c) Iteration 10. In each figure, the black solid line represents the reference power profile; the green dashed line is the predicted power after 5 prediction iterations; the red line is the predicted power after one prediction iteration; the blue line with circular markers is the initial guess. (d) The L2 relative error from the reference solution as a function of the Picard iteration number.

5.3 Multiple Variables, Fully-Integrated Sequence

In this section, the power prediction block including generalized transfer function methodology for cross-sections' prediction and first order perturbation for the power prediction, is integrated into the full Picard iteration sequence. The main objective of this section is to quantify the speed up achievable by employing the GTF-based acceleration to the BWR unit-cell problem described in Section 5.1.1.

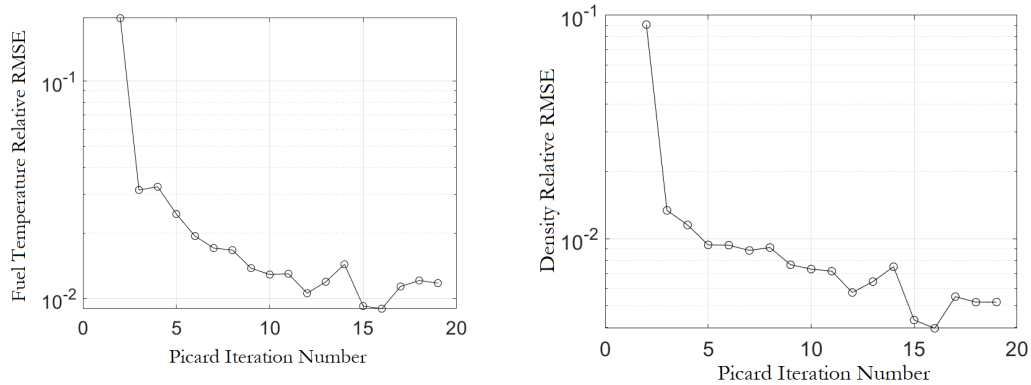

(a) (b)

Figure 5.14: The relative error for (a) the predicted fuel temperature T_f, and the (b) the predicted density ρ, as a function of the Picard iteration number.

The remainder of the section is structured as follows. Section 5.3.2 analyzes the convergence of the algorithm based on the power residual. In particular, it will be shown that a tighter coupling between neutronics and thermal hydraulics, *i.e.*, more frequent data exchange between TH and MC solver, can lead to faster convergence. The residual and error analysis are reported in Section 5.3.2 while the dependence on the number of criticality cycle per Picard iteration is addressed in Section 5.3.3.

5.3.1 Metrics

The following metrics are defined to compare the performance of the PI and the GTF-accelerated PI, denoted as GTF+PI:

- The L2 norm of the relative power residual, $|r|_P^i$, is used to measure the precision of the algorithms. The latter is defined as:

$$|r|_P^i = \frac{||\vec{P}_i - \vec{P}_{i-1}||_2}{||\vec{P}_{i-1}||_2}, \tag{5.4}$$

  where $\vec{P}_i$ and $\vec{P}_{i-1}$ are the power distributions calculated at iteration i and $i-1$ respectively. We decided to define the residual with respect to the power since this

constitutes the most stringent criterion for convergence compared to the analogous residuals defined for the TH fields.

- The accuracy is compared both in terms of TH fields and power profile using the L2 norm of the percentage error. For the power:

$$|e|_P = \frac{||\vec{P} - \vec{P}_{ref}||_2}{||\vec{P}_{ref}||_2} \times 100, \tag{5.5}$$

  where $\vec{P}_{ref}$ denotes the reference solution. Analogous formulas are defined for the fuel temperature and density.

- A Figure of Merit for the fully-integrated sequence, (FOM_f), is introduced to express the effective speed-up obtained with the GTF-based acceleration. If CC' is the number of criticality cycles for the accelerated algorithm to converge, and $CC(|e|_P)$ is the number of criticality cycles of the standard PI algorithm to achieve the same L2 norm of the power relative error, we can define the FOM in the following manner:

$$FOM_f = \frac{CC(|e|_P)}{CC'} \tag{5.6}$$

  The subscript f is introduced to distinguish this FOM from the one defined in Section 5.1.2. Notice that higher FOM_f denotes a better performance of the algorithm. Additionally, we did not express the FOM in terms of wall-clock time. This is because the MATLAB code implementing the acceleration algorithm is not optimized, therefore constituting an unfair comparison. Future work will address the inclusion of the wall-clock time in the FOM for the fully-integrated sequence.

5.3.2 Residual and Error Analysis

The BWR unit-cell problem is here solved using the standard Picard iteration method with Robbins-Monro relaxation and the GTF-accelerated algorithm. The results are then com-

pared in terms of convergence speed and accuracy with respect to the reference solution. Fig. 5.15 illustrates qualitatively the different convergence behavior for the standard PI and the GTF-accelerated scheme. The left column of Fig. 5.15 shows the power, fuel temperature, moderator density, and moderator temperature calculated with the standard algorithm. The right column of the Fig. 5.15 reports the same quantities calculated with the GTF-accelerated scheme. The spatial distributions are shown for selected iterations. In both cases, the solution was obtained by imposing a tolerance of 0.1% on the relative power residual. At each Picard iteration, 400 criticality cycles were performed, with 300,000 particles per cycle. The statistics was chosen in order to obtain a mean square standard deviation lower than the set tolerance on the power relative residual and to ensure a converged solution at the end of each Picard iteration.

As noticeable from Fig. 5.15.a-c, the convergence was achieved after 37 Picard iteration for the non-accelerated algorithm and after 7 iterations for the GTF-based acceleration, resulting in a 5.28 cycle-wise speedup. The acceleration is evident by comparing the two columns of Fig. 5.15. In fact, while the fixed point is gradually approached in absence of GTF-based acceleration, the power relative residual associated to the GTF-accelerated algorithm collapses under 1% in 5 iteration. This is emphasized in Fig. 5.16, where the residual for the two simulations is shown as a function of the number of Picard iterations; the blue curve, representing the power relative residual for the standard PI algotithm and the red curve the one for the GTF-accelerated scheme. It is noticeable the smoothness of both curves. This is because the stochastic component of the error e_s and the deterministic part e_d have different order of magnitude, *i.e.*, $e_d > e_s$. The speed-up in terms of residual is reported in Tab. 5.5 for different tolerance levels imposed on relative power residual: 10%, 1%, and 0.1%. In all cases the use of the GTF results in a speed gain as shown by the last column of the table, where the speed-up factor is reported as a function of the tolerance.

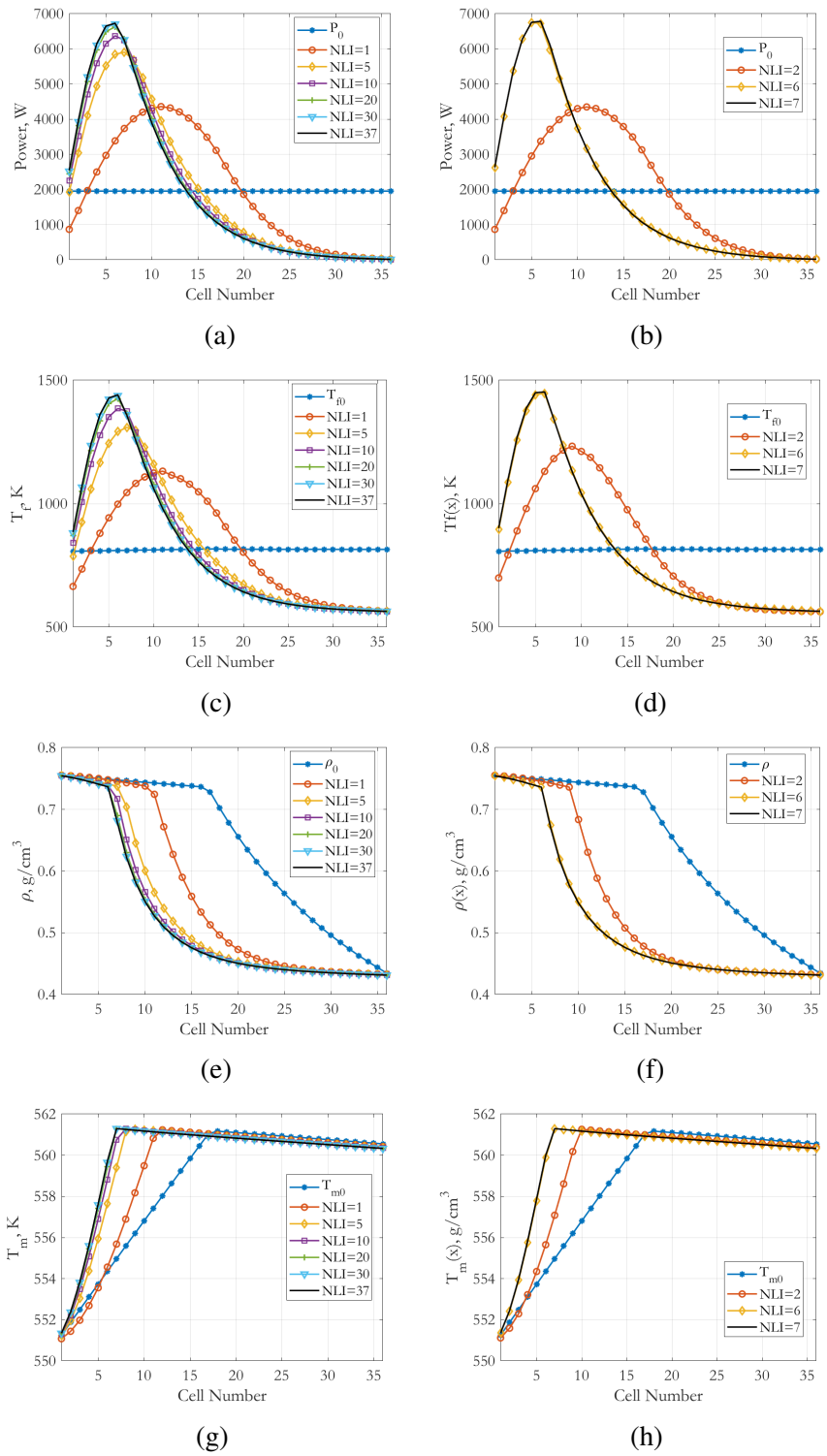

Figure 5.15: The figure reports the solution of the BWR unit-cell problem obtained with the PI method (Alg. 1) and with the GTF-accelerated PI method (Alg. 2). (a) Power with Alg. 1, (b) Power with Alg. 2, (c) Fuel Temperature with Alg. 1, (d) Fuel Temperature with Alg. 2, (e) Moderator Density with Alg. 1, (f) Moderator Density with Alg. 2, (g) Moderator Temperature with Alg. 1, (h) Moderator Temperature with Alg. 2.

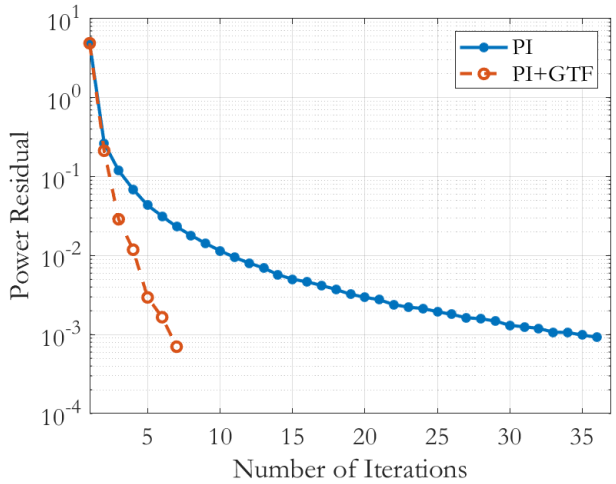

Figure 5.16: Comparison of the relative power residual as a function of the iteration. The blue curve represents relative power residual for the standard PI algorithm, while the red curve is associated to the GTF-accelerated PI scheme.

Table 5.5: Cycles at which the prescribed tolerance is achieved for the PI algorithm and the GTF-accelerated scheme, together with the corresponding speed-up.

Tolerance/Cycle	**PI**	**PI+GTF**	**Speed-up**
0.1	4	3	1.3
0.01	11	5	2.2
0.001	36	7	5.1

The relative error between the GTF-accelerated solution and the reference is 1.98% in L2 norm. This is outside the 3σ interval for the relative error estimated to be 1.28%. The discrepancy between the two spatial profile is caused by the approximations the reduced order neutronic solver relies on, *e.g.*, the use of the FM modes rather than the flux modes. These approximations make the estimator not consistent with respect to the LTE. However, the standard algorithm needs to perform 15 iterations in lieu of 7 in order to obtain the same level of accuracy. Therefore, the use of the GTF-based acceleration results into a speed-up of 2.1. The GTF acceleration can then be utilized to get in proximity of the fixed point before relying on the PI algorithm to converge to the correct solution within the 3σ region.

5.3.3 Dependence on Number of Criticality Cycles per Picard Iteration

Sensitivity studies were performed to understand the effect of varying the number of criticality cycles performed at each Picard iteration. In fact, a ”tighter coupling” between the MC and TH solver is obtained by decreasing the number of criticality cycles. This is the result of more frequent data exchange between the two single-physics codes, *i.e.*, the expected value of the power spatial profile from the MC code to the TH code, and the temperature and density spatial profiles from the TH code to the MC code. The main objective of this section is to understand if we can further push the speed up factor by increasing the frequency of the prediction.

The results of the sensitivity analysis are reported in Fig. 5.17. Each curve is obtained from a different simulation. The solid curves are associated to simulations not making use of the GTF-based prediction, while the dotted curves are associated to the ones employing the accelerated PI algorithm. The values associated to the curves, *i.e.*, $n_{it} = \{20, 100, 400\}$, refer to the number of criticality cycles performed at each Picard iteration. For the curves obtained from GTF-accelerated this value also matches the number of criticality cycles between two consecutive predictions. All the curves are generated using 300,000 particles per cycle, therefore not conserving the total number of particles per simulation.

From Fig. 5.16, two main observations can be drawn. First, a lower number of criticality cycles leads to faster convergence of the iterates. Second, is that the GTF-based acceleration is able to increase the convergence rate for an equal number criticality cycles. In particular, it can be noticed that, by using only 20 criticality cycles per Picard iteration, the convergence is reached 160 criticality cycles as opposed to the non-accelerated case, where more than 1,000 criticality cycles are needed. On the other, the lower statistics utilized to compute the power profile for $n_{it} < 400$ increases the uncertainty associated to the iterates, as visible from the curves representing the residual for simulations employing 20 criticality cycles per Picard simulations. In fact, local oscillations can be observed due to the interplay between the deterministic and stochastic component of the error in curve 20

and 20+GTF.

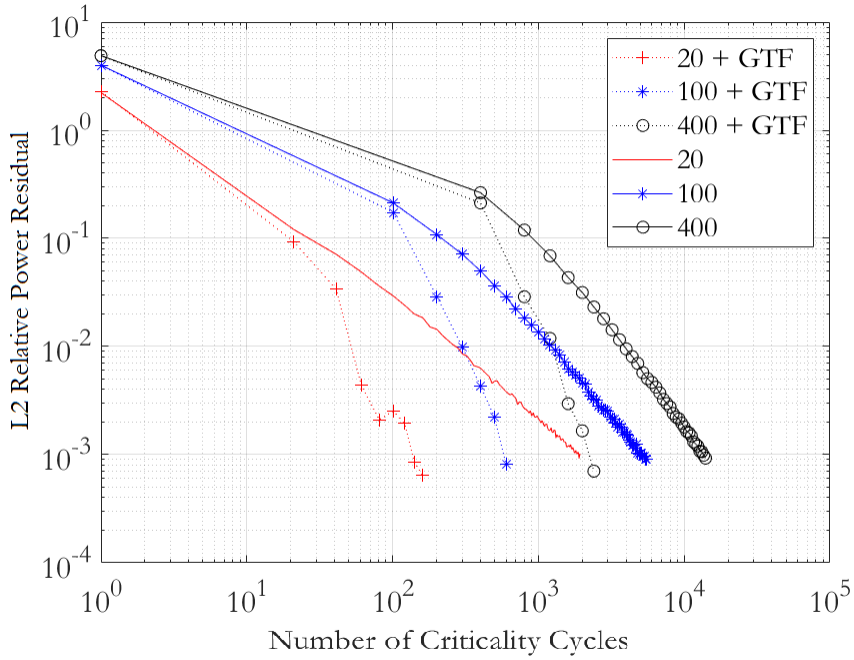

Figure 5.17: L2 norm of the power relative residual as a function of the iteration number.

A more problematic consequence of using less criticality cycles with a fixed number of particles per cycle is that non-converged power iterated are utilized in lieu of the MC-converged power profiles. The use of non-converged power profiles, in synergy with the Robbins-Monro stochastic approximation can lead the simulation to converge to an incorrect fixed point. An extreme case occurs for 20 criticality cycles in absence of acceleration. The converged power profile for the latter case is represented by the solid red line with plus markers in Fig. 5.18.a. The curve has RMSE of 27.21% from the reference curve represented by the black solid line. The inaccuracy of the obtained power profile also propagates into the TH fields, as visible in Figs. 5.18.b-c, where the fuel temperature and moderator density profiles are reported. It must be noticed that the analogous curve computed by performing the prediction every 20 criticality, represented by the red dotted curve with plus markers, is not affected by the same issue. This is because the GTF-based acceleration allows to reach convergence before the synergistic effect of the Robbins-Monro and the

use of non-converged power iterates emerges. The power profiles for the other scenarios, *i.e.*, $n_{it} = \{100, 400\}$ are also represented in Fig. 5.18. These curves are much closer to the reference, with a maximum relative RMSE of 3.895% for the case with 100 cycles in absence of GTF-based acceleration, represented by the solid blue curve with star markers, to 1.997% for the 400+GTF curve, represented by the black dotted curve with circular markers.

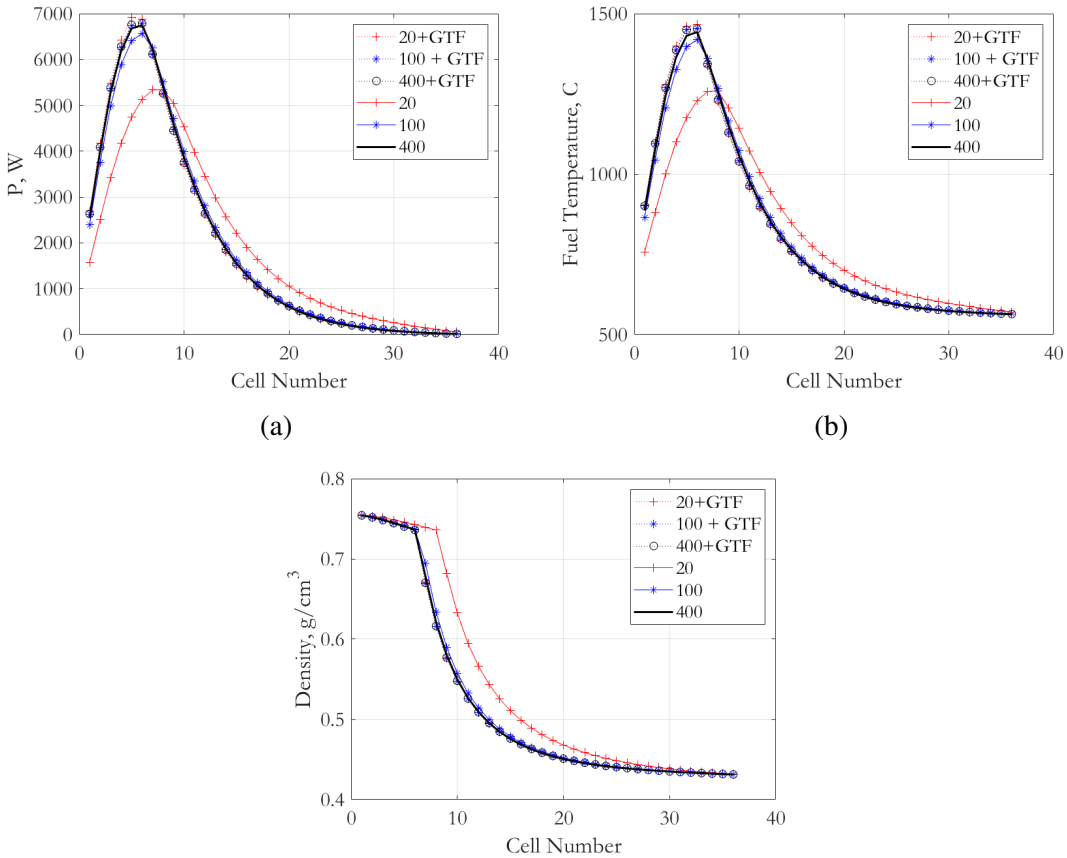

Figure 5.18: L2-residual as a function of the Picard iterations' number for (a) Power, (b) Density, and (c) Fuel temperature.

The L2-norm of the relative error for power, fuel temperature, and density is reported in the first three rows of Tab. 5.6. It is evident that the power relative error is the most stringent criterion to determine the accuracy of the GTF-accelerated PI algorithm, while the density error is the less rigid, being one order of magnitude lower than the error associated to the

power and the fuel temperature. In particular, we were able to obtain an estimation of the density within a margin of 0.36% from the reference in every case employing the GTF. The last row of the table reports the values of the FOM for the different cases. The highest FOM is obtained for the 20+GTF case, where a speed up factor exceeding 12 was achieved. while it is not convenient to decrease the number of criticality cycles without prediction, *i.e.*, FOM below one.

Table 5.6: FOM and speedup for GTF+PI compared to standard PI scheme.

Simulation Parameter	**20**	**20+GTF**	**100**	**100+GTF**	**400+GTF**
$\lvert e\rvert_{\vec{P}}$, %	27.21	3.426	3.895	1.783	1.997
$\lvert e\rvert_{\vec{T}_f}$, %	12.11	1.78	1.70	1.23	1.25
$\lvert e\rvert_{\vec{\rho}}$, %	7.07	0.35	0.83	0.36	0.32
FOM_f	0.4214	12.4286	0.3638	5.9917	2.1429

5.4 Summary

In this chapter, an axially-extruded BWR unit-cell with axial reflector was utilized as test case to obtain indications on the strengths and weaknesses of the GTF-based acceleration block. The analysis was performed in three steps.

1. In the first step, the ability of the prediction block to estimate the power was evaluated in a stand-alone fashion and by considering a single TH feedback, *i.e.*, the density feedback. A good agreement was observed between the predicted quantities of interest and the reference solution, with the approximation fidelity increasing as the distance between the initial guess, *i.e.*, the state at which the transfer function is computed, and the point at which the transfer functions must be computed decreases.

2. In the second step, multiple TH feedback mechanisms were incorporated by calculating the transfer function with respect to a new variable $\vec{\xi} = \vec{\rho} \circ \vec{T}_f$. It was demonstrated the ability to capture the TH-driven variation of the cross-sections of interest. In particular, it was noticed that single iteration within the prediction block

was able to maximize the convergence speed while minimizing the error associated to the prediction.

3. Finally, the prediction block was integrated into the full PI sequence to accelerate the Picard iteration algorithm considering both the effects of fuel temperature and moderator density. We have demonstrated that the accelerated sequence has a faster convergence than the original PI iterates sequence in terms of L2 norm of the residual. In particular, it was shown that more frequent predictions can lead to higher FOM for the algorithm, while obtaining a negligible influence on the accuracy of the method.

CHAPTER 6
THREE-DIMENSIONAL RESULTS

The chapter presents the application of the GTF-accelerated Picard iteration scheme to a PWR-based mini-core with three levels of enrichment. The latter configuration is studied for two different inlet coolant temperature, *i.e.*, 290°C and 315°C respectively, to analyze the ability of the predictor to capture the power variation in presence of both single-phase and two-phase flow. The different flow conditions leads to different convergence properties for the Picard iterates, therefore, affecting the GTF-based acceleration performance.

The remainder of the chapter is structured as follows. Section 6.1 describes the problem's geometry and material specifications. In Section 6.3, the reference solution is computed using an inlet temperature of 290°C. The predictor is then studied in stand-alone fashion in Section 6.4 before integrating it into the full sequence in Section 6.5. The same problem is then solved for an inlet coolant temperature of 315^{c}ircC in Section 6.6. A summary of this chapter's results is then provided in Section 6.7.

6.1 PWR-based mini-core description

The problem relies on a three-dimensional 3×3 super-cell with three levels of enrichment and surrounded by neutron reflectors. The radial and axial view of the geometry is reported in Fig. 6.1. The central element, *i.e.*, position B2 in Fig. 6.1.a, has an enrichment of 3.4 wt%. The assemblies at the corners, *i.e*, positions A1, C1, A3, and C3, have an enrichment of 1.6 wt%. Finally, an enrichment of 2.4% was chosen for the peripheral assemblies in positions A2, C2, B1, and B3. The enrichment values were picked from the BEAVRS reactor benchmark and chosen to maximize the radial peaking [60]. The latter decision was made to render the problem more challenging for the GTF-based acceleration. The active section of the super-cell is radially surrounded by a layer of 21.417 cm reflector,

modeled as a homogenized mixture of water and structural material. A 20 cm reflector surrounds the active core in the axial direction.

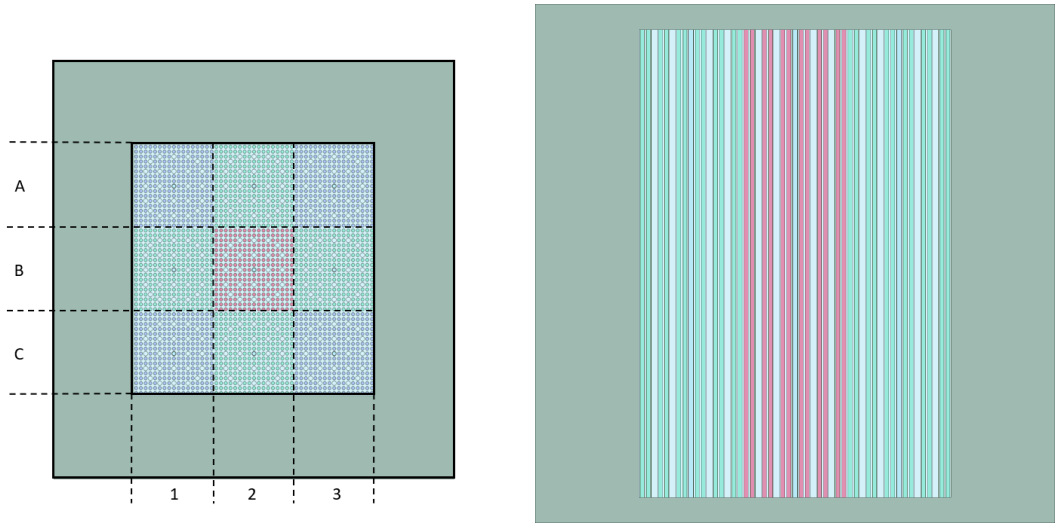

(a) (b)

Figure 6.1: (a) Radial view and (b) Axial View of the mini-core geometry.

Each assembly contains 17×17 pins. Of these, 264 are fuel pins, 24 are guiding tubes, one is an instrumentation tube (central pin). The pins are distributed as illustrated in Fig. 6.2. The internal structure and material distribution of each pin-type are reported in Fig. 6.3. The tables below each pin-type's plot report the value of the radii and the name of the materials contained within. In the framework of this chapter, the clad is modeled as pure zirconium, while air is a binary mixture, composed of 79% nitrogen and 21% oxygen. The fuel is uranium dioxide, where the uranium isotopic was reduced to a ternary mixture of U-235, U-238, and O-16. Table 6.1 reports additional geometrical and physical specifications together with the TH parameters.

The problem is discretized into 20 axial layers and 9 radial cells, the latter coinciding with the fuel assemblies. The TH variables are assumed to vary homogeneously within each discretization cell. The problem is solved for a water inlet temperature of 290 ^oC. In Section 6.6, the problem is solved with a coolant inlet temperature of 315 ^oC to further investigate the algorithm's performance when two-phase flow arises.

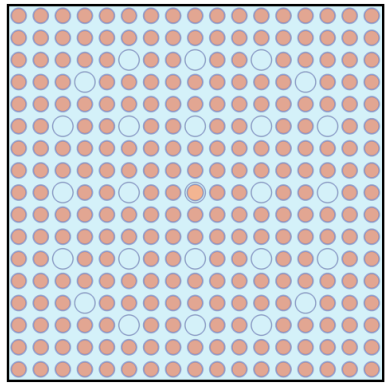

Figure 6.2: Radial view of single 17×17 fuel assembly. The problem contains three type of pins: (1) 264 fuel pin, (2) 24 guiding tube, and (3) 1 instrumentation tube in the center of the assembly.

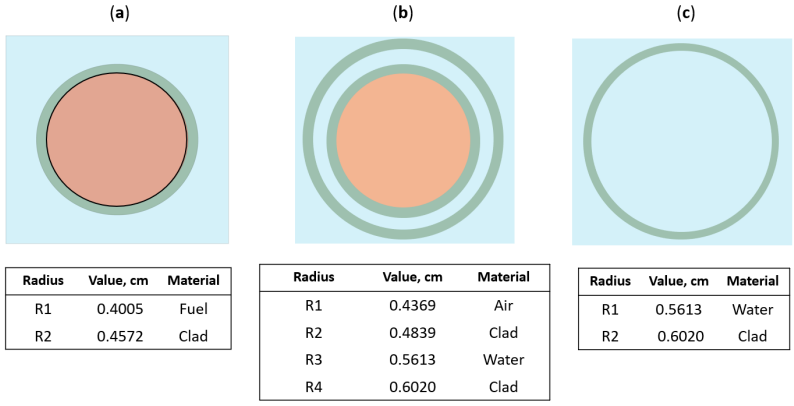

Figure 6.3: Dimensions and material specification for (a) fuel pin, (b) instrumentation tube, and (c) guiding tube.

Table 6.1: PWR 3×3 super-cell problem specifications

Parameter	**Value**
Total Height, cm	405.76
Top Axial Reflectors' Height, cm	20.00
Bottom Axial Reflectors' Height, cm	20.00
Radial Reflector' Width, cm	21.47
Assembly pitch, cm	21.47
Pin Pitch, cm	1.26
Inlet Pressure, bar	15.5
Mass flow rate, kg/s	900
Zr cladding density, g/cm^3	6.5514
UO_2 density, g/cm^3	10.42

6.2 Additional Metrics

In addition to the metrics defined in Section 5.3.1, the following two quantities are introduced to analyze the three-dimensional power distribution:

- The L2 norm of the percentage radially-integrated power error, $|e^a|_P$, is defined as:

$$|e^a|_P = \frac{|\sum_{j=1}^{N_C H} \left(\vec{P}^j - P^j_{ref}\right)|_2}{|\sum_{j=1}^{N_C H} \vec{P}^j_{ref}|_2} \times 100, \tag{6.1}$$

  where N_{CH} is the number of vertical channel, *i.e.*, assemblies, $\vec{P}^j$ is the power distribution in channel j, and the subscript ref is associated to the reference solution.

- The L2 norm of percentage axially-integrated power $|e^r|_P$ error is defined as:

$$|e^r|_P = \frac{|\sum_{j=1}^{N_z} \left(\vec{P}^j - P^j_{ref}\right)|_2}{|\sum_{j=1}^{N_z} \vec{P}^j_{ref}|_2} \times 100, \tag{6.2}$$

  where N_z is the number of axial discretization levels.

6.3 Reference Results

The reference results were obtained by averaging the spatial distributions obtained from 6 independent simulations. A tolerance below 0.1% in relative power residual was chosen as stopping criterion for the simulations. At each Picard iteration, 700 criticality cycles, of which 400 inactive were performed with 500,000 particles per cycle.

In Fig. 6.4.a, the converged 3D spatial distribution is illustrated. In this figure, the green and blue color are associated to nodes characterized by higher and lower power production respectively. The figure confirms that the solution follows the correct qualitative behavior. In fact, as expected, the power is higher for nodes with higher enrichment value and decreases along the axis due to the decrease in moderator density. Figs. 6.4.b-c, where

the axially and radially integrated power distribution are represented, allow to gain insights into the quantitative behavior of the solution. In particular, Fig. 6.4.b illustrates the radially-integrated power profile for a selected number of iterations computed from one of the independent simulations. It is noticeable that, despite being a three-dimensional problem, the convergence is faster than the one observed for the BWR unit-cell studied in Chapter 5. This is because only single-phase flow occurs in the channel and, therefore, the power distribution is less tilted. In other words, the power spatial distribution is closer to a cosine-shaped distribution. This observation is corroborated by Fig. 6.4.d, where the L2-norm of the relative residual of the power distribution is shown as a function of the non-linear iteration number. In fact the residual reaches 10^{-3} in 12 iterations rather than 37 as reported for the BWR unit-cell.

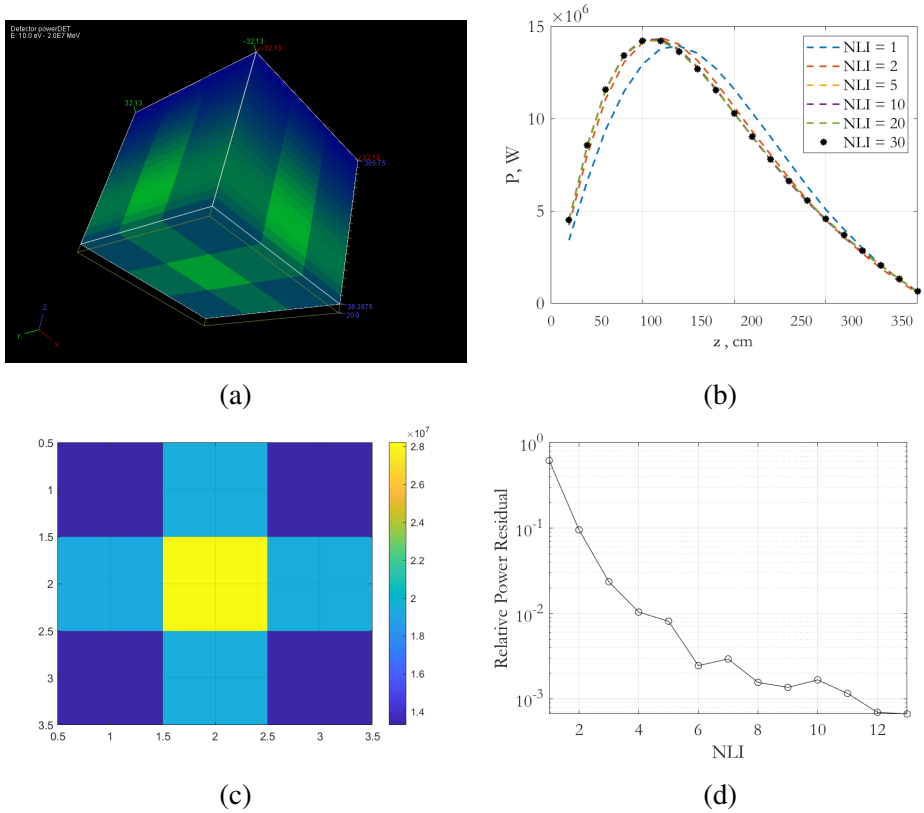

Figure 6.4: Reference Results for 290 ^{o}C as inlet temperature. (a) 3D view of the power distribution (b) Radially-integrated power distribution for selected number of iterations, (c) Axially-integrated power distribution, and (d) Relative power residual as a function of the number of iterations.

The channel-wise results for power, moderator temperature, fuel temperature, and moderator density are reported in Fig. 6.5. In the latter, the yellow curve with stars markers represents the central channel; the red curve with circle markers is associated to the channels A2-B1-B3-C2, while the blue curves with plus markers represents the spatial distribution in the corner channels, *i.e.*, assemblies A1-A3-C1-C3. From the smooth moderator temperature profile in Fig. 6.5.c, it is clear that only single-phase flow is present in the channels.

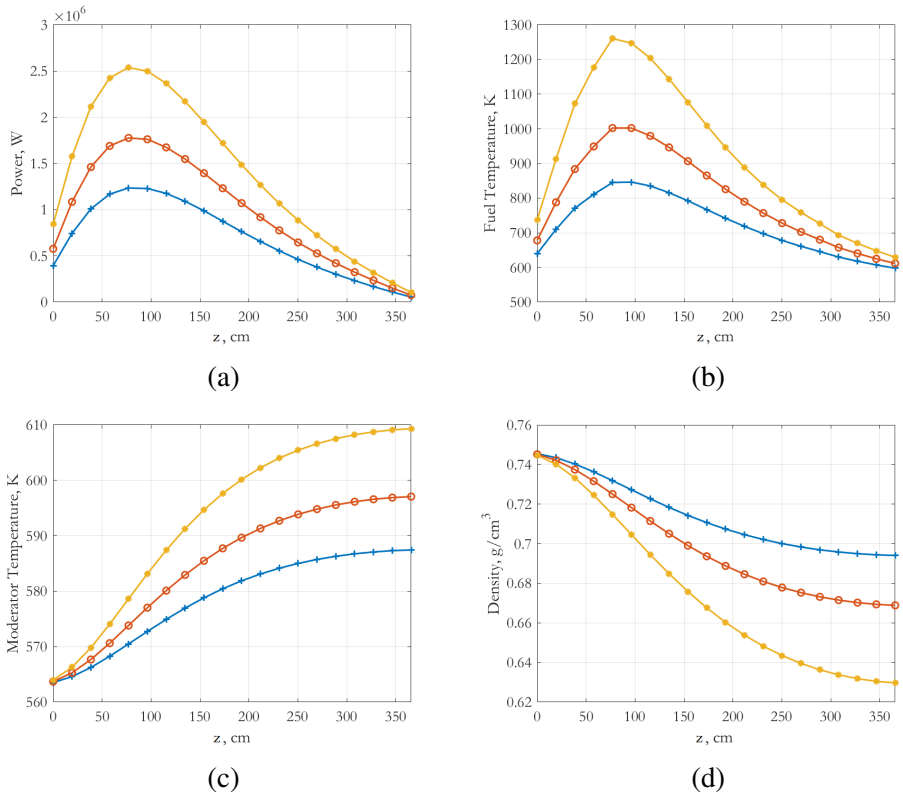

Figure 6.5: Reference Results for 290 ^oC as inlet temperature. Channel-by-channel spatial distribution for (a) power, (b) fuel temperature, (c) moderator temperature, and (d) moderator density. The yellow curves are associated to the central channel, the red curve to the peripheral channels in positions A2-B1-B3-C2, while the blue curve is associated to the corner channels-type.

6.4 Stand-alone predictor

In this section, the performance of the prediction block is analyzed in a stand-alone fashion, *i.e.*, the predicted power is not fed back into the MC-TH solver. The analysis is carried

out to demonstrate the ability of the transfer functions to capture the three-dimensional cross-sections distribution. Fig. 6.6 reports the transfer function remapping the compound variable $\vec{\xi} = \sqrt{\vec{T}_f} \circ \vec{\rho}$ onto the absorption macroscopic cross-section. The cross-sections were extracted from a MC simulation employing 400 criticality cycles per Picard iteration with 250,000 particles per cycle. The density and fuel temperature spatial profiles were computed using the Picard iteration sequence with no predictor feedback to simulate the integration of the acceleration block in the full sequence. It is evident that the transfer function does not present a simple structure as the one utilized for the simple channel. In particular, several local maxima and minima can be observed. The number of the latter does not match the number of channels.

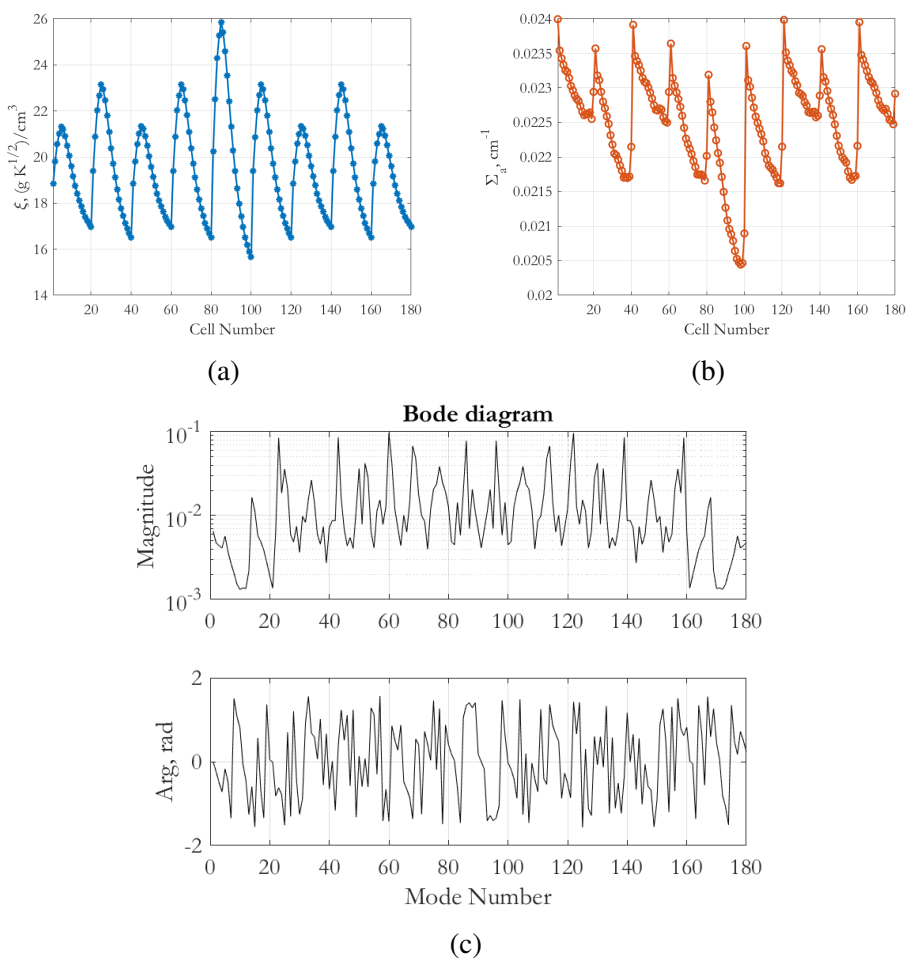

Figure 6.6: (a) Vectorized compound variable, (b) vectorized absorption cross-section, and (3) corresponding transfer function at NLI=2.

To demonstrate the ability of the GTF to predict the cross-section 3D distribution, the computed transfer functions are applied to the TH fields generated by the Picard iteration at the 2nd iteration to predict the value of the cross-sections' scalar field at the next iteration. This iteration was chosen because it presents the highest variation within the entire simulation. Fig. 6.7 reports the absorption cross-sections at iteration 2, denoted by 'Initial', the absorption cross-section at iteration 3 denoted by 'Target', and the predicted cross-section using the transfer function generated at the second iteration. It is noticeable that the prediction is able to capture the trend of the variation with an error of 1.54%. However, a more careful look shows that the noise of the iterates heavily affects the prediction when the variation is near zero as in the corner channel shown in Fig. 6.8.c. This phenomenon is also visible in the following iterates where the solution approaches the fixed point.

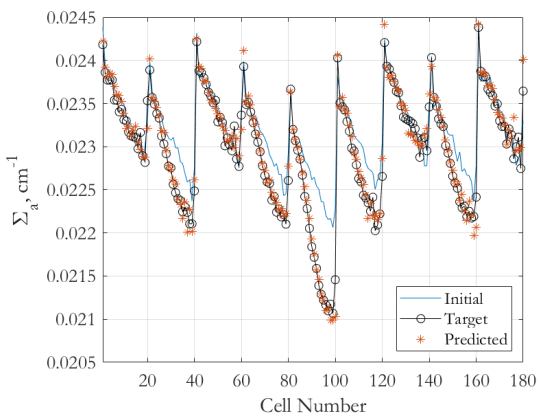

Figure 6.7: Prediction of the macroscopic absorption cross-section at the second iteration represent in vectorized form. The blue solid curve represents the initial guess, the red stars the predicted value, and the black line with circular markers the target distribution.

The predicted power profile in normalized form, *i.e.*, normalized to unity, is reported in Fig. 6.9. In the figure, the black dashed line represents the reference solution. It is noticeable that the predicted power profile tends to the reference. Moreover, we are able to predict it within 3% in few iterations.

The ability of the prediction to capture the inter-cycle variation is also confirmed by the prediction of the effective multiplication factor. In Fig. 6.10, the predicted k_{eff}, represented

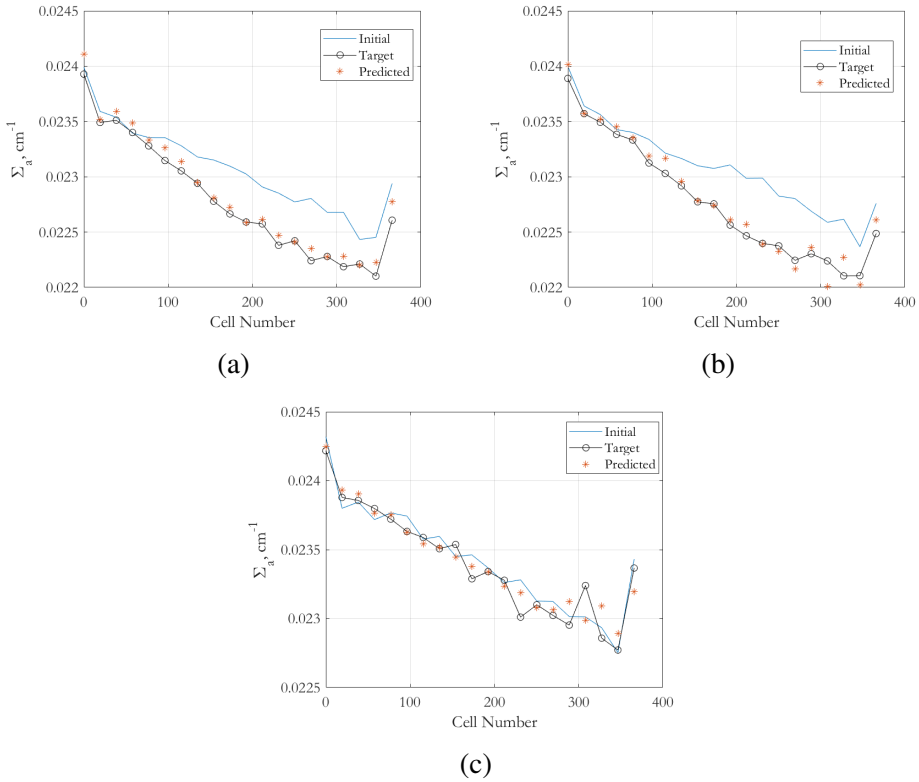

Figure 6.8: Channel-wise cross-section prediction at iteration 2.

by the red line with circular markers, is presented as a function of the number of Picard iterations and compared with the reference value, represented by the black line with star markers. It is noticeable that the prediction is able to estimate k_{eff} within a tenth of a pcm. This is due to the low inter-cycle variation that makes the linear approximation sufficient to capture the change in reactivity.

6.5 Integrated Sequence

In this section, the solutions obtained with accelerated PI and the standard algorithm are compared. The analysis is performed for different numbers of criticality cycles between two successive predictions, *i.e.*, 20 and 40. The number of criticality cycles was chosen based on the results of Section 5.35, where it was shown that a tighter coupling between MC and TH leads to higher speed-up factors. The results presented in this section are obtained using 1,000,000 particles per cycle and imposing a tolerance of 0.09% on the L2

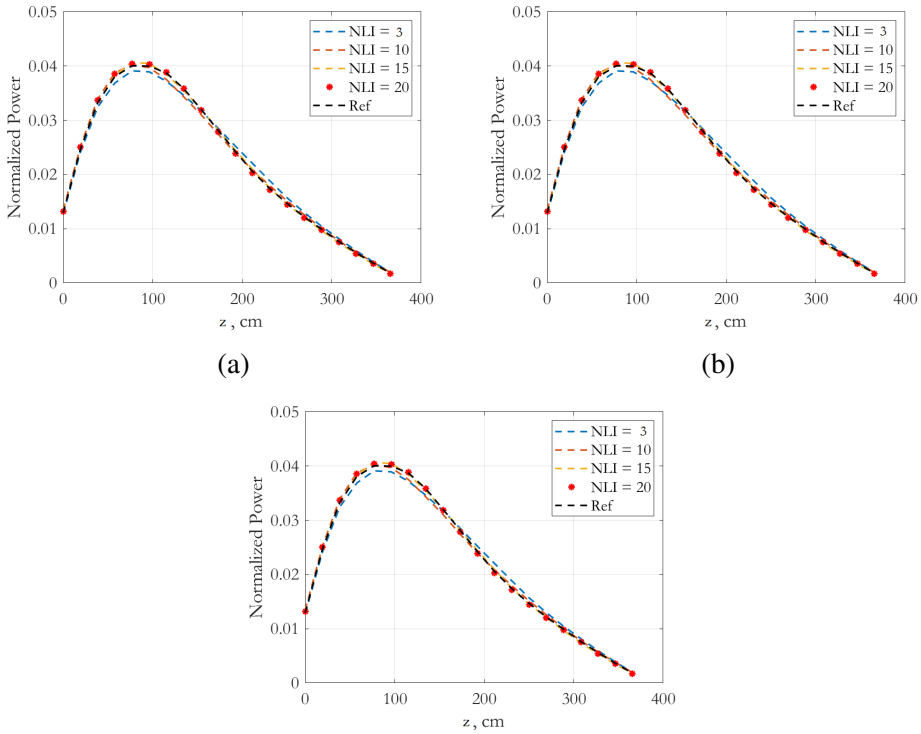

Figure 6.9: Channel-wise power prediction at selected number of iterations. The black dashed curve represents the reference solution. (a) Central channel, (b) Peripheral channel, (c) Corner Channel

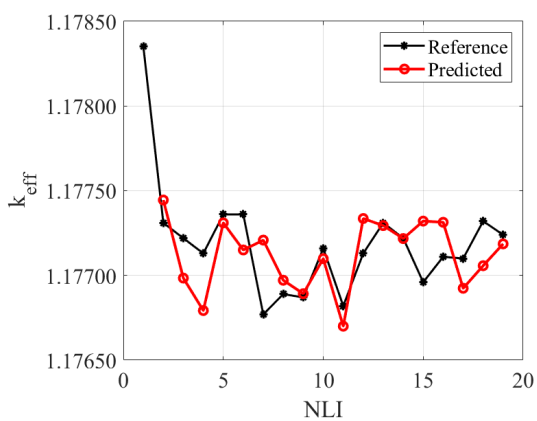

Figure 6.10: Effective multiplication factor prediction as a function of the number of Picard iteration or non-linear iterations (NLI).

norm of the power relative residual.

The remainder of the section is structured as follows. In Section 6.5.1, the residual is analyzed as a function of the Picard iteration number, while Section 6.5.2 reports the error

analysis aiming at quantifying the accuracy of the algorithm.

6.5.1 Residual Analysis

The L2 norm of the power relative residual is reported as a function of the number of criticality cycles in Fig. 6.11. As in Section 5.3.5, each curve is obtained from a different simulation. The black solid curve is computed by using the standard algorithm, where converged power iterates are utilized to initialize the next Picard iteration. The convergence is ensured by utilizing 800 criticality cycles, of which 400 are inactive and obtaining a maximum standard deviation of 0.5% on the nodal power tallies. The convergence is achieved within 13 Picard iterations, or, equivalently, 10,400 criticality cycles as shown in Fig. 6.11. The blue curves and red curves are computed by performing 20 and 40 cycles at each Picard iteration respectively, and using the same amount of particles per cycle, *i.e.*, one million neutrons. The dashed lines are associated to the standard algorithm, while the solid curves are computed from the accelerated PI. It is noticeable that in this case, the use of the acceleration does not systematically lead to a faster convergence in terms of relative residual. In particular, it can be noticed that the total number of criticality cycles to convergence is mainly determined by the tightness of the TH and MC solver coupling, *i.e.*, the curves n and $n+GTF$ converge after about the same number of iterations. However, as for the BWR unit cell, a more frequent data exchange between neutronics and TH determines a quicker convergence to the fixed point.

6.5.2 Error Analysis

While Fig. 6.11 may seem to suggest a negligible speed-up, we can clearly grasp the benefits of using the GTF-based acceleration when the accuracy of the overall scheme is considered. In fact, as noticed in Section. 5.3.2, using less criticality cycles in conjunction with the Robbins-Monro stochastic approximation can lead the sequence of iterates to an incorrect fixed point, *i.e.*, power distribution. Fig. 6.12, reporting the converged power distribution,

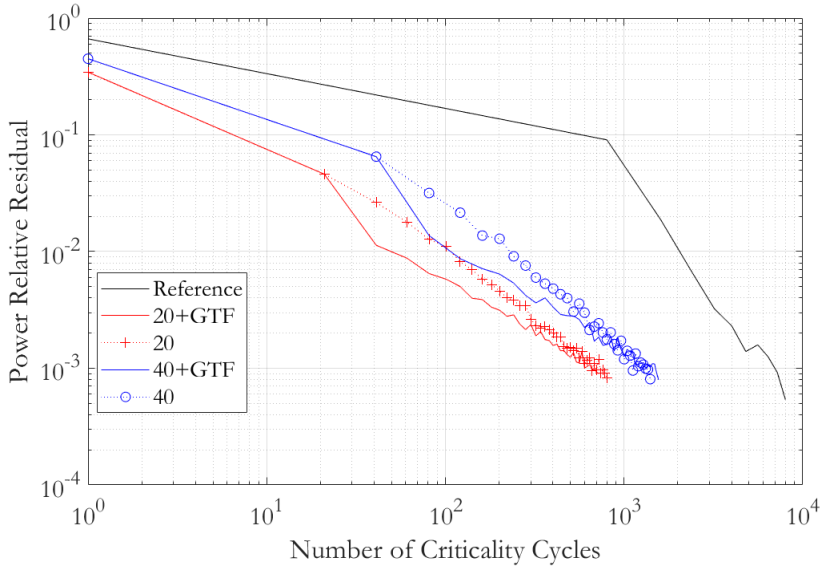

Figure 6.11: Residual as a function of number of criticality cycles.

clearly shows this phenomenon. It is noticeable that, as for the mono-dimensional case, the result obtained without employing the GTF-based acceleration heavily differ from the reference solution. In Fig. 6.12, the dashed red and blue curve are associated to the non-accelerated simulation with 20 and 40 criticality cycles per Picard iteration respectively. The latter have an $|e|_{\vec{P}}$ from the reference solution, *i.e.*, black solid line, of 27.201% and 10.711% respectively. This convergence issue does not affect the curves calculated with the GTF-accelerated algorithm represented by the solid red and blue line. In fact, the $|e|_{\vec{P}}$ is 0.54% for the accelerated scheme with 20 criticality cycles per Picard iteration and 0.85% for the one employing 40 cycles. This is because the prediction block relies on the cross-sections and the fission matrix elements. Their definition as ratios brings about a systematic cancellation of error that leads to a faster convergence when compared to the one of the power profile. Therefore, the prediction causes the iterates to drift towards a profile closer to the correct fixed point.

Fig. 6.13 clearly shows the different convergence pattern for simulations employing the GTF-based acceleration and the standard algorithm with Robbins-Monro approximation when non-converged iterates are employed. In fact, the non-accelerated scheme clearly

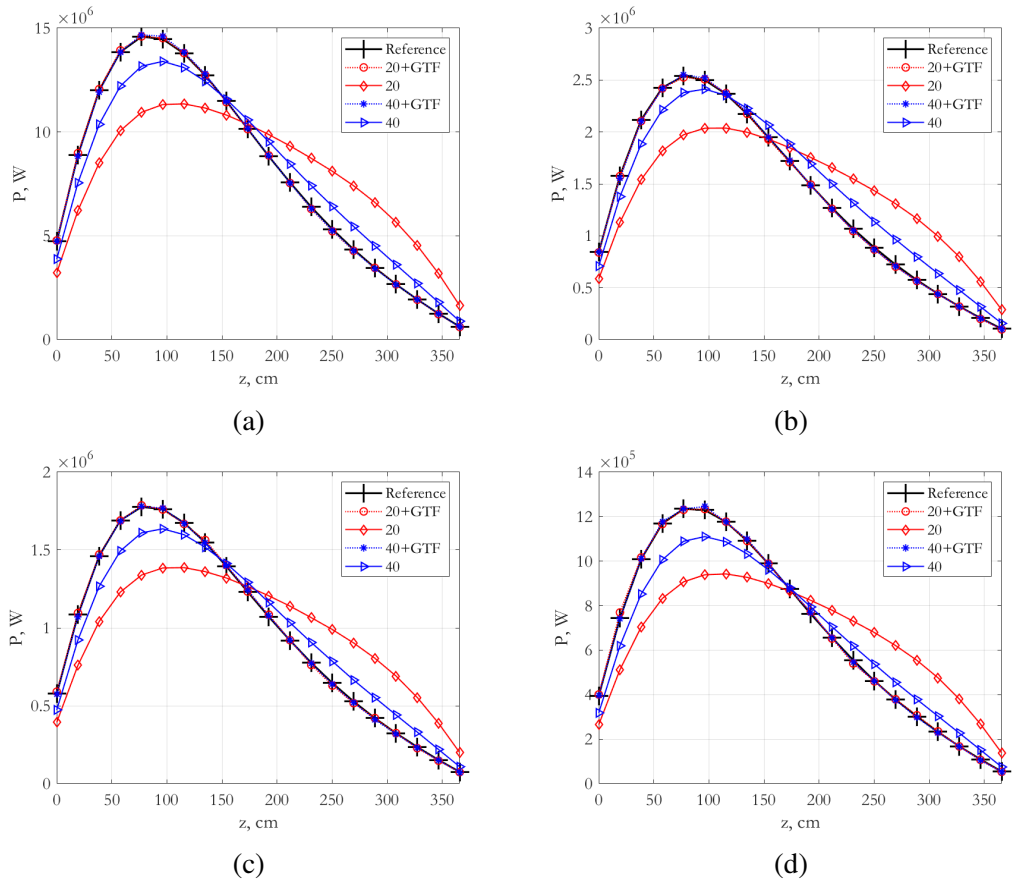

Figure 6.12: (a) Converged radially-integrated power spatial profile (b) power profile in central channel (B2), (c) power profile in peripheral channel (A2-B1-B3-C2), (d) power profile in corner channel(A1-A3-C1-C3), for different number of criticality cycles (number associated to each curve). The dotted lines are associated to simulations employing the GTF acceleration.

converges to a distorted spatial shape. The distortion is due to the non-sufficient number of cycles that determines the inability of the neutrons to migrate far enough from their birth site, effectively covering the full geometry. In other words, the birth and absorption site of the neutrons are spatially correlated due to the low number of cycles and the insufficient statistics.

Table 6.2 reports the metrics for the examined case. It is noticeable that both results computed with the accelerated algorithms agree within 1% $|e|_{\vec{P}}$ with the reference solution. The error is even lower for the TH spatial profiles, *i.e.*, 0.032% for the density profile and 0.198% for the fuel temperature in the 20 criticality-cycles case.

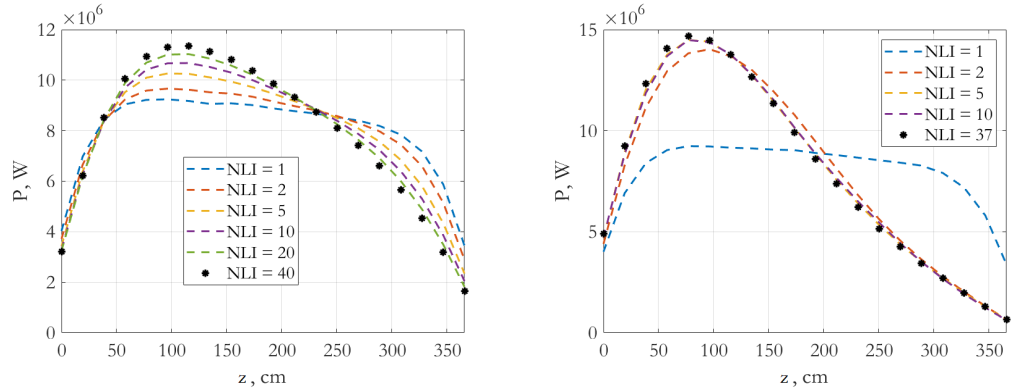

(a) (b)

Figure 6.13: Radially integrated power profile for selected number of Picard iterations, *i.e.*, non-linear iterations (NLI), for simulations with 20 criticality cycles per Picard iteration. (a) In absence of GTF-based acceleration. (b) With GTF acceleration.

Table 6.2: FOM and speedup for GTF+PI compared to standard PI scheme.

Simulation Parameter	**20+GTF**	**20**	**40+GTF**	**40**
$\lvert e\rvert^{a}_{\vec{P}}$, %	0.544	27.199	0.605	10.739
$\lvert e\rvert^{r}_{\vec{P}}$, %	0.310	2.445	0.243	2.662
$\lvert e\rvert_{\vec{P}}$, %	0.551	27.201	0.635	10.711
$\lvert e\rvert_{\vec{T}_f}$, %	0.198	9.079	0.237	3.594
$\lvert e\rvert_{\vec{T}_m}$, %	0.015	0.493	0.010	0.192
$\lvert e\rvert_{\vec{\rho}_m}$, %	0.032	0.960	0.021	0.361
FOM_f	5.50	0.500	2.81	0.256

6.6 Sensitivity to inlet coolant temperature

In this section, the mini-core is solved with 315°C as inlet coolant temperature. The problem was chosen to demonstrate the ability of the accelerated Picard iteration to capture the power variation in a three-dimensional geometrical settings when two-phase flow occurs.

The remainder of the section is structured as follows. Section 6.6.1 reports the reference results for the coupled calculation, while the problem is solved with the GTF-based accelerated Picard iteration algorithm in Section 6.6.2.

6.6.1 Reference Results

The reference results were generated by averaging the spatial distributions computed from six independent runs, each employing 500,000 particles for 800 criticality cycles of which 400 are active. This resulted in a root mean square standard deviation of 5 pcm for the effective multiplication factor and a maximum standard deviation of 0.6% on the power tallies at each Picard iteration. The convergence tolerance for the L2 norm of the power relative residual was set to 0.9%.

Fig. 6.14.a shows the three-dimensional distribution for the problem. Fig. 6.14.b-c display the radially and axially integrated power profile respectively, while the power relative residual is represented as a function of the number of Picard iterations in Fig. 6.14.d.

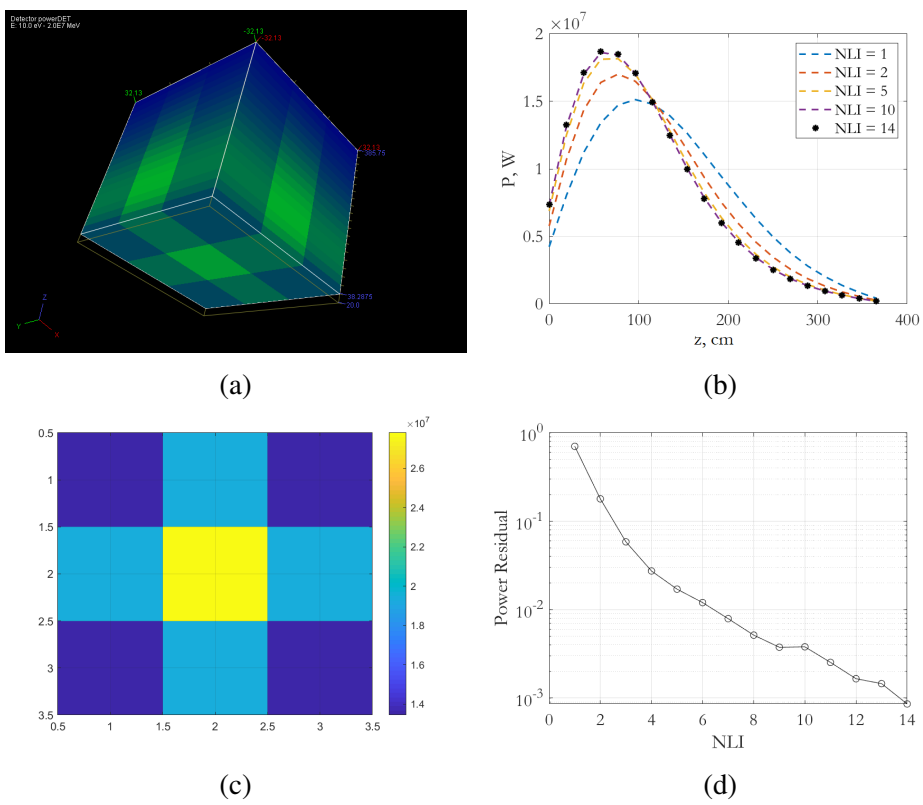

Figure 6.14: Reference results for 315°C as inlet temperature. (a) 3D view of the power distribution (b) Radially-integrated power distribution for selected number of iterations, (c) Axially-integrated power distribution, and (d) Relative power residual as a function of the number of iterations.

Fig. 6.15 displays the channel-wise results for the problem. It is noticeable that the higher inlet coolant temperature affects the flow regime in the central channel, where, in fact, boiling is experienced. This is evident from the near-flat moderator temperature profile from 125 cm to the top of the active geometry in Fig. 6.15. The slight decrease in temperature is due to the pressure drop along the channel.

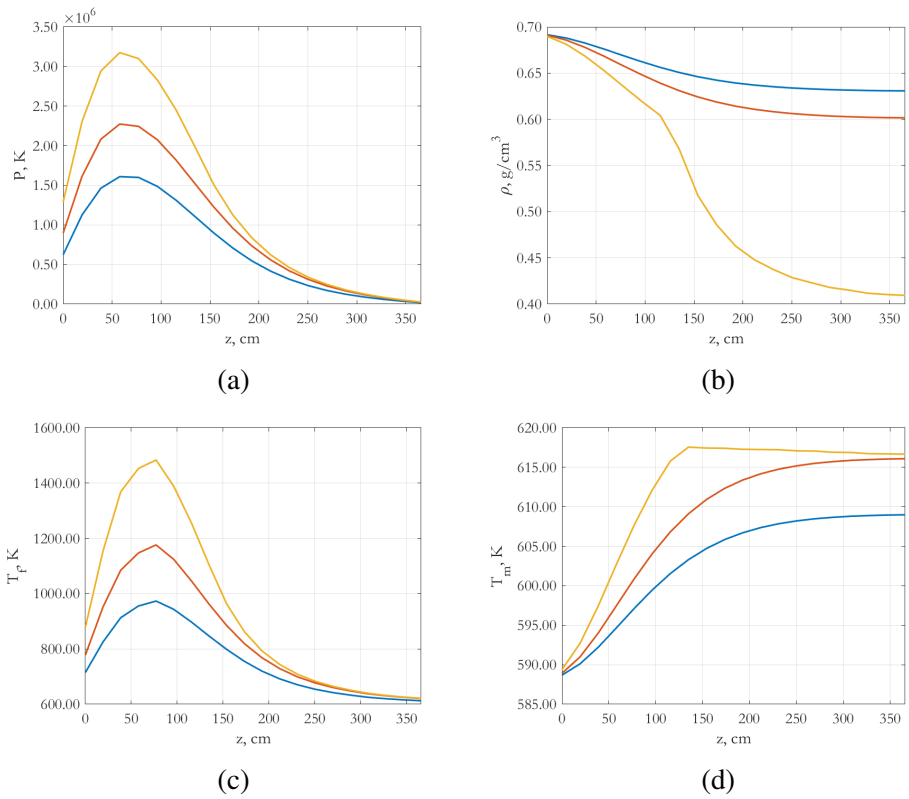

Figure 6.15: Channel-wise reference results for 315°C as inlet temperature. (a) Power distribution (b) Moderator density, (c) Fuel temperature, and (d) Moderator temperature. The yellow curves are associated to the central channel, the red curve to the peripheral channels in positions A2-B1-B3-C2, while the blue curve is associated to the corner channels-type.

6.6.2 Integrated Sequence

Fig. 6.16 reports the L2 norm of the relative power residual as a function of the criticality cycles. As for Fig. 6.11, each curve is associated to a different simulation. The number associated to each curve refers to the amount of criticality cycles per Picard iteration, while 'GTF' denotes the curves generated by deploying the GTF-based acceleration.

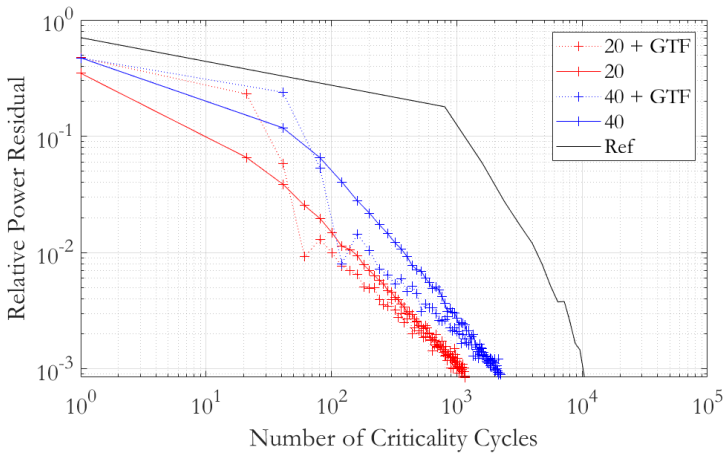

Figure 6.16: Residual as a function of number of criticality cycles.

From Fig. 6.16, it can be observed that the use of the GTF-based acceleration leads to a quicker convergence within 1% relative residual. For instance, considering the $20 + GTF$ curve, 4 Picard iterations are needed to achieve this precision level. A number of iterations equal to 11 is needed for the non-accelerated simulation to obtain the same precision level. The convergence to the tolerance is mainly determined by the degree of coupling between MC and TH solver as noticed in Section 6.5. This could be due to the statistical error associated to the transfer functions, and, therefore, the predicted cross-sections when bigger phase-space needs to be sampled. Further analysis and techniques to propagate the uncertainty in the prediction calculations block will be considered in the future to investigate this phenomenon.

Despite allowing to measure the algorithm's precision, the relative residual does not measure its accuracy. Fig. 6.17 reports the converged power profile for the simulations associated to the curves in Fig. 6.16. It is noticeable that, as for the mono-dimensional case in Section 5.3.3 and the results illustrated in Fig. 6.12, the use of the PI with non-converged MC iterations does not allow to converge to the reference solution, denoted by the black curve. This phenomenon does not occur in simulations employing the GTF-based acceleration.

The convergence pattern is clear in Fig. 6.18, where the radially-integrated power pro-

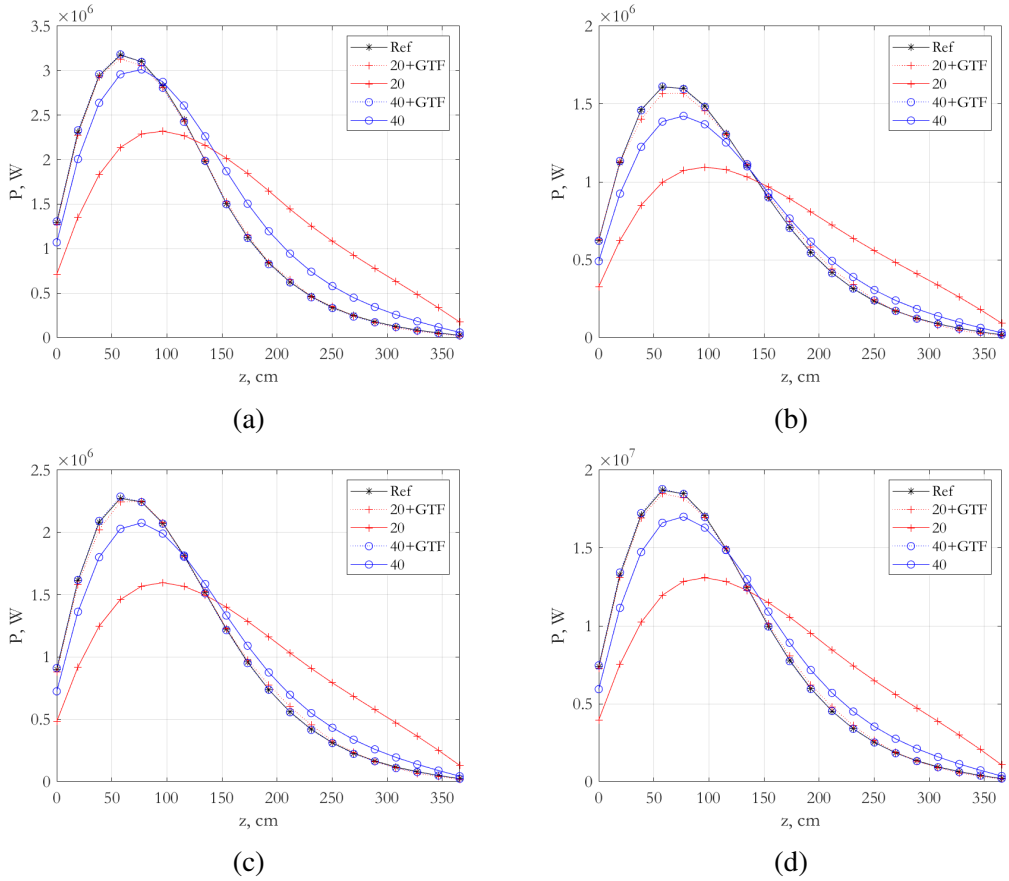

Figure 6.17: (a) Converged radially-integrated power spatial profile (b) power profile in central channel (B2), (c) power profile in peripheral channel (A2-B1-B3-C2), (d) power profile in corner channel (A1-A3-C1-C3), for different number of criticality cycles (number associated to each curve). The dotted curves are associated to simulations employing the GTF acceleration.

file is plotted for selected number of iterations. While the power profile generated with the non-accelerated algorithm smoothly converges to an incorrect fixed point, the GTF-accelerated solution quickly converges within a few iterations to the correct solution within a few percent. A synopsis of the accuracy metrics is provided in Table 6.3. Considering the case '20+GTF', it is noticeable that the L2 relative error on the power is 1.53% for the radially integrated power and 0.61% for the axially integrated power profile. The L2 error is recorded in the central channel, where the difference from the reference solution is 2.68%. The error associated to the temperature and density profile is even lower, with 0.25% on the density, 0.018% on the moderator temperature, and 0.531% on the fuel temperature.

Using the unaccelerated Picard iteration with the Robbins-Monro relaxation does not lead to a net speed up, *i.e.*, FOM less than unity, in both the cases considered in this analysis, *i.e.*, 20 and 40 criticality cycles.

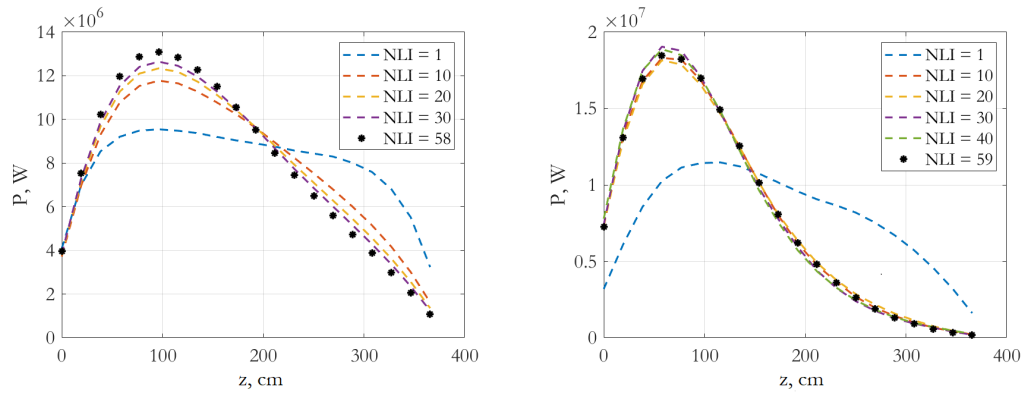

(a) (b)

Figure 6.18: Radially integrated power profile for selected number of Picard iterations, *i.e.*, non-linear iterations (NLI), for simulations with 20 criticality cycles per Picard iteration. (a) In absence of GTF-based acceleration. (b) With GTF acceleration.

Table 6.3: FOM and speedup for GTF+PI compared to standard PI scheme.

Simulation Parameter	**20+GTF**	**20**	**40+GTF**	**40**
$\lvert e\rvert^a_{\vec{P}}$, %	1.533	37.712	0.584	11.670
$\lvert e\rvert^r_{\vec{P}}$, %	0.610	4.152	0.197	4.129
$\lvert e\rvert_{\vec{P}}$, %	1.516	37.815	0.649	11.697
$\lvert e\rvert_{\vec{T}_f}$, %	0.531	13.911	0.301	4.344
$\lvert e\rvert_{\vec{T}_m}$, %	0.018	0.538	0.009	0.172
$\lvert e\rvert_{\vec{\rho}_m}$, %	0.247	2.887	0.092	1.198
FOM_f	4.138	0.700	2.222	0.740

6.7 Summary

In this chapter, the GTF-based acceleration was applied to a three-dimensional mini-core problem derived from a prototypical PWR design. The problem was solved in correspondence of two different inlet coolant temperatures to study the ability of the algorithm to capture the power variation both in the case of single-phase and two-phase flow.

It was shown that the GTF-based acceleration can accelerate the convergence to the

fixed point in both cases with error below 1% in all TH scalar fields and within few percent for the power profile. The performance of the accelerated algorithm were both superior to the standard procedure, in which the converged power profile is utilized to initialize the next Picard iteration, and to the Picard iteration with non-converged iterations.

CHAPTER 7
SUMMARY AND CONCLUSIONS

The GTF-based acceleration, a new acceleration methodology for coupled Monte Carlo-Thermal Hydraulics calculations, was introduced in this thesis. The acceleration relies on a novel technique for the computation of the cross-sections spatial distribution due to variations in the TH scalar fields. The latter technique is a novel contribution that relies on the definition of generalized transfer functions to calculate the cross-sections given a change in density and temperature profiles. The method has many desirable characteristics. First, it allows to capture non-local effects contrarily to current methods for cross-sections interpolation/reconstruction. Second, the GTF, despite being here applied to MC codes, is general and may be used for deterministic methods as well. Finally, the method is geometrically agnostic. Thus, it can be utilized to study non-traditional geometries, *i.e.*, not square or hexagonal, that characterize many advanced nuclear reactors' concepts. The performance of the method were tested against both mono-dimensional and three-dimensional problems with full TH feedback, showing a net speedup with respect to the Picard iteration method, that is the standard procedure utilized in MC-TH calculations nuclear reactor analysis. In this thesis, only LWR-based problems with Cartesian geometries were utilized to test the GTF. However, our definition of transfer function, based on the vectorization of the 3D distribution, does not account for the actual topology and geometry of the system. Therefore, the tests performed in this dissertation were deemed sufficient to demonstrate the ability of the GTF-based acceleration to treat general geometries. Studies on the application of the GTF-based acceleration to reactor designs characterized by hexagonal assemblies will be performed to further corroborate this point in future work. Follows a detailed account of the three novel contributions provided within this dissertations.

First, a novel methodology for the calculation of macroscopic cross-sections due to

spatial TH variations, was formulated from a general Petrov-Galerkin framework. This technique, called generalized transfer function (GTF) theory, allows to capture non-local effects that are neglected by standard cross-sections' generation techniques. In particular, the single shape approximation of the GTF was defined. The latter enabled us to obtain on-the-fly estimations of the mono-energetic macroscopic cross-sections. The theory was formulated to cover multiple feedback mechanisms and the theoretical claims were supported with numerical results. Preliminary results were obtained for a BWR unit-cell with realistic density profile and heterogeneous fuel composition, showing that the single-shape approximation of the GTF can to capture the cross-sections' variation within 2%, even at the boundary of the domain, where higher levels of stochastic noise are present.

Second, the GTF was leveraged to define an acceleration scheme for coupled MC-TH calculations in conjunction with a perturbation-based power prediction model based on the use of the fission matrix modes. This technique does not rely on problem-specific training, therefore allowing to efficiently predict the cross-sections and the power at the next criticality cycle on-the-fly. Additionally, a MATLAB code has been developed to perform 3D coupled MC-TH coupled calculations, employing Serpent and THERMO as single-physics code. The code can be easily modified and used for future research endeavors.

Third, the GTF-based acceleration was tested against mono-dimensional (1D) and three-dimensional (3D) LWR-based problems. It was shown that the accelerated consistently outperformed the standard algorithm. In the 1D case, a speed up between 2.1 and 12.4 over the standard Picard iteration was observed, while the speed up was between 2.2 and 5.5 in the 3D case. Higher speedups were obtained for a tighter coupling between TH and MC solver, *i.e.*, lower number of criticality cycles per Picard iteration. In terms of accuracy, a relative error below 3% from the reference power and lower than 1.9% from the reference TH spatial distributions were obtained in the 1D case. Better performances were observed for the 3D cases, with the L2-norm of the relative error below 1.5% for the power distribution and 0.5% for the TH spatial distributions. In the best case, *i.e.*, PWR-based mini-core

problem evaluated at a coolant inlet temperature of 290 ^oC with 20 criticality cycles per Picard iteration, we obtained an L2-norm of the relative power error equal to 0.544%. The corresponding error for the fuel temperature and moderator density were 0.2% and 0.032%, respectively.

CHAPTER 8

FUTURE WORK

In this section, potential directions for future work are provided.

An alternative basis set: wavelets

In this thesis, the discrete Fourier basis was chosen to expand the cross-section, the TH scalar fields and, therefore, to define the GTF in its single-shape approximation. The choice was made for two reasons. First, the computation of the expansion coefficients is made efficient through the use of the standard Fast Fourier Transform (FFT) algorithms. Secondly, the introduction of the Fourier transform enables to leverage common signal processing techniques for denoising cross-sections generated with MC codes. However, it is well-known that the DFT should be applied to periodic, unlimited signals, not for space-limited, non-periodic shapes. In order to have a basis set more consistent with the problem's characteristics, it may be a better choice to utilize a wavelet basis [61]. The latter is a family of orthonormal basis sets that is domain-limited by construction and can be utilized for non-periodic signals analysis. Additionally, well established techniques for wavelets-based denoising exist and fast-wavelet transform algorithms are implemented in standard software packages like MATLAB.

Error and uncertainty propagation

When using a stochastic solver, a standard deviation, *i.e.*, uncertainty, is associated to the calculations' results. In this thesis, it was chosen not to propagate this uncertainty trough the prediction block. This was done to mitigate the computational requirement associated to the calculation of the results. In fact, the latter would have been much higher if direct error propagation techniques had been used. However, the accurate quantification of uncertainty is crucial if the GTF-based acceleration technique is envisioned to be used in the framework of Verification & Validation efforts. A possible manner to estimate the pre-

dicted power distribution's uncertainty consists in implementing automatic differentiation algorithm [62]. The latter would allow to compute the Jacobian associated to the predictor with minimum effort.

Non-LWR benchmark problems

In this work, LWR-based test problems were used to evaluate the performance of the accelerated Picard iteration method. In order to provide a more comprehensive overview of the method's strengths and limitations, it will be necessary to test the algorithm against problems based on alternative nuclear reactor designs. This is because one of the approximations at the core of this GTF-based approximation is the use of the compound variable to describe the dependency from fuel temperature and density scalar field. Its definition is based on the problems' physics, not derived from a generally-valid equation. Therefore, extended testing is necessary to gain a better sense of the validity of this approximation. The authors are currently working on applying the GTF-based acceleration technique to a full-core nuclear thermal propulsion simulation.

Denoising input and output signals

In Chapter 3, it was noticed that the statistics can undermine the quality of the results, by exciting higher components of the Fourier spectrum. A potential line of future research could be exploring denoising techniques to mitigate this effect. In fact, a plethora of DFT-based and wavelet-based denoising techniques exist that could be utilized for this purpose [47]. An automatic denoising of the Picard iterates could be used to eliminate or attenuate the stochastic noise and further increase the convergence rate of the sequence to the fixed point, therefore leading to higher speedup factor for fixed statistics.

Alternative Power Solver

In this work, we utilized a perturbation-based formula to predict the power profile for given variations of the nodal macroscopic cross-sections. The formula leverages the fission matrix eigentriplets, *i.e.*, forward eigenmodes, eigenvalues, and adjoint eigenmodes, to perform the power prediction. However, the calculation of the fission matrix could be

memory-wise very expensive for a full-core calculation. In fact, a fine mesh is needed to obtain a meaningful estimation of the modes. This is because the modes of the fission matrix tend to the ones of the continuous operator only in the limit of null nodes' volume. In order to decrease the method's computational requirement, alternative power predictor can be used. Among these, is the use of diffusion solvers or one-group Monte Carlo solvers. The use of diffusion codes as alternative reduced order neutronic solvers is under investigation.

Full-GTF for cross-sections generation

Despite the general definition of the GTF, given in Chapter 3, the single shape approximation was here utilized. Besides it, only the utilization of the GTF for the purpose of accelerating MC-TH calculations was explored. An alternative line of research would consist in using the GTF to correct the macroscopic cross-sections for intra-nodal effects, *e.g.*, heterogeneous temperature distribution within nodes, or inter-nodal effects, *e.g.*, temperature and density distribution in neighboring assemblies.

Appendices

APPENDIX A

FISSION MATRIX DEFINITION

The LTE, *i.e.*, Eq. 2.1, can be formally solved by computing the Green's function G associated to the loss operator $\mathcal{L}$:

$$\begin{cases} \mathcal{L}G = \delta(\vec{r} - \vec{r}_0)\delta(E - E_0)\delta(\hat{\Omega} - \hat{\Omega}_0) \\ G(\vec{r}_\partial, E, \hat{\Omega}_-) = 0. \end{cases} \tag{A.1}$$

In Eq. A.1, the symbol δ denotes the Dirac function, while the subscript 0 refers to the source phase-space location. Strictly following the derivation in Refs. [63, 64], the exploitation of the LTE linearity leads to the following equation for the angular flux:

$$\psi(\vec{r}, E, \hat{\Omega}) = \frac{1}{k} \int d^3 r_0 \int d\Omega_0 \int dE_0 \, G(\vec{r}_0, E_0, \hat{\Omega}_0 \to \vec{r}, E, \hat{\Omega}) \, \frac{\chi(\vec{r}_0, E_0)}{4\pi} \mathcal{M}\psi(\vec{r}_0, E_0, \hat{\Omega}_0). \tag{A.2}$$

The integrals are computed over the whole phase-space domain. After defining the fission neutron source as $S(\vec{r}) = \mathcal{M}\psi(\vec{r}, E, \hat{\Omega})$, multiplying Eq. A.2 by $\nu\sigma_f(\vec{r}, E)$, and integrating over energy and angle, the eigenvalue equation for the fission neutron source is obtained:

$$S(\vec{r}) = \frac{1}{k} \int d^3 r_0 \, \mathcal{K}(\vec{r}_0 \to \vec{r}) \, S(\vec{r}_0). \tag{A.3}$$

The kernel operator $\mathcal{K}$ maps the fission source from position $\vec{r}_0$ to position $\vec{r}$. The average value between two finite cells V_i and V_j is obtained by discretizing the whole domain in non-overlapping cells V_j, such that $V = \bigcup_{j=1}^{N} V_j$. The integration of Eq. A.3 in

V_i leads to the definition of the spectral problem for the discretized fission source:

$$S_i = \frac{1}{k} \sum_{j \in V} K_{j \to i} S_j. \tag{A.4}$$

In Eq. A.4, S_i and S_j are the average value of the fission source in cells V_i and V_j respectively. The matrix **K**, called Fission Matrix (FM), is the collection of the elements $K_{j \to i}$ defined by the formula:

$$K_{j \to i} = \frac{\int_{V_i} d^3r \int_{V_j} d^3r_0 \, \mathcal{K}(\vec{r}_0 \to \vec{r}) \, S(\vec{r}_0)}{\int_{V_j} d^3r_0 \, S(\vec{r}_0)}. \tag{A.5}$$

The FM element $K_{j \to i}$ represents the expected number of fission neutrons born in the production site i due to the fission neutrons born in the emission site j at the previous generation. The convolution of the FM with the fission source gives the next generation neutron fission distribution. The repeated convolution, *i.e.*, power iteration, leads to the asymptotic distribution of the fission neutron population $\vec{S} = \{S_i\}_{i=0,\ldots,N}$, and the corresponding multiplication factor k .

The mode of the fission matrix can be computed by rewriting Eq. A.4 in matrix form and noticing that it is valid for any eigenpair $\left(k_n, \vec{S}^n\right)$.

$$\mathbf{K}\vec{S}_n = k_n \vec{S}_n. \tag{A.6}$$

The adjoint problem can be defined as:

$$\mathbf{K}^T \vec{S}_n^\dagger = k_n S_n^\dagger, \tag{A.7}$$

where the superscript T denotes the matrix transpose and † the adjoint. It is noticeable that for the cells volume tending to zero, the modes of the fission matrix coincide with the ones of the original transport operator as evident from Eq. A.5.

APPENDIX B

DERIVATION OF FIRST ORDER PERTURBATION FORMULAS

Let consider the LTE written in operator form, as expressed in Eq. 2.13:

$$\mathcal{L}\ \psi_n(\vec{r}, E, \hat{\Omega}) = \frac{1}{k_n}\mathcal{F}\ \psi_n(\vec{r}, E, \hat{\Omega}), \tag{B.1}$$

where $\mathcal{F}$ is the product of the multiplication operator $\mathcal{M}$ and the fission kernel $\frac{\chi(\vec{r},E)}{4\pi}$. The corresponding adjoint problem is:

$$\mathcal{L}^\dagger\ \psi_n^\dagger(\vec{r}, E, \hat{\Omega}) = \frac{1}{k_n}\mathcal{F}^\dagger\ \psi_n^\dagger(\vec{r}, E, \hat{\Omega}), \tag{B.2}$$

The definition of the adjoint operators can be found in Ref. [22]. The solution ψ_0 of the adjoint equation, *i.e.*, dominant eigenmode, is usually denoted as importance function or adjoint flux. Both equations admit infinite solutions $\{\psi_n\}_{n=0,\ldots}$, that respect the bi-orthogonality relation:

$$\langle \psi_n^\dagger\ ,\ \mathcal{F}\psi_m \rangle = \delta_{n,m}, \tag{B.3}$$

where the angle brackets indicate the inner product, and $\delta_{n,m}$ is the Kronecker delta.

B.1 Eigenvalue perturbation

If we insert an arbitrary perturbation in Eq. B.1, the following equation is obtained:

$$\mathcal{L}'\ \psi_0'(\vec{r}, E, \hat{\Omega}) = \frac{1}{k_0'}\mathcal{F}'\ \psi_0'(\vec{r}, E, \hat{\Omega}), \tag{B.4}$$

where the prime denotes a perturbed quantity. Equivalently, we can express the new

system of equation as a perturbation of the original state:

$$\begin{aligned}\mathcal{L}\ \psi_0(\vec{r},E,\hat{\Omega})+\delta\mathcal{L}\ \psi_0(\vec{r},E,\hat{\Omega})+\mathcal{L}\ \delta\psi_0(\vec{r},E,\hat{\Omega}) &= \lambda_0\ \mathcal{F}\ \psi_0(\vec{r},E,\hat{\Omega}) \\ &= \delta\lambda_0\mathcal{F}\ \psi_0(\vec{r},E,\hat{\Omega})+\lambda\delta\mathcal{F}\ \psi_0(\vec{r},E,\hat{\Omega})+\lambda_0\mathcal{F}\ \delta\psi_0(\vec{r},E,\hat{\Omega}),\end{aligned} \tag{B.5}$$

where λ_0 is the inverse of the dominant eigenvalue k_0. Using Eq. B.1, multiplying by the adjoint flux $\psi_0^\dagger$, and taking the inner product, we obtain:

$$\begin{aligned}&\langle\psi_0^\dagger,\ \delta\mathcal{L}\ \psi_0(\vec{r},E,\hat{\Omega})\rangle+\langle\psi_0^\dagger,\ \mathcal{L}\ \delta\psi_0(\vec{r},E,\hat{\Omega})\rangle = \\ &= \delta\lambda_0\langle\psi_0^\dagger,\ \mathcal{F}\ \psi_0(\vec{r},E,\hat{\Omega})\rangle+\lambda_0\langle\psi_0^\dagger,\ \delta\mathcal{F}\ \psi_0(\vec{r},E,\hat{\Omega})\rangle \\ &+\langle\psi_0^\dagger,\ \lambda_0\mathcal{F}\ \delta\psi_0(\vec{r},E,\hat{\Omega})\rangle,\end{aligned} \tag{B.6}$$

The use of Eq. B.3 and the recast of the terms leads to the following expression for the inverse of the dominant eigenvalue, *i.e.*, multiplication factor:

$$\delta\lambda_0 = \frac{\langle\psi_0^\dagger,\ \delta\mathcal{L}\ \psi_0(\vec{r},E,\hat{\Omega})\rangle-\lambda_0\langle\psi_0^\dagger,\ \delta\mathcal{F}\ \psi_0(\vec{r},E,\hat{\Omega})\rangle}{\langle\psi_0^\dagger,\ \mathcal{F}\ \psi_0(\vec{r},E,\hat{\Omega})\rangle}. \tag{B.7}$$

B.2 Dominant eigenmode perturbation

The perturbed eigenmode can be found by using the superposition of effects.

$$\delta\psi_0(\vec{r},E,\hat{\Omega}) = \sum_{m=0}^{M} a_m\psi_m(\vec{r},E,\hat{\Omega}), \tag{B.8}$$

where M is finite if the core is discretized in a finite number of cells and infinite if a continuous phase-space representation is used. The expansion coefficients can be found by

substituting Eq. B.8 into Eq. B.5 to obtain:

$$\begin{aligned}
&\delta\mathcal{L}\ \psi_0(\vec{r},E,\hat{\Omega}) + \mathcal{L}\ \sum_{m=0}^{M} a_m\psi_m(\vec{r},E,\hat{\Omega}) = \lambda_0\ \mathcal{F}\ \psi_0(\vec{r},E,\hat{\Omega}) \\
&= \delta\lambda_0\mathcal{F}\ \psi_0(\vec{r},E,\hat{\Omega}) + \lambda_0\delta\mathcal{F}\ \psi_0(\vec{r},E,\hat{\Omega}) + \lambda_0\mathcal{F}\ \sum_{m=0}^{M} a_m\psi_m(\vec{r},E,\hat{\Omega}),
\end{aligned} \tag{B.9}$$

Multiplying by $\psi_n^\dagger$, taking the inner product, and exploiting the bi-orthogonality property, we obtain the following equation for the mth coefficient:

$$a_m = \frac{\langle\psi_m^\dagger,\ \delta\mathcal{L}\ \psi_0(\vec{r},E,\hat{\Omega})\rangle - \lambda_0\langle\psi_m^\dagger,\ \delta\mathcal{F}\ \psi_0(\vec{r},E,\hat{\Omega})\rangle - \delta\lambda_0\langle\psi_m^\dagger,\ \mathcal{F}\ \psi_0(\vec{r},E,\hat{\Omega})\rangle}{(\lambda_0-\lambda_m)\ \langle\psi_m^\dagger,\ \mathcal{F}\ \psi_0(\vec{r},E,\hat{\Omega})\rangle}. \tag{B.10}$$

REFERENCES

[1] A. Haghighat, *Monte Carlo Methods for Particle Transport*. CRC Press, 2015.

[2] "Lightbridge corporation advanced metallic fuel.," in *The 11th National Conference on Nuclear Science and Technology Agenda and Abstracts*, 2015.

[3] V. K. Mehta, P. McClure, and D. Kotlyar, "Selection of a space reactor moderator using lessons learned from snap and anp programs," in *AIAA Propulsion and Energy 2019 Forum*. eprint: `https://arc.aiaa.org/doi/pdf/10.2514/6.2019-4451`.

[4] B. Herman, "Monte carlo and thermal hydraulic coupling using low-order nonlinear diffusion acceleration," PhD thesis, Massachusset Institute of Technology, 2014.

[5] J. Wang, Q. Wang, and M. Ding, "Review on neutronic/thermal-hydraulic coupling simulation methods for nuclear reactor analysis," *Annals of Nuclear Energy*, vol. 137, p. 107 165, 2020.

[6] A. Mylonakis, M. Varvayanni, N. Catsaros, P. Savva, and D. Grigoriadis, "Multi-physics and multi-scale methods used in nuclear reactor analysis," *Annals of Nuclear Energy*, vol. 72, pp. 104 –119, 2014.

[7] J. Geiser, "Iterative operator-splitting methods for nonlinear differential equations and applications," *Numerical Methods for Partial Differential Equations*, vol. 27, no. 5, pp. 1026–1054, 2011. eprint: `https://onlinelibrary.wiley.com/doi/pdf/10.1002/num.20568`.

[8] J. C. Ragusa and V. S. Mahadevan, "Consistent and accurate schemes for coupled neutronics thermal-hydraulics reactor analysis," *Nuclear Engineering and Design*, vol. 239, no. 3, pp. 566 –579, 2009.

[9] H. Robbins. and S. Monro, "A stochastic approximation method," *Ann. Math. Stat.*, vol. 22, no. 400, 1951.

[10] J. Dufek and W. Gudowski, "Stochastic approximation for monte carlo calculation of steady-state conditions in thermal reactors," *Nuclear Science and Engineering*, vol. 152, no. 3, pp. 274–283, 2006.

[11] D. Kotlyar and E. Shwageraus, "Numerically stable monte carlo-burnup-thermal hydraulic coupling schemes," *Ann. Nucl. Energy*, vol. 63, pp. 371–381, 2014.

[12] C. T. Kelley, *Iterative Methods for Linear and Nonlinear Equations*. Society for Industrial and Applied Mathematics, 1995.

[13] D. Knoll and D. Keyes, "Jacobian-free newtonkrylov methods: A survey of approaches and applications," *Journal of Computational Physics*, vol. 193, no. 2, pp. 357 –397, 2004.

[14] D. Gaston, C. Newman, G. Hansen, and D. Lebrun-Grandi, "Moose: A parallel computational framework for coupled systems of nonlinear equations," *Nuclear Engineering and Design*, vol. 239, no. 10, pp. 1768 –1778, 2009.

[15] J. Willert, X. Chen, and C. T. Kelley, "Newton's method for monte carlo-based residuals," *SIAM Journal on Numerical Analysis*, vol. 53, no. 4, 2015.

[16] M. Aufiero and M Fratoni, "Stabilization and convergence acceleration in coupled monte carlocfd calculations: The newton method via montecarlo perturbation theory," in *International Conference on Mathematics& Computational Methods Applied to Nuclear Science& Engineering*, Jeju, South Korea, 2017.

[17] A. G. Mylonakis, M. Varvayannia, and N. Catsarosa, "A newton-based jacobian-free approach for neutronic-monte carlo/thermal-hydraulic static coupled analysis," *Annals of Nuclear Energy*, vol. 110, pp. 709 –725, 2017.

[18] B. R. Herman, B. Forget, and K. Smith, "Progress toward monte carlothermal hydraulic coupling using low-order nonlinear diffusion acceleration methods," *Annals of Nuclear Energy*, vol. 84, pp. 63 –72, 2015, Multi-Physics Modelling of LWR Static and Transient Behaviour.

[19] C. Cortes and V. Vapnik, "Support vector networks," *Machine Learning*, vol. 20, 273297, 1995.

[20] K. Smith, "Nodal method storage reduction by non-linear iteration," *Transaction of American Nuclear Society*, 1983.

[21] M. Lee, H. Joo, D. Lee, and K. Smith, "A feasibility study of cmfd acceleration in monte carlo eigenvalue calculation," in *Trans. Kor. Nucl. Soc*, 2009.

[22] W. F. Miller and E. E. Lewis, *Computational Methods of Neutron Transport*. American Nuclear Society, 1993.

[23] F. B. Brown, "Monte carlo techniques for nuclear systems - theory lectures," Nov. 2016.

[24] F. B. Brown, "K-effective of the world and other concerns for monte carlo eigenvalue calculations," *Progress in Nuclear Science and Engineering*, vol. 2, pp. 738–742, 2011.

[25] J Lieberoth, "Monte carlo technique to solve. the static eigenvalue problem of the boltzmann transport equation.," *Nukleonik, 11: 213-19(Sept. 1968).*, Jan. 1968.

[26] T. Goorley, M. James, T. Booth, F. Brown, J. Bull, L. Cox, J. Durkee, J. Elson, M. Fensin, R. Forster, J. Hendricks, H. Hughes, R. Johns, B. Kiedrowski, R. Martz, S. Mashnik, G. McKinney, D. Pelowitz, R. Prael, J. Sweezy, L. Waters, T. Wilcox, and T. Zukaitis, "Initial mcnp6 release overview," *Nuclear Technology*, pp. 298–315, 2017.

[27] J. Leppänen, M. Pusa, T. Viitanen, V. Valtavirta, and T. Kaltiaisenaho, "The serpent monte carlo code: Status, development and applications in 2013," *Ann. Nucl. Energy*, vol. 82, pp. 142–150, 2015.

[28] M. A. Jessee and B. T. Rearden, "Scale code system, ornl/tm-2005/39, version 6.2," Oak Ridge National Laboratory, Report, 2016.

[29] P. K. Romano, N. E. Horelik, B. R. Herman, A. G. Nelson, B. Forget, and K. Smith, "Openmc: A state-of-the-art monte carlo code for research and development," *Annals of Nuclear Energy*, vol. 82, pp. 90 –97, 2015.

[30] E. G. Whitesides, "A difficulty in computing the k-effetive of the world," *Transactions of the American Nuclear Society*, vol. 14, no. 2, p. 680, 1971.

[31] E. Dumonteil, F. Malvagi, A. Zoia, A. Mazzolo, D. Artusio, C. Dieudonn, and C. De Mulatier, "Particle clustering in monte carlo criticality simulations," *Annals of Nuclear Energy*, vol. 63, pp. 612–618, 2014.

[32] M. Nowak, J. Miao, E. Dumonteil, A. Forget B. ans Onillon, K. S. Smith, and Z. A., "Monte carlo power iteration: Entropy and spatial correlations," *Annals of Nuclear Energy*, vol. 94, pp. 856–868, 2016.

[33] T. Sutton and A. Mittal, "Neutron clustering in monte carlo iterated-source calculations," *Nuclear Engineering and Technology*, vol. 49, pp. 1211–1218, 2017.

[34] E. Dumonteil, G. Bruna, F. Malvagi, A. Onillon, and R. Y., "Clustering and traveling waves in the monte carlo criticality simulation of decoupled and confined media," *Nuclear Engineering and Technology*, vol. 49, pp. 1157–1164, 2017.

[35] K. S. Smith, "Reactor core methods," in *Invited lecture at the M&C 2003 International Conference*, Gatlinburg, TN, USA, 2003.

[36] W. R. Martin, "Advances in monte carlo methods for global reactor analysis," in *Invited lecture at the M&C 2003 International Conference*, Monterey, CA, USA, 2007.

[37] K. S. Chaudri, J. Kim, and Y. Kim, "Development and validation of a fast subchannel code for lwr multi-physics analyses," *Nuclear Engineering and Technology*, vol. 51, no. 5, pp. 1218 –1230, 2019.

[38] N. E. Todreas and M. S. Kazimi, *Nuclear Systems, Volume I*. Taylor&Francis, 1990.

[39] J. F. Hewitt, "Pressure drop, two-phase flow," *ThermoPedia*, 2020.

[40] A. T. Bharucha-Reid, "Fixed point theorems in probabilistic analysis," *Bullettin of the American Mathematical Society*, vol. 82, no. 5, pp. 641–657, 1976.

[41] A. Cegielski, *Iterative Methods for Fixed Point Problems in Hilbert Spaces*. Springer, 2012.

[42] S. Terlizzi and D. Kotlyar, "On-the-fly prediction of macroscopic cross-section spatial response to th perturbations through transfer functions: Theory and first results," *Nuclear Science and Engineering*, vol. 194, no. 4, pp. 280–296, 2020.

[43] S. Terlizzi and D. Kotlyar, "On the fly prediction of th-dependent spatial macroscopic cross-sections using fft," in *PHYSOR 2020: TRANSITION TO A SCALABLE NUCLEAR FUTURE*, American Nuclear Society, Cambridge, UK, 2020.

[44] D. Elfverson, V. Ginting, and P. Henning, "On multiscale methods in petrovgalerkin formulation," *Numer. Math.*, vol. 131, 643682, 2015.

[45] Y. Wang, S. Schunert, and V. Laboure, "Rattlesnake theory manual," Apr. 2018.

[46] G. Golub and C. Reinsch, "Singular value decomposition and least squares solutions.," *Numer. Math.*, vol. 14, 403420, 1970.

[47] R. G. Lyon, *Understanding Digital Signal Processing*. Pearson Education, Inc., 2011.

[48] G. Sarty, R Bennet, and R. W. Cox, "Direct reconstruction of non-cartesian k-space data using a nonuniform fast fourier transform.," pp. 908–15, 2001.

[49] V. S. Mahadevan, "Nonlinearly consistent schemes for coupled problems in reactor analysis," PhD thesis, Texas A&M, 2006.

[50] X. Guo, Q. Li, and W. Xu, "Acceleration of the em algorithm using the vector aitken method and its steffensen form.," *Acta Math. Appl. Sin. Engl. Ser.*, vol. 33, 175182, 2017.

[51] L. Xu, "Acceleration of the power and related methods with dynamic mode decomposition," PhD thesis, Kansas State University, 2017.

[52] H. F. Walker and N. Peng, "Anderson acceleration for fixed-point iterations," *SIAM J. Numer.Anal.*, vol. 49, pp. 1715–1735, 4.

[53] A. Toth, J. Austinellis, T. Evans, H. S., C. T. Kelley, R. Pawlowski, and S. Slatter, "Local improvement results for anderson acceleration with inaccurate function evaluations," *SIAM J. Sci. Comput.*, vol. 39, 4765, 5.

[54] S. Carney, F. Brown, B. Kiedrowski, and W. Martin, "Higher-mode applications of fission matrix capability for mcnp," Los Alamos National Laboratory, Los Alamos, NM, USA, Tech. Rep., 2013.

[55] A. Johnson and D. Kotlyar, "A transport-free method for predicting the post-depletion spatial neutron flux distribution," *Submitted for publication*, 2019.

[56] Y. Shaposnik, "Thermal-hydraulic feedback module for bgcore system," PhD thesis, Ben Gurion, 2008.

[57] D. Kotlyar and E. Shwageraus, "On the use of predictor-corrector method for coupled monte carlo burnup codes," *Ann. Nucl. Energy*, vol. 58, pp. 228–237, 2013.

[58] N. Kaffezakis and D. Kotlyar, "Fuel cycle analysis of novel assembly design for thorium-uranium-ceramicfueled thermal, high-conversion reactor," *Nuclear Technology*, vol. 2006, no. 1, pp. 48–72, 2017.

[59] D. K. M. A. Krecicki, "Low enriched nuclear thermal propulsion neutronic, thermal hydraulic, and system design space analysis," *Nuclear Engineering and Design*, vol. 363, 2019.

[60] N. Horelik, B. Herman, B. Forget, and K. Smith, "Benchmark for evaluation and validation of reactor simulations (beavrs)," in *M&C 2013*, 2013.

[61] J. C. Van Den Berg, *Wavelets in Physics*. Cambridge University Press, 1999.

[62] M. Bartholomew-Biggs, S. Brown, B. Christianson, and L. Dixon, "Automatic differentiation of algorithms," *Journal of Computational and Applied Mathematics*, vol. 124, no. 1, pp. 171 –190, 2000.

[63] S. Carney, F. B. Brown, B. Kiedrowski, and W. Martin, "Theory and applications of the fission matrix method for continuous-energy monte carlo," *Annals of Nuclear Energy*, vol. 73, pp. 423–431, 2014.

[64] S. Terlizzi and D. Kotlyar, "Fission matrix decomposition method for criticality calculations: Theory and proof of concept," *Nuclear Science and Engineering*, vol. 193, no. 9, pp. 948–965, 2019.